Politecnico di Torino

Corso di Laurea Magistrale in Ingegneria Meccanica
Dipartimento di Ingegneria Meccanica e Aerospaziale

Tesi di Laurea Magistrale

Study of a spherical inflated light sail riding on a laser beam:
Breakthrough Starshot

Politecnico di Torino:
Prof. Giancarlo Genta - Relatore
Ing. Dario Riccobono - Correlatore
Ankers Juss-AMG:
Ing. Alessandro Genta - Supervisor

Candidato:
Gianmario De Blasio

Anno Accademico 2017 - 2018

A mio nonno Gianni

Abstract

Inflated spherical light sails have been considered to push ultra-light nanocrafts at a significant fraction of light speed. The light sail, which is essentially an extremely thin spherical shell, is subjected to extremely high accelerations and deformations. The purpose of this master thesis is to perform 3D numerical analyses to study the deformed shape of an inflated spherical light sail riding on a laser beam.

The first approach to the problem has been made by resorting to Inertia Relief Method, which suits non-constrained applications and allows to make analyses with good reliability and low computational cost. In order to simulate the inertial effects of the gas an analytical model has been first developed and then implemented.

The next step has been performed by resorting to an explicit solver in order to make a non-stationary analysis simulating also the gas contribution through Smoothed-particle hydrodynamics (SPH).

Common Finite Element codes are not specifically designed to deal with this phenomenon. A similar physical context in which an impulsive dynamic is present can be found in crash events simulated in automotive industry, which can be analyzed by using commercial codes. Since the development of a dedicated numerical code would require a remarkable effort, an attempt of using such commercial codes has been conducted.

Attention has been paid on the simulation of the dynamics of the inflating gas and its effect on sail deformation. Moreover, the effect of changing the features of the sail shell such as material, thickness and the inflating pressure have been considered.

The results of this investigation can be used as guideline for sail design, as well as an input for further analysis on sail stability.

Acknowledgements

This master thesis work has been developed both at Ankers juss-AMG and at DIMEAS (Polytechnic of Turin).

I am very grateful to Professor Genta for the opportunity he gave me to work on such an amazing project. He allowed me to approach a field I am very interested in and he always supported me during my work. It has been an honor to work with him and his support has been crucial.

I am thankful to Ing. Alessandro Genta and the people from Ankers for their support and because they made me feel part of a family.

A special word of thanks goes to Dario, that was always present throughout the whole work encouraging and helping me.

Contents

List of Figures

Chapter 1

Introduction

The Breakthrough initiatives are a program of scientific and technological exploration, which try to solve the big mysteries of life in the Universe: are we alone? Are there habitable planets in our galactic neighborhood?

We can watch at life in the universe from a different perspective: it doesn't necessarily mean extraterrestrial life, it also means us. As far as we know, we have never been visited from other beings, but neither have we stepped out to the galactic stage. The obvious question is: are we destined to belong to our native planet as long as we survive, or can we reach the stars? If we start thinking that we can, the first step is our nearest star-system, Alpha Centauri, which is "only" four light years away.

Space propulsion system of common use are unable to provide enough energy to accelerate a space probe at a reasonable speed for interstellar travel. A travel of a few light years is feasible if it is possible to reach a significant fraction of the speed of light. Light power represents a possibility to go in that direction.

Target

On August 24, 2016 - the ESO announced the discovery of a new exoplanet, Proxima b, which is also the first exoplanet discovered in the Alpha Centauri system. At the moment, this planet is identified as the primary target of Starshot interstellar mission. The common interest about a mission towards Proxima b

comes from the fact that it has Earth-like properties (roughly the same mass, probably a rocky composition). Although it is placed in the so called "habitable zone" of its star, it is still unknown whether it has either liquid water (which would be allowed by the temperature) or an atmosphere, or other conditions suitable for life. These and many others properties will be objects of intense investigation in the coming decades.

Alpha Centauri

The Alpha Centauri system is a three-stars system: it comprises a pair of Sun-like stars, Alpha Centauri A and B, along with Proxima Centauri which is the closest star to the Sun.

Breakthrough Starshot is a $100 million project aiming to demonstrate proof of concept for a new technology, allowing to lay the foundations for a flyby mission to Alpha Centauri within a generation. In particular, at this moment the idea is to build an ultra-light laser-propelled light sail, able to travel at 20% of the speed of light and so able to reach Alpha Centauri in about 20 years.

Light Sail, StarChip and Laser cost

Advances in nanotechnology are producing meta-materials with increasing strength-to-weight ratios, promising to allow the fabrication of meter-scale sails with a thickness not higher than a few atoms and at gram-scale mass. Progress in technology has allowed a huge decrease in the size of electronic components; this enables the developing of a gram-scale chipset carrying cameras, photon thrusters, power supply, navigation and communication equipment. This would constitute a fully functional space probe.

The same goes for the laser cost which, following Moore's law, has undergone a significant drop in costs and an important rise in power. It led to notable advances in light beaming technology, while phased arrays of lasers could theoretically be scaled up to a level of hundreds of Gigawatt which is of the same order of magnitude of the power requested to accelerate the sail up to such high accelerations.

Solar sails (also called light sails) are a form of spacecraft propulsion using

radiation pressure exerted by sunlight on large reflecting surfaces. High-energy laser beams could be used as an alternative light source to exert much greater force than would be possible using sunlight, a concept known as beam sailing.

Solar sails allow low-cost operations along with long operating lifetimes. Since they have few moving parts and use no propellant, they could be used several times for various reasons.

Solar sails use a phenomenon that has been proved to work on spacecrafts. Solar pressure affects every spacecraft in space or in orbit around some planet. For example a typical spacecraft directed to the red planet will be displaced thousands of kilometers by the pressure coming from solar radiation and so the effects must be taken into account during trajectory planning, which has been done since the time of the earliest interplanetary missions in the 1960s. Solar pressure also affects the orientation of a craft, a factor that must be included in spacecraft design. [22] [23]

1.1 Description of the mission

The ultimate aim of the project is to send the light sail to Alpha Centauri and to bring back useful data that can tell us more about extraterrestrial life in the universe. The hardware designated to collect and send back data should be enclosed within a chipset not larger than a common credit card.

As mentioned above, the sail should be able to travel at 20% of the speed of light; to reach that velocity in a reasonable time (order of magnitude of some minutes) it needs to be accelerated up to tens of thousands of g's. To make this happen, a huge power from the laser plant is required. Of course, the power needed is proportional to the mass of the sail and to the acceleration which is needed to be achieved, so minimizing the mass is a priority.

A particularly important problem is ensuring that the sail remains centered on the laser beam despite disturbances, misalignment, and manufacturing imperfections. A sail with an active-feedback control would easily perform this task, but unfortunately it is not possible as the addition of sensor and actuator hardware would add significant mass and complexity to the spacecraft. For this reason a passively stable configuration must be adopted in order to keep the sail centered

on the beam as long as needed.

The passive stability comes from both the shape of the sail and the laser beam profile. In [1] a stable beam-riding architecture was found by projecting the dynamics onto the *transverse subspace* ; such a stable configuration was achieved by combining a spherical shape with a multimodal beam profile, composed by the sum of four Gaussians. For this reason the analyses discussed in the following chapters are based on this layout.

Predictions

The research and development phase is expected to last a certain number of years. After that, the development of the ultimate mission to Alpha Centauri would require a budget of the same order of magnitude of the largest current missions. The prediction is that, once the technology is mature, each launch cost is estimated to drop to a few hundred thousands dollars.

Challenges

The program will require to go beyond several theoretical and technological issues; the nanocraft concept explained above is by far the most plausible system for launching a feasible mission to Alpha Centauri within a generation. The key elements of the proposed system design are based on technology which is in part ready and in part in development, hopefully to be achievable in the near future under reasonable assumptions. The good news is that no "deal-breakers" have been identified by the team of expert scientists and engineers leading the program.

An example could be building a ground-based kilometer-scale light beamer at high altitude, in dry conditions, or generating and storing a few gigawatt per hours of energy per launch.

The proposed light propulsion system is on a scale significantly exceeding any current operational analog. This is why the nature of the project calls for global co-operation and support.

Authorizations for launches would be required from all the appropriate institutions and governments.

In addition, it would be necessary to take into account that dust collisions may happen during the mission to the target. A collision at such high velocities would be fatal for the sail, unless it is provided an appropriate coating which could help in some case.

It will also be of the highest importance to bring back images of the planet and other scientific data. To make that happen, a compact and light set of cameras should be placed on the chipset, but also a compact on-board laser communication system to transmit them back to Earth.

The issues that will be encountered to make this mission actually feasible are numerous, and some of them will be discussed in the next sections.

Chapter 2

Sail configuration

The following topics will be briefly reviewed in this chapter:

- *Shape of the sail*
- *Laser beam profile*
- *Choice of the material*
- *Internal pressurized gas*
- *Brief description of the launch process*

2.1 Shape of the sail

In [1], first the transverse dynamics of conical sails along with a unimodal gaussian laser beam was investigated; it was proven that a simple conical sail cannot achieve stability since the center of mass must lie beneath the base of the cone by a significant distance. There are mechanical solutions that could lower the center of mass, such as a rigid pendulum, but they would introduce serious practical difficulties:

- *any such structure will necessarily be exposed to the laser beam;*
- *significant additional mass would be added to the spacecraft, allowing it to achieve a lower acceleration with a given beam power;*

- *the flexible modes of the structure and their effect on stability would require careful analysis.*

Taking into account the reasons listed above, the hypothesis of using a conical sail was excluded and after a proper investigation, as it was anticipated in the description of the mission, a spherical shape of the sail was chosen in order to obtain a stable beam-riding configuration. Lastly, the interior of a spherical sail would naturally provide a shielded environment for electronics or other payload items.

2.1.1 Laser beam profile

The beam-riding configuration must take into account both the shape of the sail and the beam profile, so that the combination of the two generates a passively stable condition.

The laser beam profile, which combined with a spherical shape of the sail yields a passively stable beam-riding configuration, is a multimodal beam profile formed by the sum of four Gaussians. Such a particular profile was chosen due to the ease of producing gaussian beams and their favorable divergence properties and it allows to produce on an appropriately shaped spherical sail a restoring force which pushes it back toward the center thanks to the increased power in the sides of the beam. Physically, the sail will oscillate around the center of the beam, but the amplitude of the oscillation will remain bounded.
The function that describes the gaussian three-dimensional profile is:

$$f(x,y) = \frac{\exp\left(-\frac{1}{2(1-\rho^2)}\left[\frac{(x-\mu_x)^2}{\sigma_x^2} + \frac{(y-\mu_y)^2}{\sigma_y^2} - \frac{2\rho(x-\mu_x)(y-\mu_y)}{\sigma_x\sigma_y}\right]\right)}{2\pi\sigma_x\sigma_y\sqrt{1-\rho^2}} \tag{2.1}$$

In which:

- σ_x, σ_y : standard deviation in x and y directions (in this case $\sigma_x = \sigma_y$);
- ρ : correlation between x and y directions (in this case ρ=0 thanks to the symmetry of the distribution);
- μ_x, μ_y : peak-shifting parameters in x and y directions.

The standard deviations are computed starting from the assumption that the laser beam which accelerates the sail has a *full-width-at-half-maximum* W, with W and the *sail radius* of the same order of magnitude (it is worth to underline that also W has two components, one for each direction). In particular, the relationship between W and σ in a certain direction is:

$$\sigma = \frac{W}{2\sqrt{\ln(2)}} \tag{2.2}$$

The 2.1 just gives the shape of one generic gaussian. The power distribution which needs to be applied to the sail in order to obtain a dynamically stable configuration is the sum of four different gaussians, each one with the peak centered on a circumference with a radius equal to the sail radius plus a certain value of tolerance; such circumference has the following equations:

$$x^2 + y^2 = (r + tol)^2$$

in which r is the sphere radius.

The shift parameters are obtained from the intersection of this circumference with the bisectors of 1st and 3rd quadrant and 2nd and 4th quadrant, as showed in Table-Figure 2.1.

	μ_x	μ_y
μ_1	Γ	Γ
μ_2	$-\Gamma$	Γ
μ_3	$-\Gamma$	$-\Gamma$
μ_4	Γ	$-\Gamma$

Table 2.1: Value of the shift parameters μ_x and μ_y for gaussians $1 \div 4$. $\Gamma = \sqrt{(r + tol)^2/2}$

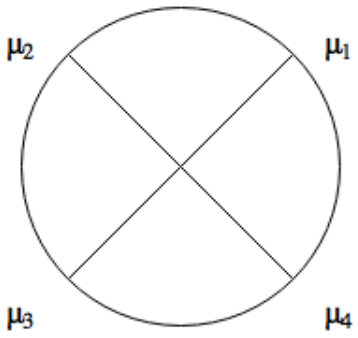

Figure 2.1

The presence of a tolerance (of the order of magnitude of $(0.2 \div 0.5)r$) makes sure that the sail is entirely within the basin of attraction which is located in the middle of the total distribution. Such basin of attraction is the valley between the

four peaks, as it is shown in figure 2.2.

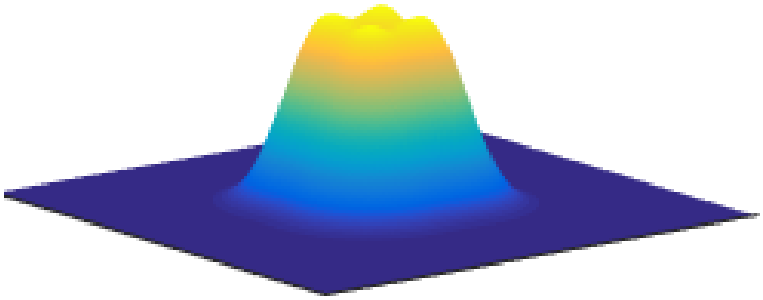

Figure 2.2: *Laser beam profile*: a multimodal profile made by the sum of four gaussians. The four peaks are positioned so that the final distribution is symmetric.

The function shown in the figure 2.2 represents only the shape of the power distribution, so it needs to be normalized with respect to the intensity of the laser in order to compute the pressure exerted on the sail.

2.1.2 Choice of the material

The material used for the simulations that will be shown in this master thesis was chosen among the materials currently available on the market. The fact that Starshot project will not be completely ready for at least ten years from now makes this choice very hard, because there is a strong possibility that the material which will actually be used to build the sail doesn't exist yet. In view of this, it is clear that a material with a strength-to-weight ratio as high as possible is required, since not only a low mass but also an high strength is desirable. For this reason, at the moment Carbon Nanotubes (CNTs) seem the best candidate. To make this choice more clear it can be useful to show a comparison of strength-to-weight ratios for some materials.

The informations showed in 2.2 give a qualitative idea of the amazing properties of CNTs (STW ratio up to two order of magnitudes higher with respect to other materials) if compared to other materials which can be currently found on the market.

Going into a detailed discussion about the Carbon Nanotubes structure and

Material	**Strength-to-weight ratio** $[kN\frac{m}{kg}]$
Alluminum alloy (7075-T6)	204
Titanium alloy(Beta C)	260
Carbon-epoxy composite	785
Carbon fiber (AS4)	2457
Kevlar	2514
Carbon Nanotubes	46268

Table 2.2: Strength-to-weight ratios for some materials. [2]

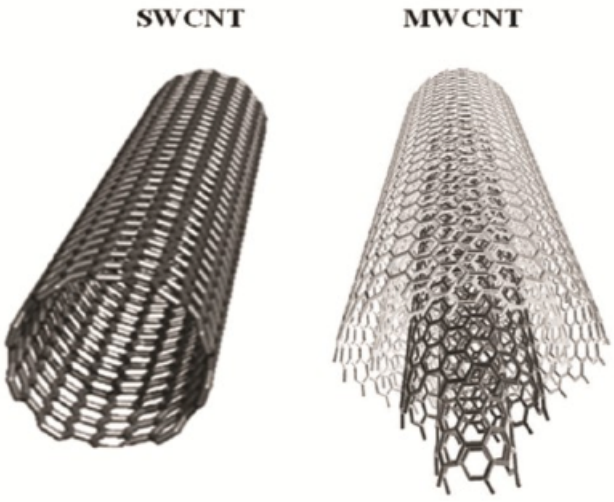

Figure 2.3: *Picture of SWCNT and MWCNT*

properties falls outside the scope of the present work, but there are some informations which can be useful, for sake of clarity.

Let's start saying that CNTs macro-properties are deeply different from their micro-properties. In fact, their behavior is strongly anisotropic on a quantum level but they can be considered linear isotropic on a macroscopic scale like that of our interest (the sail has a diameter of about 2 m); this is because it is reasonable to believe that the random orientation of each CNT in the macro-structure mitigates the strong anisotropy of the CNT alone. For the same reason, it is also reasonable to assume that the amazing properties shown on an atomic scale are not the actual properties shown by the sail itself.

Property	**Value**
Young's modulus [GPa]	200
Tensile Strength [GPa]	10
Poisson's ratio	0.1
Density [kg/m^3]	1350

Table 2.3: Main mechanical and physical properties of CNTs [2]

The values reported in the table 2.3 are referred to an atomic scale and are realistic only along the same directions of $C-C$ bonds of CNTs rings. This is why they need to be corrected with appropriate weightings before they can be used for the definition of the material to use in Finite Element Analyses.

Furthermore, another factor influencing the mechanical properties of CNTs is the number of layers (in 2.3 an example of both Single Wall and Multi Wall CNTs is reported).

In order to keep the mass of the sail as low as possible, also the thickness must be the lowest possible. From the analyses that will be discussed in detail later, it comes that the thickness varies between $0.1 \div 1 \mu m$. This means that the thickness of the sail can be comparable with the outermost tube diameter and that is why the number of layers (which at the same time slightly influence the mechanical properties) must be chosen after having reached a good compromise between mechanical properties and thickness.

There are also other factors influencing the CNTs elastic properties (*e.g. tube*

chirality) which need to be taken into account if an in-depth material model is requested. [3]

2.1.3 Internal pressurized gas

A topic which has not been addressed so far is that of the internal pressurized gas used to inflate the sail.

The sail must be inflated with a gas to maintain its shape. This would allow many sails to be stored compactly and launched inside a conventional rocket before being inflated in Earth orbit and accelerated with a ground-based laser. It would also allow the sail to be deflated after the acceleration phase, and perhaps reconfigured for some other purpose.

But there are also side-effects of the presence of the gas which must be considered, and in particular the inertial effects. In fact the mass of pressurized gas enclosed into the sail generates, when undergoing ultra-high accelerations, a density field which depends on the axial coordinate Z (in the direction of motion). In fact the gas applies an additional pressure due to its inertia, in the direction pointed in Fig. 2.4.

The analytical model which describes the density field $\rho(z)$ will be discussed in great detail in section 5.2.

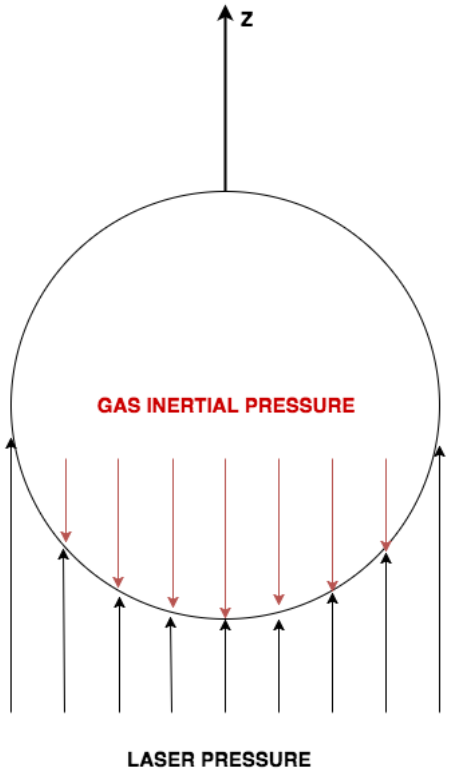

Figure 2.4: *Qualitative scheme which shows the directions of the external laser pressure which accelerates the sail versus the internal gas pressure due to inertial effects. Please note that the figure doesn't show the gas internal pressure on the upper face which is still present, only with a smaller magnitude. In addition, the arrows are parallel to the* Z *direction, but actually the pressure exerted on each point of the sail has a magnitude which comes from the projection on the direction perpendicular to the surface in that point.*

2.2 Launch process

The launch process is a topic which will be addressed during a more advanced phase of the project, so in this thesis only some important concepts will be discussed.

How will the laser be built?

If we think of a laser like a point source, as we are used to when we deal with commercial lasers, it is easy to understand that the actual area of the laser spot which exerts a pressure over the sail depends both on the distance from the source r and the divergence angle θ (shown in Fig. 2.5) :

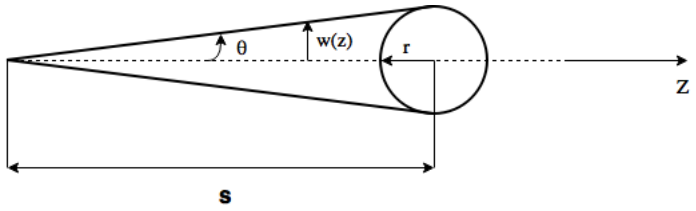

Figure 2.5: *Laser point source scheme. In this configuration* $\boldsymbol{s}$ *is chosen so that* $A_{spot} = A_{sail}$ *(in which* A_{sail} *is the projected area of the sphere).*

Referring to the configuration illustrated in 2.5 the following relation can be written:

$$A_{spot} = \pi w(z)^2 = \pi r^2 = A_{sail} \tag{2.3}$$

In this case the peaks of the four gaussians fall exactly on the outer circumference of the projection of the sphere, because the tolerance (see Fig. 2.1) is of course equal to zero.

This case allows to compute a certain distance from the source r which satisfies the equivalence 2.3, as:

$$s = \frac{w}{tan(\theta)} = \frac{r}{tan(\theta)} \tag{2.4}$$

So the sail must be put at a distance $s_{start} \geq s$ so that its initial condition lie within the basin of attraction surrounding the center of the beam and the sail

will remain trapped in the basin. But after the sail starts moving, A_{spot} starts growing and so does the tolerance ($tol = w(z) - r$). This means that the actual power available for propulsion starts falling down very rapidly because the gaussian distribution of Fig.2.2 sees the distance between its peaks increasing and so the circular integral

$$\int_{-r}^{r} \int_{-(r^2-x^2)}^{r^2-x^2} E_f \cdot f_{tot}(x,y) dxdy \tag{2.5}$$

rapidly decreases. The $f_{tot}(x,y)$ comes from the sum of four gaussians as the one in Eq. 2.1, each one with the peak shifted in the $x-y$ plane in order to match the positions showed in Fig. 2.1; E_f is the irradiance of the laser and is measured in $\frac{W}{m^2}$.

To make this concept more clear, an iterative computation has been performed in order to plot the acceleration of the sail versus the distance from the source, for a given divergence angle θ; starting from the time $t = 0$ in which the configuration is the one showed in Fig. 2.5, the new state of the system is computed for each time step. In this computation the angle of divergence is $\theta = 2.258 \cdot 10^{-4} rad$, which is a value for lasers of common use.

The Fig. 2.6 clearly shows how the acceleration of the sail goes to zero in only half a second due to the fact that the area of the laser spot increases dramatically and so the net power flux on the sail goes to zero. At the same time the velocity increases up to about $5 \cdot 10^4 \frac{m}{s}$ and then stabilizes itself due to the decreasing acceleration.

The velocity reached in such a short time is more than three orders of magnitude smaller than the target ($20\%c \approx 5.996 \cdot 10^7 \frac{m}{s}$), so it is clear that a traditional laser cannot handle a thing like that.

For the sake of completeness Fig. 2.7 shows the displacement of the sail, which after about $19km$ has reached a null acceleration.

To solve this issue, the laser cannot be considered a point source but it needs to have a diameter of the same order of magnitude of the sail (slightly bigger to include a tolerance to ensure the stability) with $\theta \approx 0$. In this way the A_{spot} can be considered equal to the projection of the sphere surface plus the ring due to the

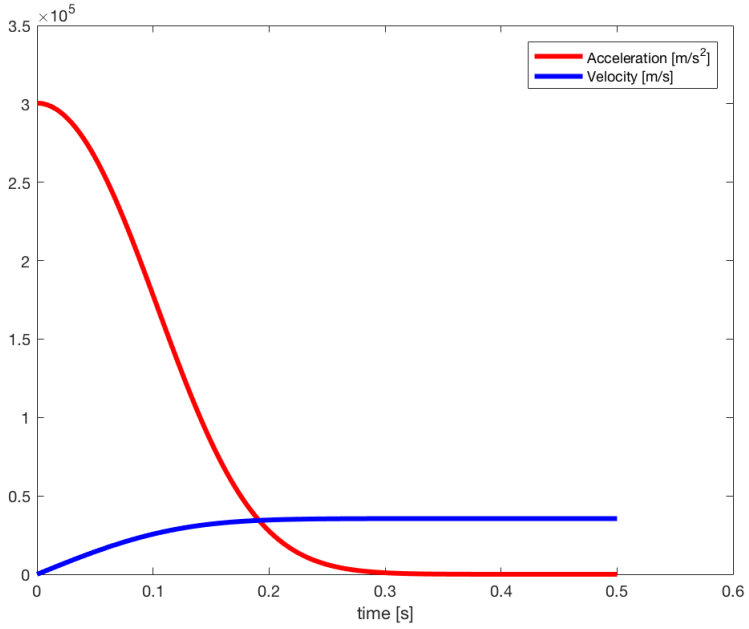

Figure 2.6: *Acceleration of the sail vs time.*

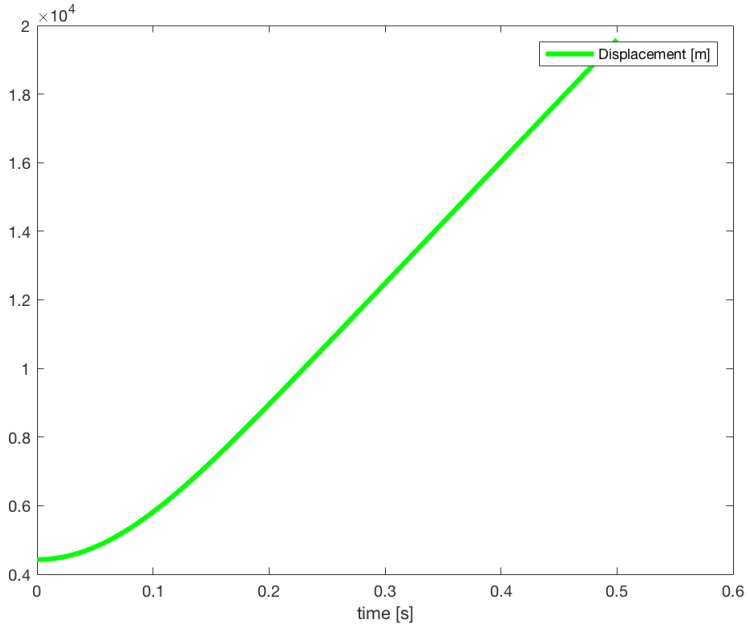

Figure 2.7: *Displacement of the sail vs time.*

tolerance, for the whole duration of the process.

So, for example, with a constant acceleration of $20000g$ the sail would reach the target velocity in just 306 *seconds* , which is about half the time of 10 *minutes* which was given as limit for the project.

In the following sections a detailed analysis about the maximum acceleration reachable with a given sail configuration will be shown.

Where will the laser plant be placed?

At the moment, there are some ideas about where to put the laser plant which is in charge of the propulsion of the sail:

1. *Earth surface*;
2. *Earth orbit*;
3. *Moon surface.*

The option which looks more realistic is the first one; in fact the idea of placing the laser plant in orbit or more difficult on the moon surface, doesn't look feasible in the short time. In fact, apart from dealing with the issues of the transportation and the energy storage, another important issue is that such a powerful laser (hundreds of GW of power) placed somewhere above the earth could become a weapon of mass destruction if it falls into the wrong hands.

On the other hand, placing the lasers on the Earth surface means that it is necessary to deal with atmospheric effects on the laser beam; to go beyond this issue it could be necessary to take advantage of adaptive optics technology in real time to compensate these effects dynamically.

In any case, this issue will be addressed directly from the USA military and USA government and detailed informations will not be shared publicly.

How many sails will be launched? And when?

When the project will be ultimated, the sails will not just launched at a random time. The study of the right timing for the launch will be addressed in a

later phase of the development and will require an accurate planning. The same goes for the number of sails which will be launched. A statistic study will be developed in order to understand what is the number of sails which guarantees a good probability that at least one reaches the target, with respect to the cost of the mission.

Another launch layout which has been discussed is the so called "Mothership Layout". It considers to launch a "Mothership" carrying thousands of nanocrafts to a high-altitude orbit.

This topic will not be discussed further in this work.

Chapter 3

2D Model

The aim of the study (as reported in [2]) was to perform a first approximation to verify whether the low thickness of the sail and the potentially large deformation cause numerical stability problem of the Finite Element code used. Such study was made to obtain some indications useful to develop a more complicated and complete 3D model. For this reasons, some simplifications were done:

- **CAE code -** Rather than using a specialized FEM code, the SolidWorks suite was used to perform both the design and the study. This software was chosen because it allows to perform a quick but reliable analysis. For the more complex 3D analyses, a specialized FEM code included in the Altair Hyperworks suite was used.

- **Axisymmetric Geometry -** Both the beam and the sail were considered completely axisymmetric.

- **Ticker shell -** A 2D flat mesh approach was used to mesh the shell of the sail, and it forced the choice of a much ticker membrane with respect to the actual thickness of the sail in order to avoid unacceptable numerical errors and raising simulation time. In particular the thickness used for the 2D case is $t = 5\ \mu m$, much larger than the one used for the 3D case ($t = 0.1\ \mu m$).

- **Smaller Sail -** The CAD model of the sail was made by imposing a sphere radius of $r = 0.5\ m$ in order to reduce the size of the problem and so the

computational cost. The 3D model (which will be described later) was made with a sphere radius of $r = 1\ m$.

- **Higher required mass -** The mass required as a result of the analysis (*50 grams*) is much bigger than the actual requirements of the project (*few grams*) .
- **Accelerations much lower than the target -** In this first analysis, for the reasons about numerical stability already listed above, an acceleration of $30g's$ was assumed.

Also for the 2D model, CNTs are used. In particular, the mechanical properties are the same listed in 2.3. This material, combined with the geometry described above ($r = 0.5\ m$ radius and $t = 5\ \mu m$ thickness) leads to a dry mass of the sail of $21.2g$, far from the upper limit of $50g$ (target of the simplified analysis).

Imposing an inflating pressure of $10Pa$, considering an equilibrium temperature at $200K$ between the gas and the interplanetary space near Earth [5] , the mass of the system raises to $21.3g$.

The forces in the model can be summarized as follows:

- **Inflating pressure -** Due to the presence of the gas within the shell. It has a stabilizing effect and it is constant on the whole inner surface.
- **Light pressure exerted by the laser beam -** Applied only on one hemisphere.
- **Inertial forces of the gas -** During the acceleration in one direction, the gas mass exerts a pressure due to its inertia, on the inner surface of the same hemisphere where the laser pressure is applied.
- **Inertial forces of the shell -** The same goes for the shell itself, which undergoes an inertial force due to its mass.

Since the model is axisymmetric, the assumption of modeling the phenomenon with a 2D model helps containing the computational time and cost and at the same time guarantees a good reliability of the results.

3.1 Laser Pressure

The light pressure is calculated by considering both the contribution coming from the reflection and the absorption of the surface material [6]. For this reason, radiation pressure is analyzed as interactions by either electromagnetic particles (photons) or waves (***wave-particle duality***) . In both cases the property of *momentum* is present.

3.1.1 Poynting vector

According to Maxwell's theory of electromagnetism, an electromagnetic wave carries momentum, which can be transferred to the surface hit by the wave through reflection or absorption.

The intensity of the flux is expressed by the ***Poynting vector***:

$$\mathbf{S} = \mathbf{E} \times \mathbf{H} \tag{3.1}$$

in which $\mathbf{E}$ is the *electric field* vector and $\mathbf{H}$ is the *magnetic field*'s auxiliary field vector.

The radiation pressure exerted by an electromagnetic wave on the surface of a target is given by the *time-averaged intensity* $\langle \mathbf{S} \rangle$ divided by the speed of light in free space.

Radiation pressure by absorption *(waves)*

If the wave is completely absorbed:

$$P_{absorb} = \frac{\langle S \rangle}{c} = \frac{E_f}{c} \quad [Pa] \tag{3.2}$$

in which **P** is pressure, $\mathbf{E_f}$ is intensity of the flux (in W/m^2), **c** is speed of light in vacuum. If the absorbing surface is planar at an angle α to the radiation source, the intensity of the actual pressure exerted on the surface will be reduced by the angle of the flux and a reduction in the frontal area:

$$P_{absorb} = \frac{E_f}{c} cos^2(\alpha) \ \ [Pa] \tag{3.3}$$

which means that while the component of momentum normal to the surface exerts the pressure, the tangent component does not contribute to the pressure (α is the angle between the surface normal and the incident radiation).

Radiation pressure by reflection *(particle model - photons)*

The pressure applied on the surface by reflection can be quantified by resorting to the particle model. Electromagnetic radiation is quantized in particles called photons. Photons are zero-rest mass particles but they have the property of energy and momentum as they travel at light speed.

The generation of the pressure comes from the changes in the momentum when incident radiation encounters a surface. The surface exerts a force on the photons in changing their momentum by *Newton's second law* and a reaction force is applied to the body by *Newton's third law.*

In analogy with the absorption case:

$$P_{refl} = \frac{2E_f}{c} cos^2(\alpha) \ \ [Pa] \tag{3.4}$$

In this case it can be noted that the pressure exerted on the surface is doubled with respect to the case of complete absorption.

Global radiation pressure

Considering that part of the radiation is absorbed and another part is reflected,

the summation of 3.3 and 3.4 gives the global pressure exerted on the surface of the target:

$$P_{tot} = kP_{refl} + (1-k)P_{abs} = k\frac{2E_f}{c}cos^2(\alpha) + (1-k)\frac{E_f}{c}cos^2(\alpha) \tag{3.5}$$

which yields:

$$P_{tot} = (1+k)\frac{E_f}{c}cos^2(\alpha) \tag{3.6}$$

where $0 \leq k \leq 1$ is the fraction of beam flux reflected. Since the current CAE software doesn't project the pressure along the normal autonomously, it was necessary to discretize the outer surface with a certain number of slices (in this case $n_{slices} = 20$) so that each slice undergoes a different value of pressure, dependent from angle α. For this reason, P_{tot} is a vector with a cardinality equal to the number of slices n_{slices}.

Discretizing the surface is also useful because so the contribution of inertial pressure of internal gas can be calculated by multiplying the mass of the gas volume contained within a slice and the acceleration per unit area exerted on that slice by the laser beam. For this reason also the gas inertial pressure has the same number of components of laser pressure, and each slice of surface undergoes a combination of the two.

3.2 Numerical analyses

For the reasons listed above, it is interesting to investigate both the contribution of the sail reflectivity and the contribution of the absorption. It is evident that would be better to have a total reflectivity in order to have the best power-to-thrust ratio, so the following case studies are developed:

- ***Case Study 1*** **-** Complete reflectity ($k = 1$) and constant distribution of laser beam power.

- ***Case Study 2*** **-** 90% reflectivity ($k = 0.9$) and constant distribution of laser beam power.
- ***Case Study 3*** **-** 90% reflectivity ($k = 0.9$) and double-Gaussian distribution of laser beam power.

The parameters of the case studies are showed in table

	Case Study 1	**Case Study 2**	**Case Study 3**
k	1	0.9	0.9
$\mathbf{E_f}$	$1.2GW/m^2$	$1.2GW/m^2$	Gaussian distribution

Table 3.1: Parameters used for the three case studies [2]

The Gaussian distribution for the beam power flux used in *Case Study 3* is a 2D distribution, sum of two identical Gaussians, in order to be compatible with the 2D simplified model.

Each Gaussian has a standard deviation described by the equation:

$$\sigma = \frac{W}{2\sqrt{\ln(2)}} \tag{3.7}$$

The two distributions are described by the following functions:

$$E_{f_L} = \frac{K}{\sigma\sqrt{2\pi}} \exp\left(-\frac{(x+\mu_L)^2}{2\sigma^2}\right) \tag{3.8}$$

$$E_{f_R} = \frac{K}{\sigma\sqrt{2\pi}} \exp\left(-\frac{(x+\mu_R)^2}{2\sigma^2}\right) \tag{3.9}$$

in which E_{f_L} is the left component and E_{f_R} is the right component. What is more, μ_L and μ_R are two shifting parameters which, in this case, are so that the distance between the two peaks is equal to the diameter of the sphere plus a 20%D tolerance (as shown in fig. 3.1) that helps increasing the stability of the motion, enabling

little oscillations about the center of the beam (which is the valley between the two peaks).

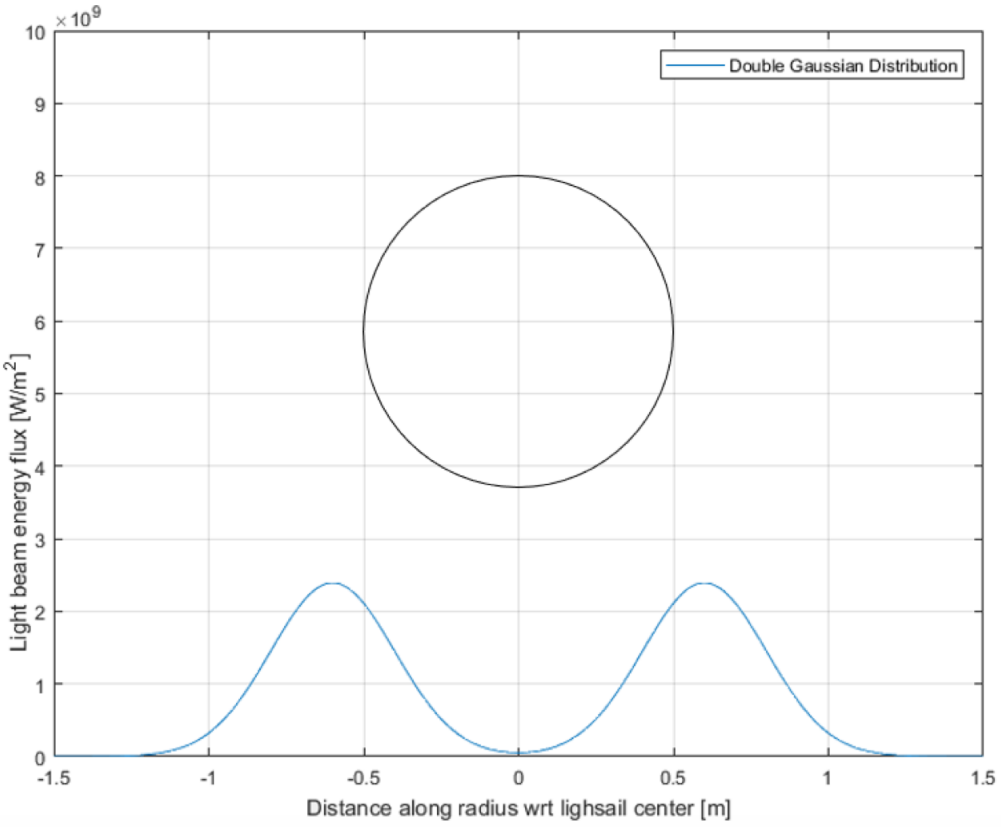

Figure 3.1: *Position of the two Gaussians with respect to the sphere.*

The final gaussian comes from the sum of the left component and the right component:

$$E_f = E_{f_L} + E_{f_R} \tag{3.10}$$

3.2.1 Simulation parameters

Since the aim of the analysis was to determine the deformed shape of the sail when it is subjected to the pressure of the laser that accelerates it, a non constrained

analysis was necessary. In fact, during its motion in deep space, the sail doesn't have any constraint and moves as a free body.

In order to do that, a non-stationary non-linear analysis was performed with the only constraint of a straight trajectory.

The parameters of the simulation are summarized in table 3.2 and mesh properties are listed in table 3.3:

Analysis type	2D, axisymmetric, non-stationary, non-linear
Run time	1 sec
Time step	0.1 sec
Type of solver	Direct solver for sparse matrices
Iteration Method	Newton-Raphson
Integration Method	Newmark

Table 3.2: Simulation parameters [2]

Mesh type	2D flat mesh
Max element dimension	0.1 mm
Min element dimension	0.05 mm
Total number of elements	40960
Total number of nodes	122883

Table 3.3: Mesh Parameters [2]

3.2.2 Results and conclusions

The results of the simulations show how the deformations of the spherical shell are very low if compared with the macro-dimensions of the sail (maximum equivalent deformation is about 5 μm). This is because the maximum stress generated on the sail is beyond four orders of magnitude less than the tensile strength of CNTs showed in tab 2.3.

Also, the case study 3 shows how the 2D Gaussian distribution generates a stress on the sail that is one order of magnitude less than the stress generated by the first two case studies.

The simplified analyses are useful to understand the behavior of the system and give some information about the order of magnitude of the deformations experienced by the sail, and likely a qualitatively reliable deformed shape. Taking into account all the simplifications made, only a complete 3D model for both the sail and the power distribution can give results which are actually reliable.

Chapter 4

Preliminary 3D Analyses

After the preliminary 2D analyses were performed, the path to follow was already marked out. The natural continuation to the work showed in chapter 3 was of course a 3D analysis, which is necessary to tear down most of the simplifications made in the 2D case.

In order to build a model and run a simulation which allows to describe the motion of the light sail in the most accurate way possible, it is necessary to develop a non-stationary and non-constrained simulation.

Developing a 3D model of such a phenomenon is very demanding, both in terms of modeling time and computational cost.

For this reason, it seemed a better choice to make the transition from 2D to 3D smoother by using a method , called "inertia relief method", that is able to perform unconstrained analyses with no need to resort to an explicit solver.

In order to build this kind of analyses, it was necessary to switch to a more specialized commercial code based on Finite Element Method. In particular, from now on all the studies and results that will be shown are made through the Altair HyperWorks suite.

4.1 Overview about the software

Altair HyperWorks is one of the most comprehensive, open architecture CAE simulation platform in the industry. It offers the best technologies to design and

optimize high performance, weight efficient and innovative products.

HyperWorks includes best-in-class modeling, linear and nonlinear analyses, structural and system-level optimization, fluid and multi-body dynamics simulation, electromagnetic compatibility (EMC), multiphysics analysis, model-based development, and data management solutions.

4.1.1 FEM commercial code structure

The Altair suite includes numerous tools that are used to perform analysis in several branches of Engineering field. In general, the logical structure of a Commercial Numerical Analysis Code based on Finite Element Method can be described as in Fig. 4.1:

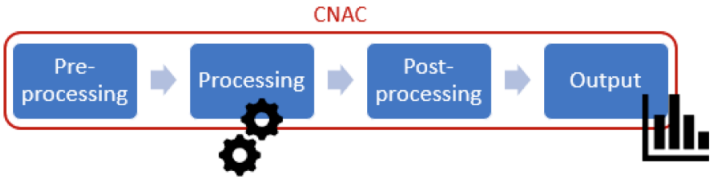

Figure 4.1: *Flowchart - Logical structure of a Commercial Numerical Analysis Code*

Pre-Processing phase

For what concerns the analyses that will be described from now on, the pre-processor used was HyperMesh.

HyperMesh is a multi-disciplinary finite element pre-processor which manages the generation of the largest, most complex models, starting with the import of a CAD geometry to exporting ready-to-run solver file.

With a wide set of direct CAD and CAE interfaces and the ability to define custom integrations, HyperMesh works seamlessly within any engineering environment.

One of the most important features which this pre-processor offers is the support of different solver formats for both import and export phases. Along with fully supported solvers, HyperMesh provides a completely tailored environment (user profile) for each supported solver. For each solver supported by HyperMesh, it

organizes its UI in a different way showing panels relative to the user profile chosen (which is associated to the solver).

The pre-processing phase includes all the operations made to develop the model, from geometry clean-up to the meshing phase, but also the modeling of all the loads and the constraints, whose definition is dependent from the solver that will be used to run the analysis.

In fact, each solver needs to be set with a different set of the so called "CARD IMAGES" that needs to be set-up in a specific way, depending from the solver which is used.

After the pre-processing phase HyperMesh generates a file which can be read from the processor (or solver) the model was built for (and that is defined from the user profile).

Processing phase

As already said before, there are several solvers (or processors) compatible with HyperMesh (also solvers not made by Altair like Abaqus, Ls-Dyna, etc.), some of them are implicit solvers, others are explicit solvers. Implicit and Explicit are two types of approaches that can be used to solve the finite element problem.

The implicit approach is useful in problems in which time dependency of the solution is not an important factor (e.g. static structural, harmonic, modal analysis etc.).

Explicit Dynamics approach is more used when it is necessary to solve high deformation, time-dependent problems which present impulsive dynamics (e.g. Crashes).

The first difference between the implicit and explicit scheme lies in the consideration of velocity or acceleration. For example, let's consider the equilibrium equation of a mass-spring-damper system, relating mass matrix M , damping matrix C , stiffness matrix K and external force vector F . In equation 4.1 , $\mathbf{x}$ represents the displacement and $\dot{\mathbf{x}}$ and $\ddot{\mathbf{x}}$ stand respectively for velocity and acceleration.

$$M\ddot{\mathbf{x}} + C\dot{\mathbf{x}} + K\mathbf{x} = \mathbf{F} \tag{4.1}$$

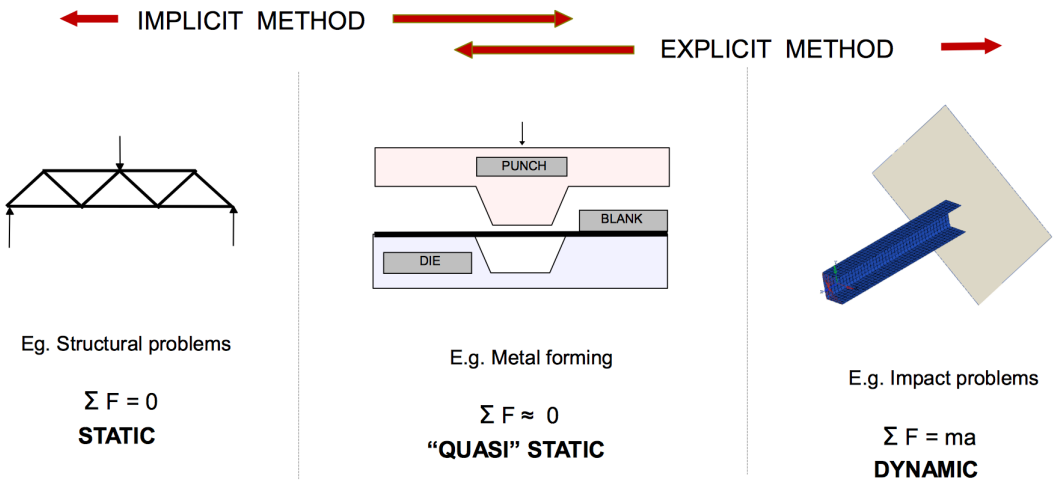

Figure 4.2: *Applications for implicit and explicit analyses.*

In an *implicit scheme*, the displacement is not a function of time. Hence the velocities and accelerations (which are time derivatives of displacement) turn out to be zero and so the mass and damping matrix can be neglected.

The implicit method can be based on Newton Raphson Method, Newark's method, etc.

In order to solve a FEM problem using implicit method, inversion of stiffness matrix K is required. Very Large deformation problems such as crash analysis can result in millions of degrees of freedom effectively increasing the size of stiffness matrix. Of course, larger the stiffness matrix longer is the computational time required for its inversion. So a method which avoids the inversion of stiffness matrix is needed.

The *explicit scheme* is opposed to implicit scheme, and is a function of time. Being a function of time, the velocity and acceleration as well as the mass and damping need to be considered in this scheme. In an explicit method, Central Difference time integration (CDTI) is used to calculate field variables at respective nodal points. Since only a numerical solution is possible for a non linear ordinary differential equation, this method is particularly suited for non linear problems. It requires the inversion of the lumped mass matrix as opposed to that of the global stiffness matrix in the implicit methods. In the CDTI, the equation of motion is evaluated at the previous time step (t_{n-1}, where t_n is the current timestep).

The explicit method or algorithm works in timestep increments which means that the displacements are calculated as the time proceeds. For example, if we consider the simulation of a crash analysis, at the first timestep (t=0 ms) there is no deformation since the simulation hasn't started yet. Gradually, as time goes on the deformation also changes. At timestep 2, "t" is equal to the time step (e.g. $t = 0.1\ ms$) and the explicit algorithm will calculate the values of field variables at time $t = 0.1\ ms$. The solution proceeds this way.

Altair HyperWorks suite has both an Implicit Solver and an Explicit Solver; the first is called Optistruct and the second is called RADIOSS.

Optistruct is a modern solver for the developing of Finite Element Analyses relative to structural problems in static or dynamic conditions; it represents the solution for market leaders for what concerns structural design and optimization.

With optistruct it is possible to make static and quasi-static analyses, non linear implicit analyses, modal analyses to solve eigen problems to find complex and real eigenvalues, frequency response analyses, fluid-structure couplings and so on.

Other than that, it is also possible to perform optimization analyses , which allow the user to find in a partial or complete automatic way the design solution which gives the best performances with respect to a certain objective and design constraints assigned.

For example, it is possible to find the thickness distribution of a component which guarantees the lighter weight (objective) respecting the minimum requirement in terms of bending stiffness (constraint).

RADIOSS is a multidisciplinary finite element solver. It can solve both linear and non-linear problems. It is a finite element solver using explicit integration schemes for the solution of engineering problems, from linear statics and linear dynamics to nonlinear transient dynamics and mechanical systems.

This multidisciplinary solver enables designers to maximize performance related to durability, NVH, crash, safety, manufacturability, and fluid-structure interaction, in order to bring products to market faster.

RADIOSS' analysis capabilities for linear and non-linear finite element analysis, sheet metal stamping, and multi-body dynamics are accessible via two input formats.

It is quite important to make the right choice for what concerns solvers, because

a bad choice could cause high computational cost and poor results.

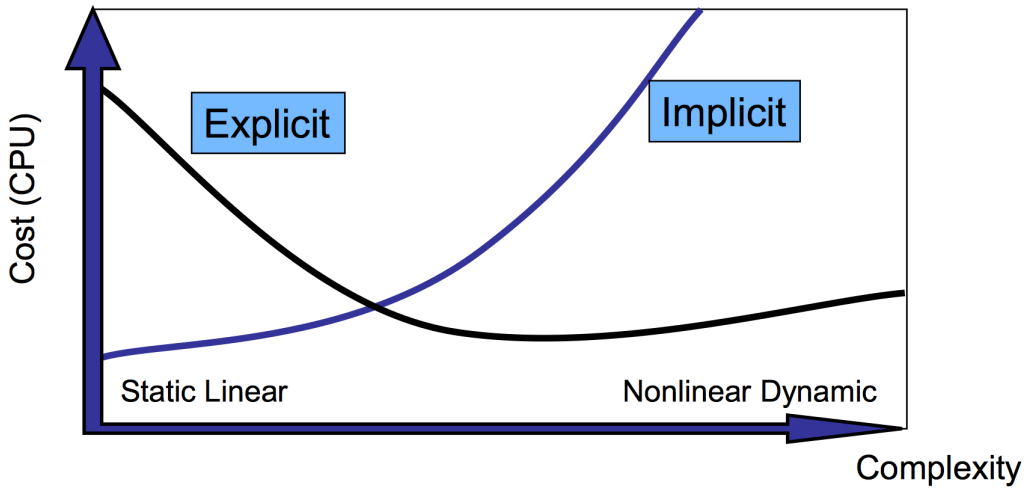

Figure 4.3: *Computational cost (time) vs Complexity of the problem. Explicit solvers are more effective than implicit one when dealing with complex non-linear problems.*

Post-processing phase

Post-processing phase is the part of the flowchart in which the user can visualize and elaborate the results of the analysis; the post processor included in the Altair HyperWorks suite is called HyperView.

HyperView gives a complete environment for post-processing and consequently for visualization of results obtained from a model solved by one of the solvers available in the market, for both FEM and multi-body simulations, allowing to elaborate digital videos and engineering data. The software combines the possibility of visualizing advanced animations and graphics or digital videos.

It is possible to make a direct comparison between the numerical and experimental results (in form of a digital video) by placing the results and the video side-by-side; it is also possible to synchronize them to make the comparison more effective.

What is more, it is possible to place side-by-side also different analyses to make a comparison and it also supports multi-window mode.

4.2 Inertia Relief Analysis

The first approach to the 3D problem was made by performing the so called *"Inertia Relief Analysis"*.

As reported in [6], *"Inertia relief analysis is regarded as an effective technique for the modeling of unconstrained structural systems"* and, as reported in Optistruct user manual, *"typical applications are an airplane in flight, suspension parts of a car or a satellite in space. This analysis type will calculate the steady-state stress and deformed shape in the structure as if it were freely accelerating due to the applied loads"*.

It is evident that the application of the light sail riding on a laser beam is in line with the capabilities of an inertia relief analysis, which at this point seems the best tool to make some preliminary analysis that will make the future complete explicit dynamics analyses more focused on the main problem.

4.2.1 Overview on the method

With inertia relief, the applied loads are balanced by a set of translational and rotational accelerations that provide body forces over the structure so that the resultant of the applied forces on the structure is zero. This provides the steady-state stress and deformed shape in the structure as if the structure were *freely accelerating* due to the applied loads. Boundary conditions are applied only to avoid rigid body motion.

Because the external loads are balanced by the accelerations, there are no reaction forces added to the problem due to the boundary conditions; the calculation is automated.

In order to activate inertia relief analysis in optistruct a control card must be added; in particular, the PARAM control card must be activated, and then the INREL parameters must be flagged.

The INREL parameter can have two values:

- **INREL, -1** - in which the *fake constraints* needed to avoid rigid body motion must be specified manually in the bulk section by using the SUPORT card;

- **INREL, -2** - in which the process of constraining the rigid body motion is automatic; every inertia relief analysis that will be shown in this work is made by using this parameter.

It is worth to underline that displacements depends on where this *"fake constraints"* are placed and so the results about displacements given by an inertia relief analysis are not reliable.

This approach was already used to determine the distribution of non-linear internal forces in aircrafts by counterbalancing rotor hub loads and was also used to estimate impact loads of a space frame structure.

What is more, inertia relief method was already used to perform a study about a squared solar sail in [7].

4.3 First studies - Geometric Linearity

Before going into a detailed analysis, following what was showed in the section dedicated to the 2D Model, it is worth to investigate about possible geometric non-linearities or numerical issues due to the fact that the thickness is much smaller than the other macro dimensions.

In this section a detailed study about the linearity of the problem was made.

4.3.1 The model

The model used to make this kind of study is a 3D model of the sphere whose surface was meshed with shell elements in order to optimize the computational cost of the analyses. This is because a mesh with tetra elements in such a small thickness would lead to huge computational cost and poor mesh and results quality; the first due to its huge number of elements needed to cover the whole shell and the second due to a poor quality of the elements due to small angles, poor form factor and so on.

In particular, a sphere with a diameter of *2 meters* was meshed with quad elements with an average size of *3 millimeters* for a total of 360460 elements and 356686 nodes.

The size of the mesh was chosen after a brief convergence study which assured that the results obtained with smaller elements are not different from the ones obtained using the current mesh. Instead decreasing mesh density, it was seen that the results obtained by a study made with the same model meshed with elements with an average size of *5 millimeters* (with respect to 3 *mm* of the current model) yielded a stress distribution quite fragmented and with a poor reliability.

What is more, the model was made by simulating the contribution of the gas with a constant pressure on the whole internal surface, and with no contribution coming from the inertia of the gas.

All the analyses in this case studies are made by resorting to inertia relief method.

4.3.2 The study

The objective of the study was that of assuring the absence of non-linearities due to the small thickness of the geometry, and for this particular purpose a simple model is enough. In particular, for this purpose the external pressure exerted on the sail due to laser beam is assumed to have a constant distribution rather than the actual four-Gaussians distribution.

Considering that the three variables of the study are *the external laser pressure, the internal gas pressure and the thickness of the shell*, the study was set by keeping one of the first two variable constants and increasing or decreasing of one order of magnitude the value of the variable left free; this was made before by keeping constant the laser pressure and varying the internal pressure and then vice-versa, starting from a standard couple of values of $p_{laser} = 300Pa$ and $p_{int} = 10Pa$. After that also four mixed cases were made by varying both the first two variables.

All these analyses were made for two thickness values, in particular for a $0.5\mu m$ and $1\mu m$ thickness.

The whole study can be summarized in the following case studies and sub-cases, in which the values of external laser pressure and internal pressure were chosen in order to be of the same order of magnitude of the values which will be used in the actual studies:

- ***Case Study "a"*** **-** In this case study the laser pressure was kept constant

to a value of $p_{laser} = 300Pa$ and the internal pressure was changed first to a value of $p_{int} = 100Pa$ (***Case Study 1a***) and then to a value of $p_{int} = 1Pa$ (***Case Study 2a***);

- ***Case Study "b" -*** In this case the internal pressure was kept constant to a value of $p_{int} = 10Pa$ and the laser pressure was changed first to a value of $p_{laser} = 3000Pa$ (***Case Study 1b***) and then to a value of $p_{laser} = 30Pa$ (***Case Study 2b***);

- ***Case Study "c" -*** In this case study the first two case studies were combined in four different ways; in particular in ***Case Study 1c*** both the variables were decreased of one order of magnitude with respect to the standard values ($p_{int} = 1Pa$ and $p_{laser} = 30Pa$); in ***Case Study 2c*** both the variables were increased of one order of magnitude with respect to the standard values ($p_{int} = 100Pa$ and $p_{laser} = 3000Pa$); in ***Case Study 3c*** the internal pressure was increased of one order of magnitude while the laser pressure was decreased of one order of magnitude with respect to the standard values ($p_{int} = 100Pa$ and $p_{laser} = 30Pa$); in ***Case Study 4c*** the internal pressure was decreased of one order of magnitude while the laser pressure was increased of one order of magnitude with respect to the standard values ($p_{int} = 1Pa$ and $p_{laser} = 3000Pa$).

The case studies described in detail above are summarized in table 4.1.

$\mathbf{p_{laser}}$	$\mathbf{p_{gas}}$	**Case Study**
300	10	standard
300	100	1a
300	1	2a
3000	10	1b
30	10	2b
30	1	1c
3000	100	2c
30	100	3c
3000	1	4c

Table 4.1: Summary of the case studies

4.3.3 The results

For each case study, an inertia relief analysis was made (using Optistruct solver) and the results were post-processed and compared within the Altair post-processor HyperView.

From the comparison of ***Case Study "a"*** (in particular the sub-cases 1a and 2a) with the standard case shown in figures 4.4, 4.5, 4.6, some useful informations about the physics of the problem can be extracted.

The distribution and the actual values of Von Mises stresses don't change so much between the three cases, and it is to indicate that the variation of the internal pressure (also if it is of two order of magnitudes) doesn't affect in a tangible way the physics of the problem, which seems to be dominated by the external laser pressure.

From the comparison of ***Case Study "b"*** (in particular the sub-cases 1b and 2b) with the standard case shown in figures 4.7, 4.8, 4.9 the consideration just made during the analysis of the first case study is confirmed. What happens is that the standard case and the case 2b ,in which the laser pressure is respectively 300Pa and 30Pa, show almost no stresses with respect to the case 1b in which the laser pressure is the highest (3000Pa).

In the end, from the analysis of ***Case Study "c"*** in its sub-cases 1c, 2c, 3c and 4c shown in figures 4.10, 4.11, 4.12, 4.13 the same concept comes back: it looks like the internal gas pressure doesn't affect at all either the distribution of Von Mises stresses on the light sail or the actual stress values.

Looking at figure 4.11 and 4.13 it is clear that both the values of stress and the qualitative distribution are the same regardless the internal pressure that varies in a range of two order of magnitudes, from 1 Pa of case 4c up to 100Pa of case 2c.

The fact that such a huge percentage change in internal pressure doesn't change at all the results in terms of stress means that it is possible to inflate the sail also at a pressure of 1Pa (rather low value), minimizing the mass of the gas included within the sail and so minimizing the whole mass of the system.

The minimization of the total mass comes necessarily from the minimization of the quantity of mass used to inflate the sail because it usually covers a large percentage (up to $70 - 80\%$) of the total mass.

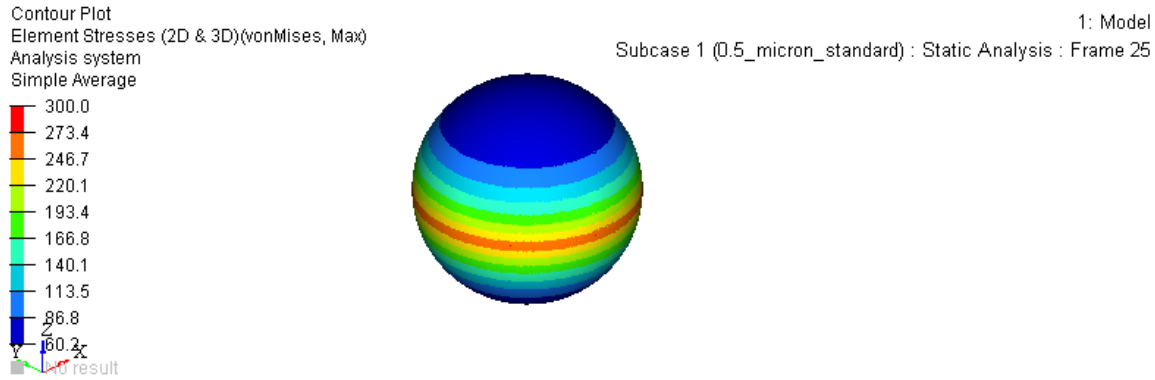

Figure 4.4: *Contour plot of the standard case, with the same scale of cases 1a and 2a (thickness of the shell $t = 0.5\mu m$).*

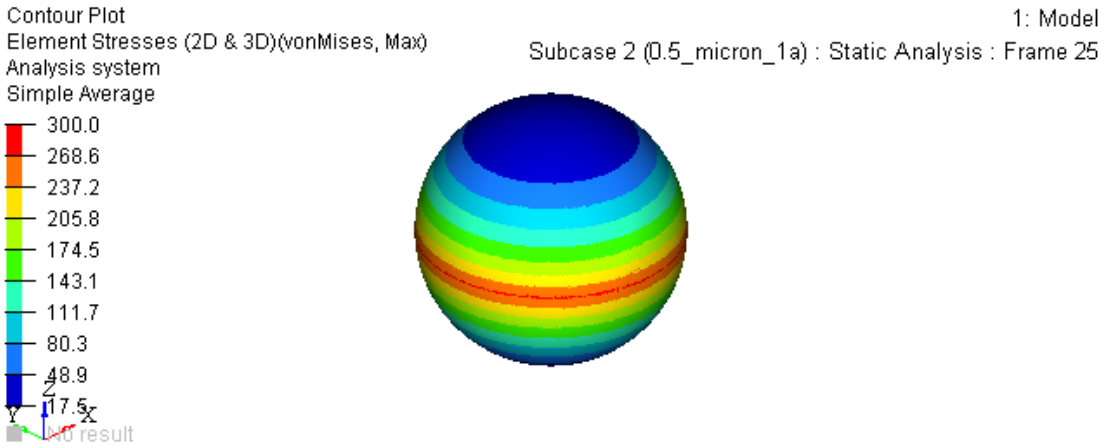

Figure 4.5: *Contour plot of case study 1a (thickness of the shell $t = 0.5\mu m$).*

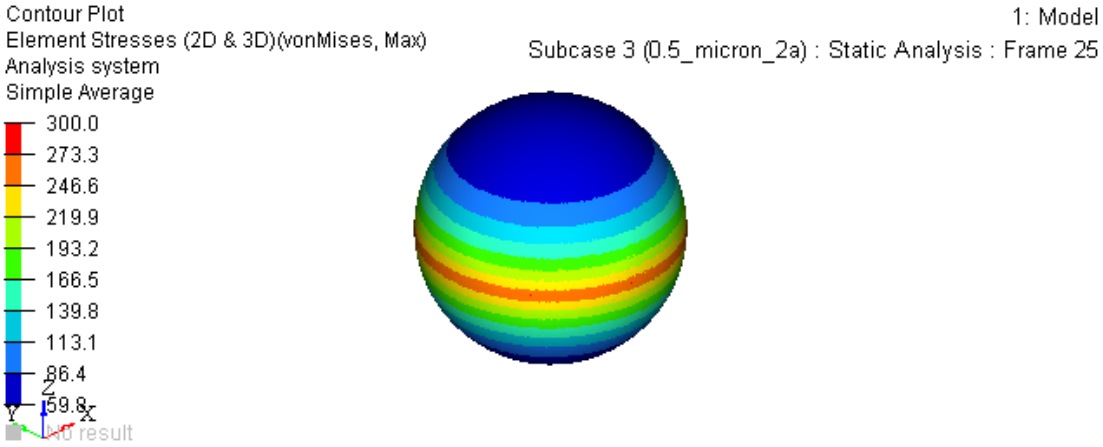

Figure 4.6: *Contour plot of case study 2a (thickness of the shell $t = 0.5\mu m$).*

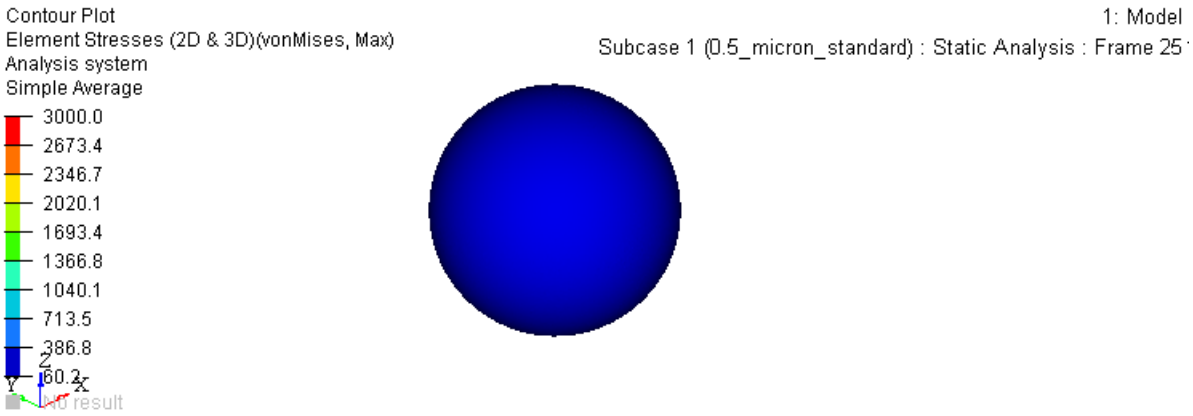

Figure 4.7: *Contour plot of the standard case, with the same scale of cases 1b and 2b (thickness of the shell $t = 0.5\mu m$).*

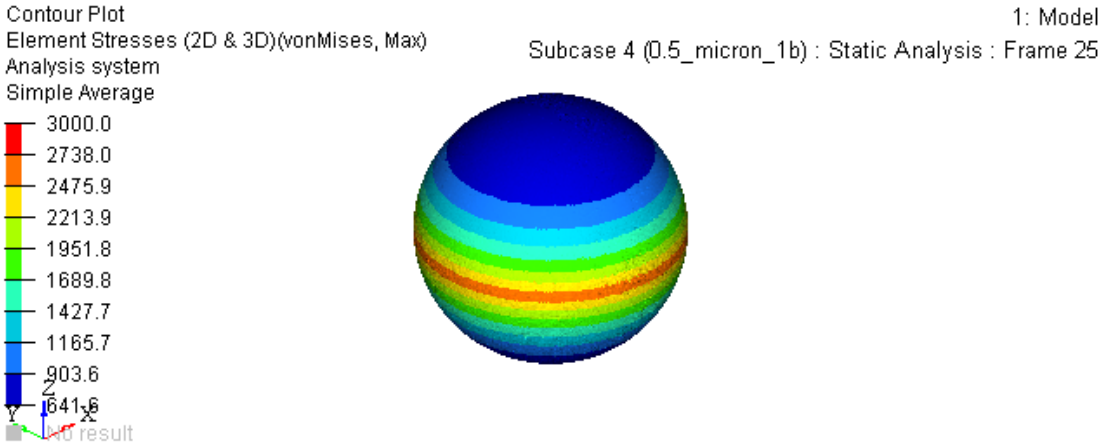

Figure 4.8: *Contour plot of case study 1b (thickness of the shell $t = 0.5\mu m$).*

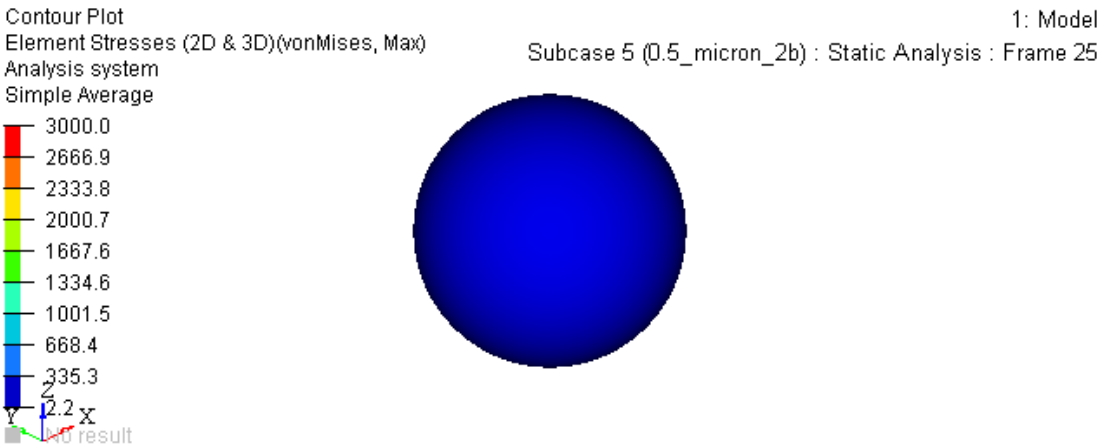

Figure 4.9: *Contour plot of case study 2b (thickness of the shell $t = 0.5\mu m$).*

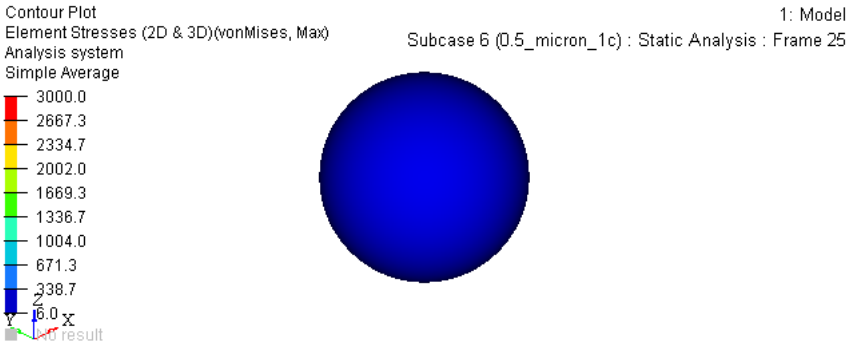

Figure 4.10: *Contour plot of the standard case, with the same scale of cases 1b and 2b (thickness of the shell $t = 0.5\mu m$).*

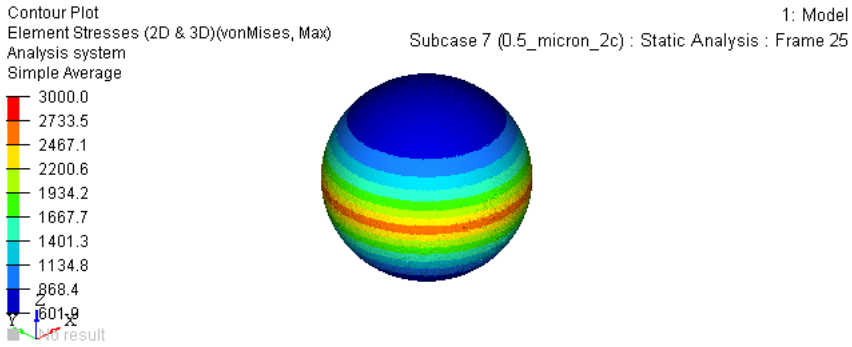

Figure 4.11: *Contour plot of case study 1b (thickness of the shell $t = 0.5\mu m$).*

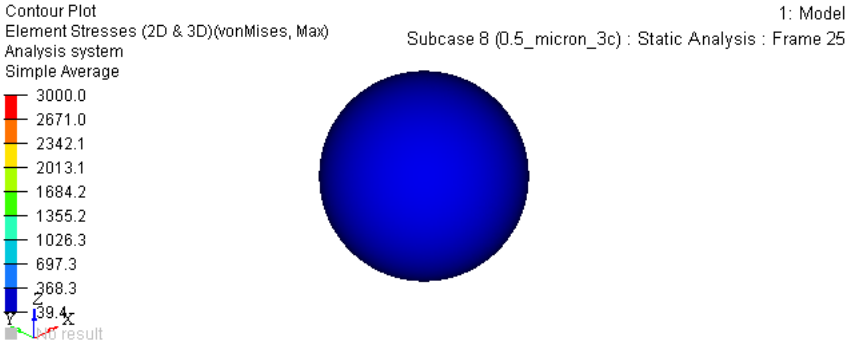

Figure 4.12: *Contour plot of case study 2b (thickness of the shell $t = 0.5\mu m$).*

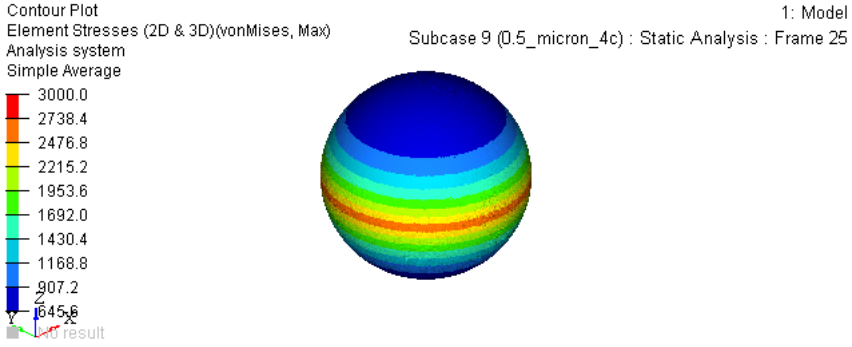

Figure 4.13: *Contour plot of case study 2b (thickness of the shell $t = 0.5\mu m$).*

As it was said before, the same study was made both on a sail with a thickness of the shell $t = 0.5\ \mu m$ and $t = 1\ \mu m$. The results for the model with $t = 1\ \mu m$ are showed in figures from 4.14 to 4.23.

The considerations made during the analysis of ***Case Study "a"*** for a thickness of $t = 0.5\ \mu m$ still holds for the case of $t = 1\ \mu m$. This is another proof in support of the fact that changing the internal pressure doesn't give almost any contribution to the stress distribution.

What is more, it can be noticed that also in this case the scales of the values are calibrated with respect to maximum values; the difference is that in this case the stress values are about halved with respect to the case of $t = 0.5\ \mu m$.

The fact that doubling the thickness the stress gets halved shows how the problem can be considered linear, so far.

Also in case of ***Case Study "b"*** the stress trends are the same for both values of thickness and the simulations yield values of stress halved when the thickness gets doubled.

For this reason the considerations made for the case with $t = 0.5\ \mu m$ still holds for the case at $t = 1\ \mu m$.

In the end, the ***Case Study "c"*** for $t = 1\ \mu m$ is analyzed. What has already been said for the first two cases is still valid: the distributions are the same of the case with $t = 0.5\ \mu m$ and the the stress values are halved with respect to the previous case.

It can be useful to specify also the maximum values actually carried out from each case study (until now only the distributions, calibrated with respect to the maximum value in the whole case study, have been plotted); also, for each case study it would be useful to plot the ratio between maximum Von Mises stress and maximum Von Mises stress in the standard case. Such informations are summarized in table 4.2 for $t = 0.5\ \mu m$ and in table 4.3 for $t = 1\ \mu m$.

It can be noted that the ratio between $\sigma_{max_{0.5}}$ and σ_{max_1} is approximatively equal to 2 for each case study, due to the fact that the thickness is doubled.

The distributions already explained multiple times above are also plotted in figures 4.24 and 4.25 for $t = 0.5\mu m$ and in figures 4.26 and 4.27 for $t = 1\mu m$.

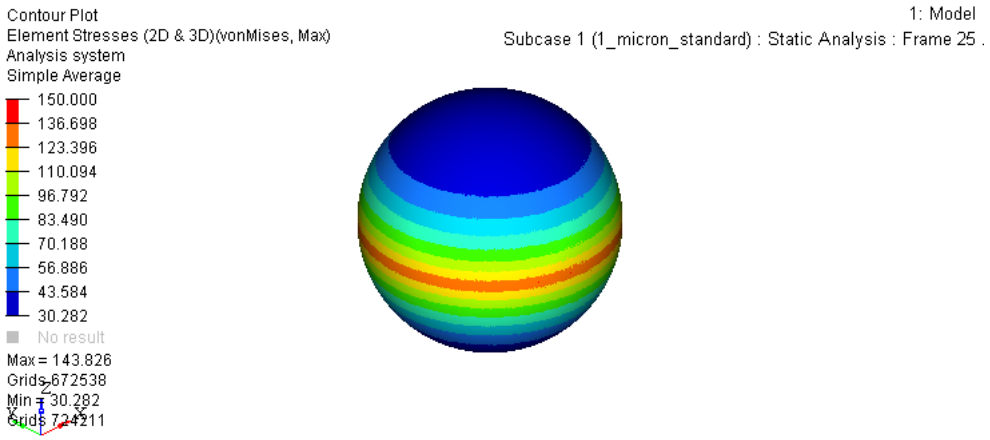

Figure 4.14: *Contour plot of the standard case, with the same scale of cases 1a and 2a (thickness of the shell $t = 1$ μm).*

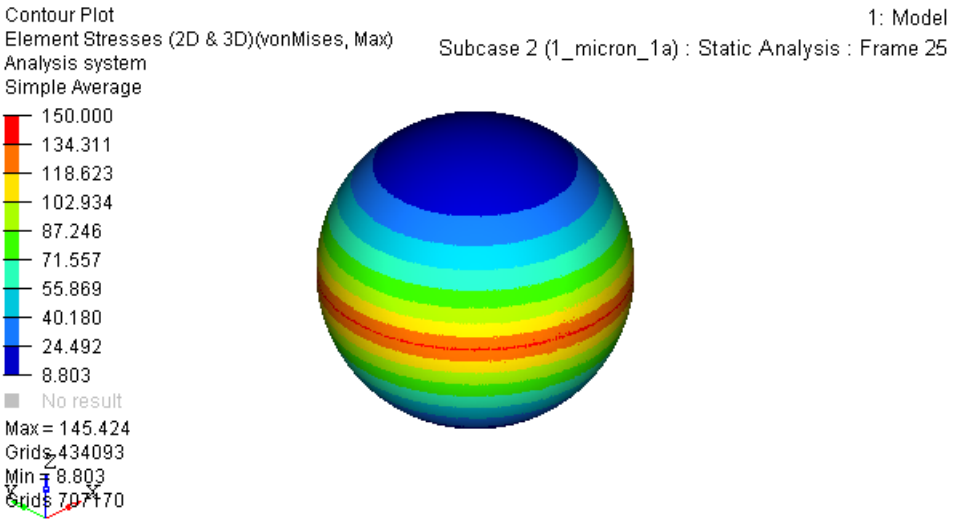

Figure 4.15: *Contour plot of case study 1a (thickness of the shell $t = 1$ μm).*

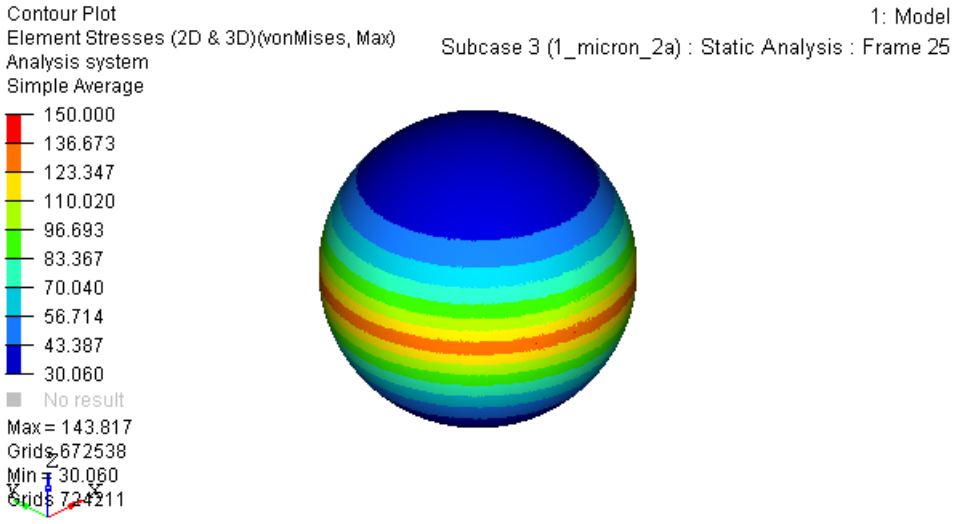

Figure 4.16: *Contour plot of case study 2a (thickness of the shell $t = 1$ μm).*

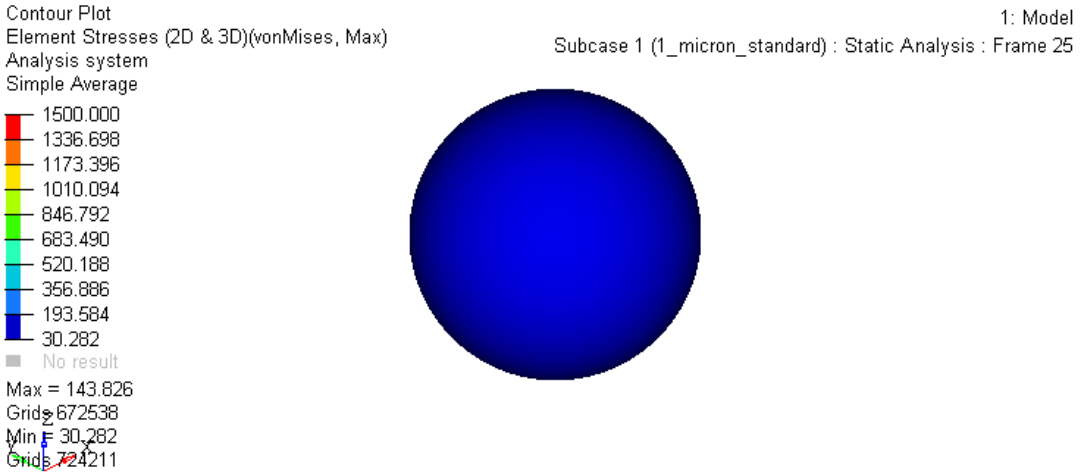

Figure 4.17: *Contour plot of the standard case, with the same scale of cases 1b and 2b (thickness of the shell $t = 1$ μm).*

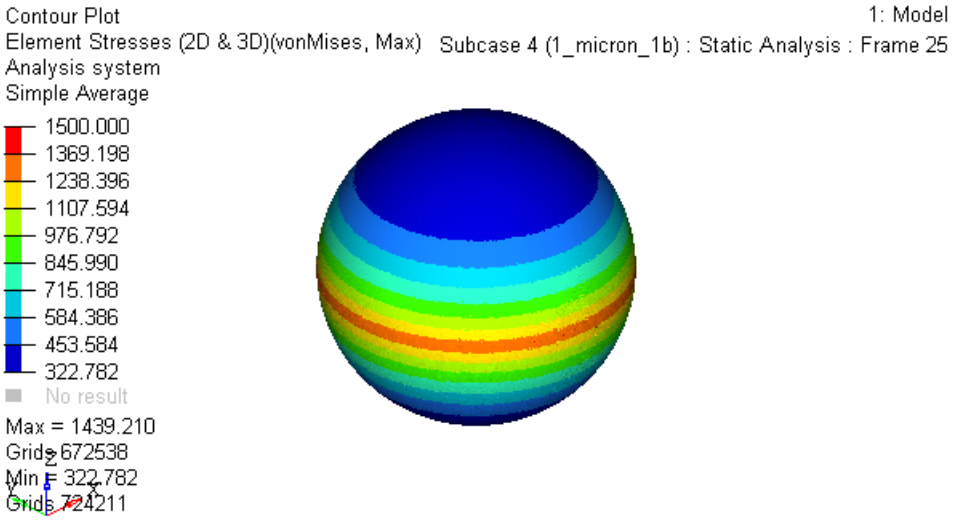

Figure 4.18: *Contour plot of case study 1b (thickness of the shell $t = 1$ μm).*

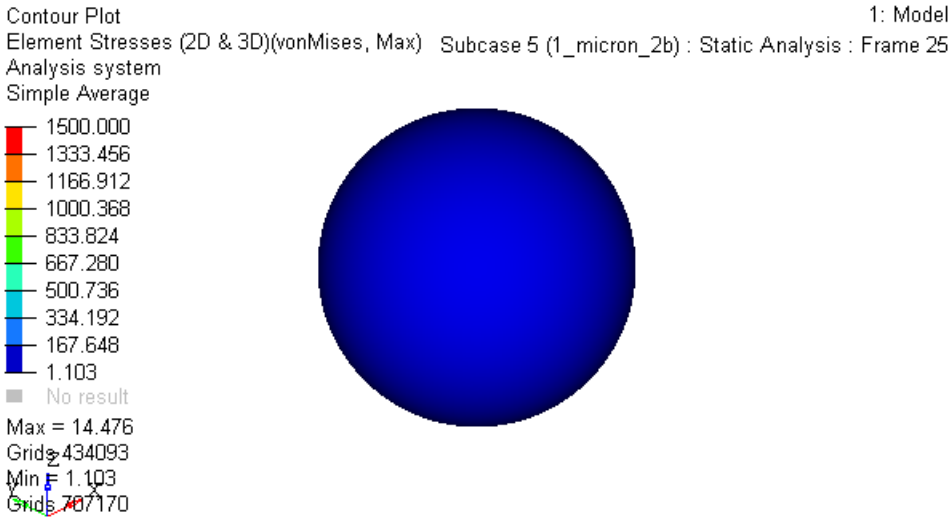

Figure 4.19: *Contour plot of case study 2b (thickness of the shell $t = 1$ μm).*

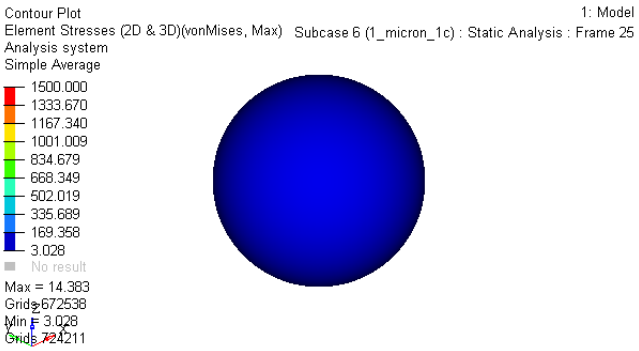

Figure 4.20: *Contour plot of the standard case, with the same scale of cases 1b and 2b (thickness of the shell $t = 1$ μm).*

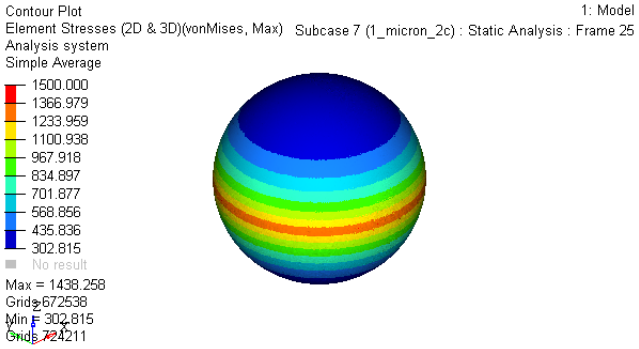

Figure 4.21: *Contour plot of case study 1b (thickness of the shell $t = 1$ μm).*

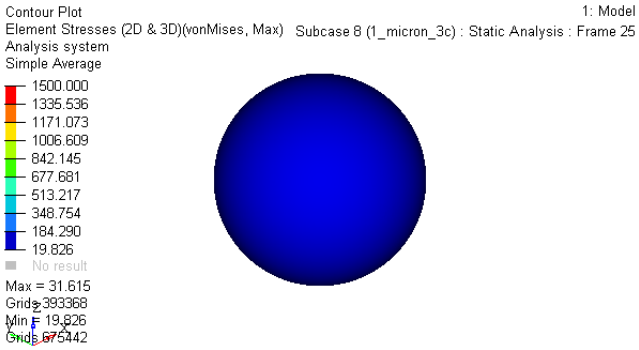

Figure 4.22: *Contour plot of case study 2b (thickness of the shell $t = 1$ μm).*

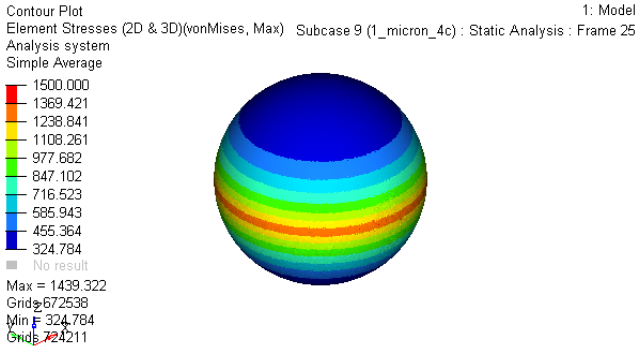

Figure 4.23: *Contour plot of case study 2b (thickness of the shell $t = 1$ μm).*

CaseStudy	$\sigma_{\mathbf{max_{0.5}}}[\mathbf{MPa}]$	$\sigma_{\mathbf{max_{0.5}}}/\sigma_{\mathbf{max_{standard}}}$
standard	287	1
1a	291	≈ 1
2a	287	1
1b	2871	≈ 10
2b	29	≈ 0.10
1c	29	≈ 0.10
2c	2869	≈ 10
3c	63	≈ 0.20
4c	2872	≈ 10

Table 4.2: Comparison of the maximum Von Mises stress in each case studies, thickness $t = 0.5\mu m$.

CaseStudy	$\sigma_{\mathbf{max_1}}[\mathbf{MPa}]$	$\sigma_{\mathbf{max_1}}/\sigma_{\mathbf{max_{standard}}}$
standard	144	1
1a	145	≈ 1
2a	144	1
1b	1439	≈ 10
2b	14.5	≈ 0.10
1c	14	≈ 0.10
2c	1438	≈ 10
3c	31.6	≈ 0.20
4c	1439	≈ 10

Table 4.3: Comparison of the maximum Von Mises stress in each case studies, thickness $t = 1\ \mu m$.

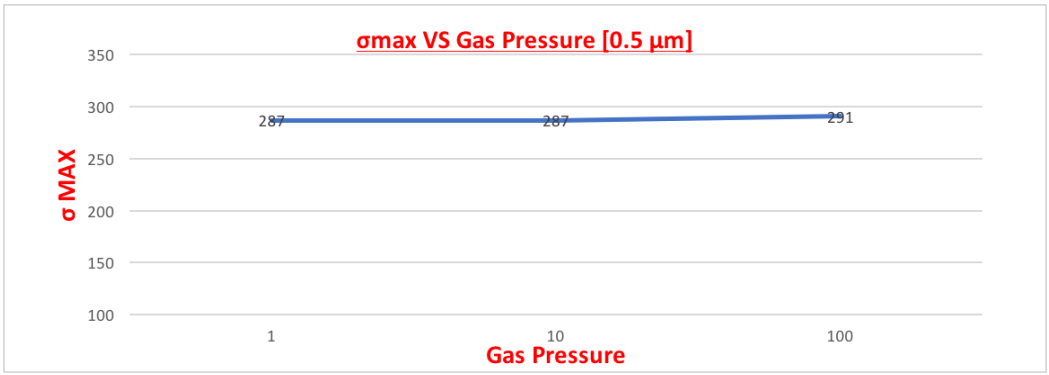

Figure 4.24: *Plot of $\sigma_{max_{0.5}}$ vs gas pressure (thickness of the shell $t = 0.5\mu m$).*

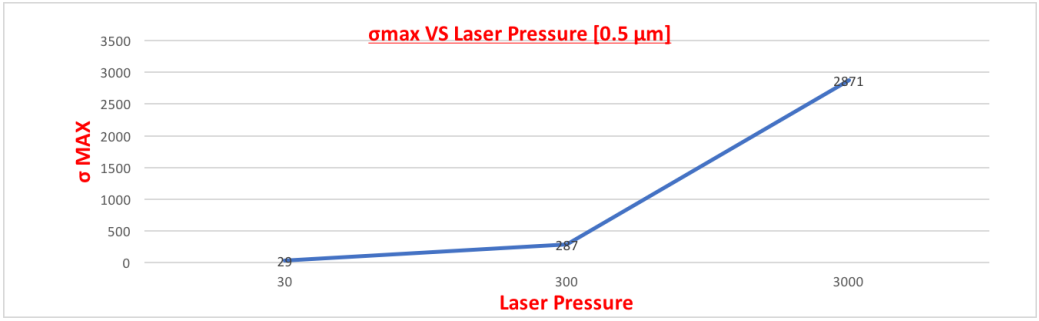

Figure 4.25: *Plot of $\sigma_{max_{0.5}}$ vs laser pressure (thickness of the shell $t = 0.5\mu m$).*

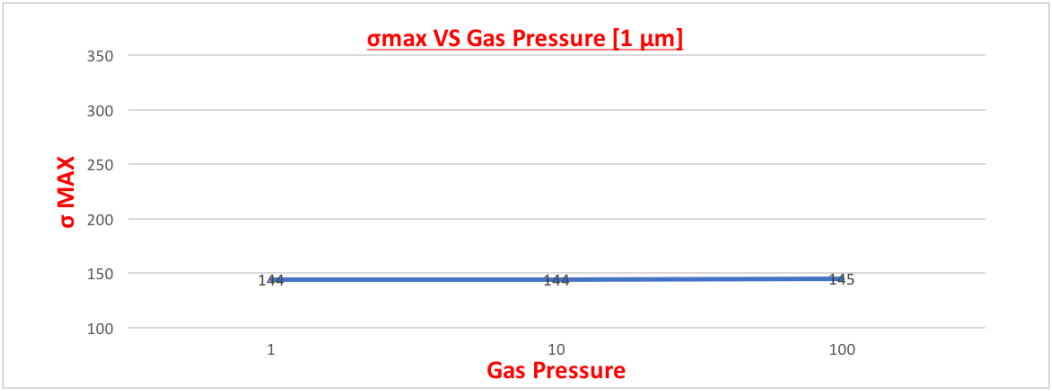

Figure 4.26: *Plot of $\sigma_{max_{0.5}}$ vs gas pressure (thickness of the shell $t = 1\mu m$).*

The fact that internal pressure does not play a key role in these simulations is due to the absence of gas inertial contribution, which at ultra-high accelerations is the most important effect related to the presence of a mass enclosed within the

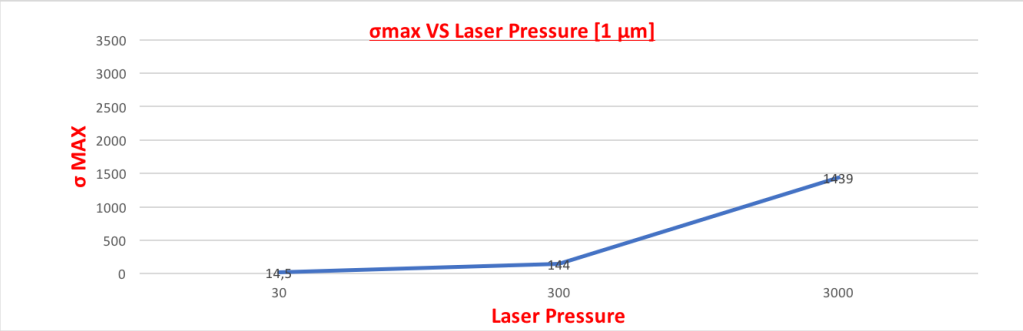

Figure 4.27: *Plot of* $\sigma_{max_{0.5}}$ *vs laser pressure (thickness of the shell* $t = 1\mu m$*).*

spherical shell. Neglecting such effect is the biggest approximation made in this study, but it is in line with the objective of such study which was made to study the geometric non-linearities of the model.

Chapter 5

Full 3D Study - Optistruct

The studies made in chapter 4 were made to investigate about possible non-linearities due to the ultra-thin spherical shell.

These studies were performed through Inertia Relief Method which allows to make linear static analysis on unconstrained bodies.

Now that the risk of geometric non-linearities has been avoided and the software has proved that it can handle this particular problems, it is necessary to go deep into the model and add the contribution of the pressure which is a function made by the sum of 4 gaussians, like it was explained in chapter 2.

The internal pressure will be kept constant, applied on the whole internal surface; this means that inertial effects of internal gas will not be taken into account during the following steps, but this phenomenon will be treated in detail in the following sections.

5.1 Modeling phase

The finite element model used to perform the study presents a substantial increment in mesh density (*Number of FE nodes* ≈ 490000 *and Numbers of FE elements* ≈ 500000) with respect to the model used in chapter 4. In addition, all the cases are made considering a value of tolerance $toll = 0$; this means that in this case the power requested to accelerate the sail (for a given acceleration) is underestimated because the portion of power outside the *"sphere shadow"* is useful

to generate a basin of attraction (so raising the dynamic stability) but it implicates an higher energy demand for a given acceleration target. In each case the quantity of flux which falls onto the semi-sphere will be the same, because it is the flux which allows to accelerate the sail to a desired acceleration and it can't change. The material used owns the characteristics already illustrated in table 2.3 and it is a standard type of Multi Layer Carbon Nano-Tubes.

5.1.1 Modeling laser pressure

The laser pressure needs to be modeled considering that, in each point, only the component normal to the surface contributes to exert a pressure on the shell. For this reason, also if the peaks of the four-Gaussians function are positioned in a zone near to the maximum radius of the sphere, only a little portion of pressure modulus (dependent from the angle of incidence) is actually exerted on the sail.

What is more, the intensity of pressure across the surface will undergo also a reduction in the frontal area, and so the intensity of the usable flux will vary as $\cos^2(\alpha)$, where alpha is both the angle of incidence and the angle of reduction of the frontal area. Such line of reasoning is applied in both planes parallels to the motion direction; in particular, assuming the motion of the sphere in **z** direction, the reduction happens both in **x-z** plane with an angle α and in **y-z** plane with an angle β (as showed in fig. 5.1 and 5.2).

A few problems were encountered in modeling this kind of reduction within the FEM code due to the fact that this operation was not automated by the software and so it was necessary to include such variation within the equation which describes the four-Gaussians function. In order to do that, it was necessary to express the angles α and β as functions of spatial coordinates **x**, **y**, **z**. From fig. 5.1 and 5.2 it is easy to write the following expressions:

$$\alpha = \arctan\left(\frac{x}{z}\right) \tag{5.1}$$

$$\beta = \arctan\left(\frac{y}{z}\right) \tag{5.2}$$

So, due to a reduction with angle of incidence and a reduction in frontal area,

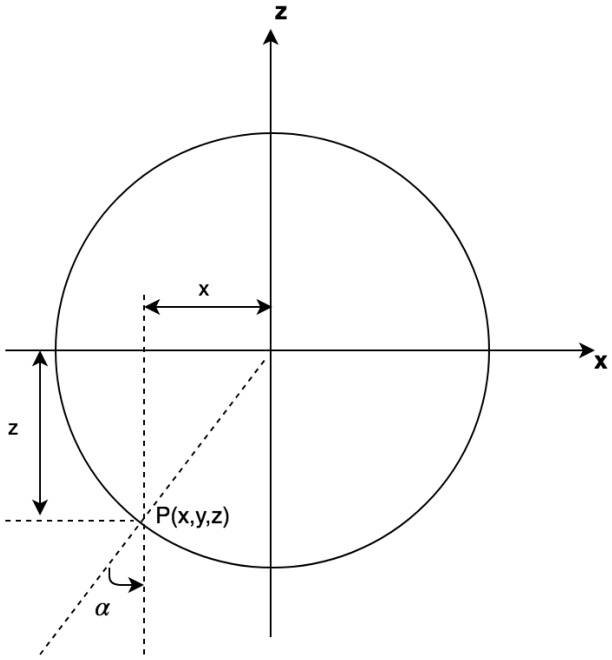

Figure 5.1: *Representation of angle α as a function of spatial coordinates.*

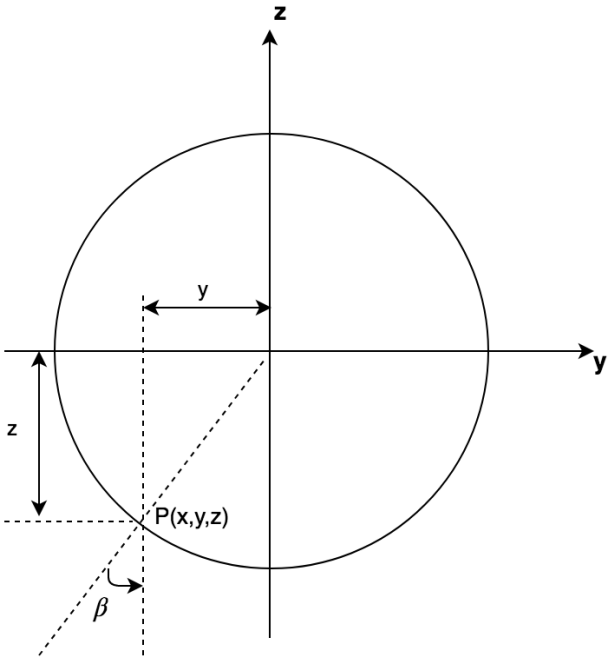

Figure 5.2: *Representation of angle β as a function of spatial coordinates.*

the scale factor which realizes the correct distribution on the outer semi-surface of the sphere irradiated by the laser beam is given by:

$$RF = cos^2(\alpha) * cos^2(\beta) \tag{5.3}$$

The product in Eq. 5.3 is able to describe the right distribution also in the equatorial zone in which the contribution of the pressure should tend to zero because the direction normal to the element tends to be perpendicular with **z** axis . In fact in the equatorial zone the angles α and β , following the way they have been defined, tend to $\frac{\pi}{2}$ and so both the cosines tend to zero.

So, such reduction factor needs to be multiplied by the function sum of the four gaussians and multiplied by the magnitude of the power flux and the resultant function must be inserted within the model in HyperMesh, applied to each node belonging to the outer surface of the semi-sphere irradiated by the laser beam .

So, following what has already been said in section 2.1.1, each gaussian component has an equation similar to:

$$f(x,y) = \frac{\exp\left(-\frac{1}{2(1-\rho^2)}\left[\frac{(x-\mu_x)^2}{\sigma_x^2} + \frac{(y-\mu_y)^2}{\sigma_y^2} - \frac{2\rho(x-\mu_x)(y-\mu_y)}{\sigma_x\sigma_y}\right]\right)}{2\pi\sigma_x\sigma_y\sqrt{1-\rho^2}} \tag{5.4}$$

and the final function ready to be inserted within HyperMesh will be:

$$equation = C \cdot f_{tot}(x,y) \cdot (cos^2(\alpha) * cos^2(\beta)) \tag{5.5}$$

in which $f_{tot}(x,y) = f_1(x,y) + f_2(x,y) + f_3(x,y) + f_4(x,y)$, C is the multiplicative coefficient which turns measure units from W/m^2 of the beam intensity to Pa of the actual pressure exerted on the beam (Eq. 5.6) .

$$C = \frac{E_f}{c}(1 + k_{refl}) \tag{5.6}$$

in which c is the light speed, E_f is beam intensity and k_{refl} is the reflection coefficient defined in 3.1.

For sake of clarity, in fig. 5.3 and 5.4 one of the four scaled distribution which comes from the equation 5.5 is showed in HyperMesh.

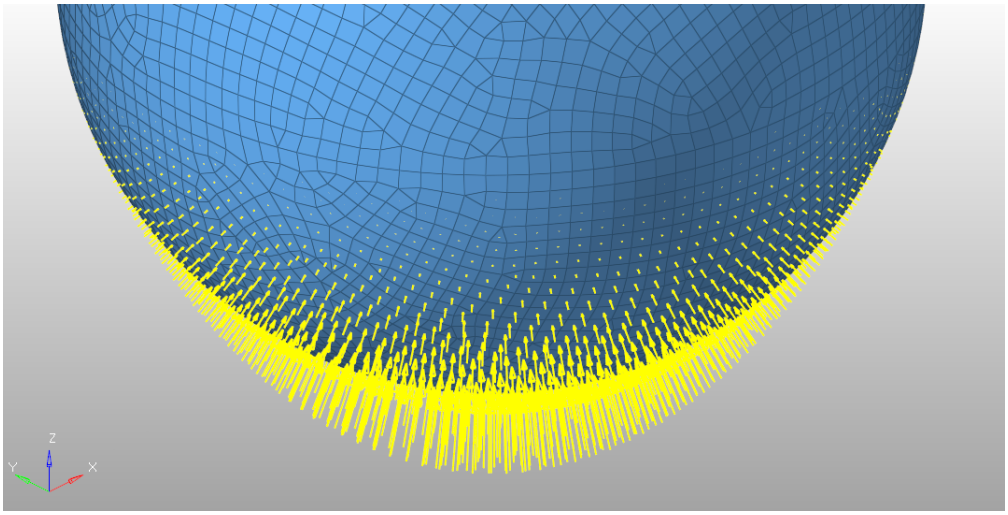

Figure 5.3: *Representation of the scaled distribution of pressure in HyperMesh: as expected the magnitude of vectors tends to zero going from the lower pole towards the equatorial zone.*

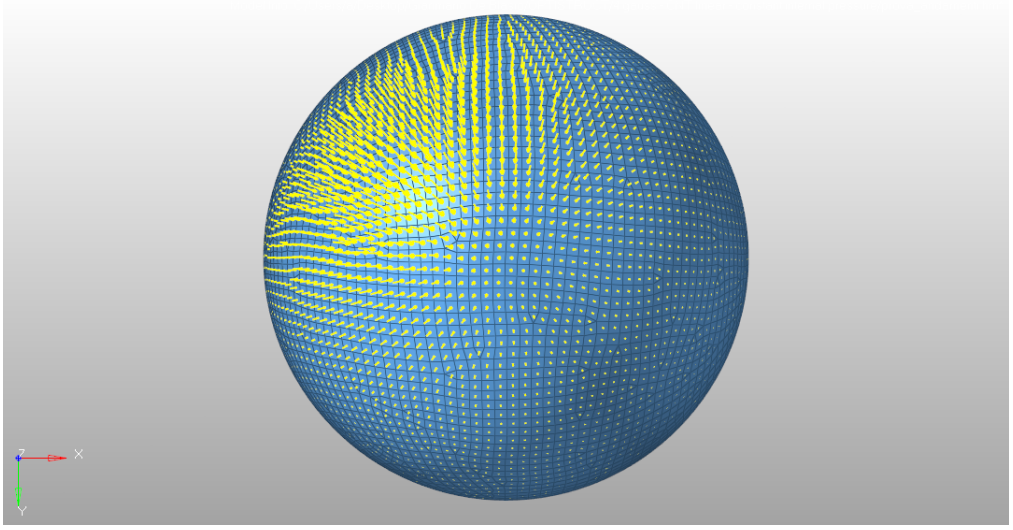

Figure 5.4: *Representation in x-y plane of 5.3; in this view the position of the peak is more visible: the gaussian plotted is the one which has both shifting parameters μ_x and μ_y negative (origin of reference frame coincident with the sphere center).*

5.1.2 Case studies

The following case studies have been studied:

	Case Study 1.1	**Case Study 1.2**
thickness [μm]	0.1	0.1
tollerance	0	0
E_f [W/m^2]	5.25e+10	2.625e+10
$E_{f_{tot}}$ [W]	7.64e+10	3.82e+10
k_{refl}	1	1
C	350	175
acceleration	30000g	15000g

Table 5.1: Summary of the Case Study 1

	Case Study 2.1	**Case Study 2.2**
thickness [μm]	0.5	0.5
tollerance	0	0
E_f [W/m^2]	2.6e+11	1.3e+11
$E_{f_{tot}}$ [W]	3.784+11	1.9e+11
k_{refl}	1	1
C	1734	867
acceleration	30000g	15000g

Table 5.2: Summary of the Case Study 2

The main difference between the two cases is that case study 1 is based on a sail with $t = 0.1\mu m$ and case study 2 is based on a sail with $t = 0.5\mu m$. This difference, of course, brings a difference in the mass which in the first case is $m = 1.7g$ and in the second case $m = 8.5g$. It is a huge difference in percentage, but it is worth to underline that no contribution of the gas is still present, so the sail is substantially lighter with respect to the actual case.

Although the gas mass is not materially present into the model, a constant pressure acting on the whole inner surface has been inserted manually, also if it is not so close to the actual case due to the absence of inertia effects which should be quite important at ultra-high accelerations.

What is more, the laser pressure value in the model is referred to a case in which the mass of gas is not present and so it is not the actual value of pressure needed to accelerate the system to the desired acceleration (as in table 5.1 and 5.2).

5.1.3 Results of the simulations for Case Study 1 and Case Study 2

The results of the simulations in terms of Von Mises stress are showed in figures 5.5 , 5.6, 5.7, 5.8.

It is interesting to compare the results obtained in Case Study 1.1 and 1.2, and in Case Study 2.1 and 2.2 , but also to compare Case Study 1 with Case Study 2.

Case Study 1.1 vs Case Study 1.2

The results obtained in Case Study 1 show clearly the effect of the peaks centered along the outer circumference which has the same radius of the sphere (tollerance = 0).

On the other hand, the red circle which highlights the most stressed zone is placed in the middle of the valley between the four gaussians. This phenomenon, which can be unexpected in the first place, is due to the pressure distribution which is projected along the vector normal to each element. In fact, as it was already said before, although the maximum values of pressure are located on the peaks of the gaussians, only a little portion of that values are actually exerted as pressure on the sail because of the positioning of the peaks.

Passing from an acceleration of $30000g$ (Case Study 1.1) to an acceleration of $15000g$ (Case Study 1.2) the resultant stress is more than halved, but the behavior can be considered mostly linear as expected.

Looking at the distributions and the maximum values there is an important safety factor if we consider a $10GPa$ yield stress as indicated in table 2.3, but it decreases if we consider that the macro characteristics of the material are weaker than the micro characteristics because of the possibility of inclusions and the random orientation of the tubes, which show a particularly strong behavior only

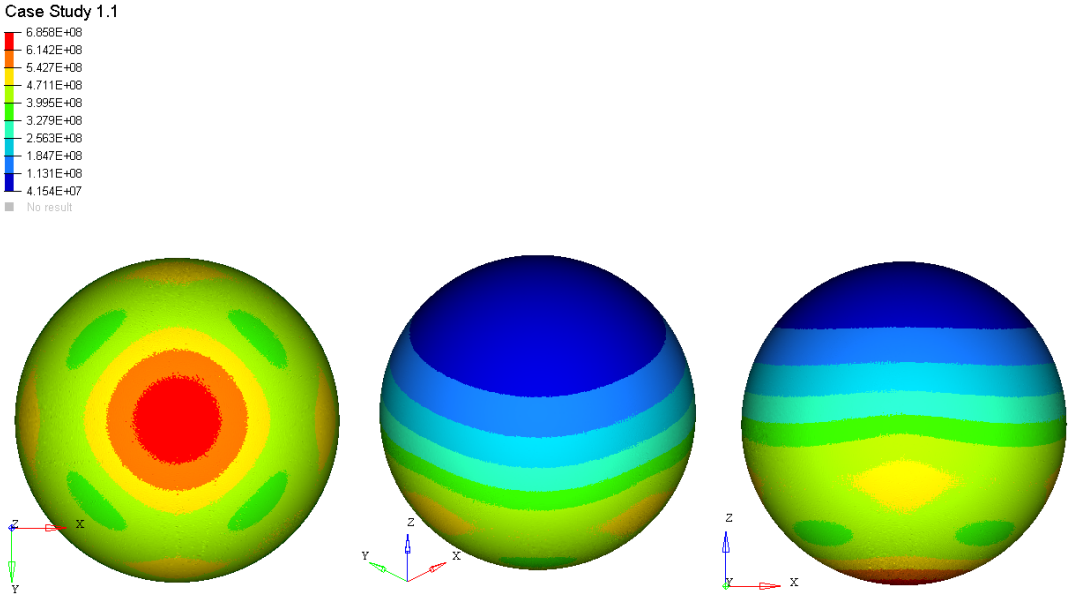

Figure 5.5: *Representation in three views of contour plots relative to Case Study 1.1 (Von Mises Stress) .*

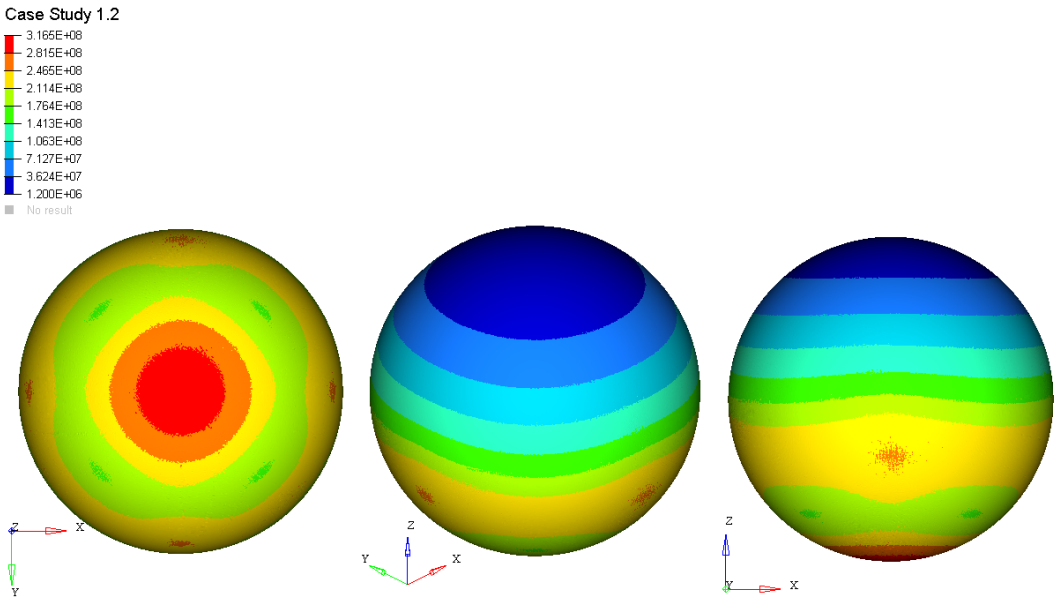

Figure 5.6: *Representation in three views of contour plots relative to Case Study 1.2 (Von Mises Stress) .*

along the axis of the tube. The result is a lower average of the characteristics that should be still far higher than the maximum stresses generated within the sail. To

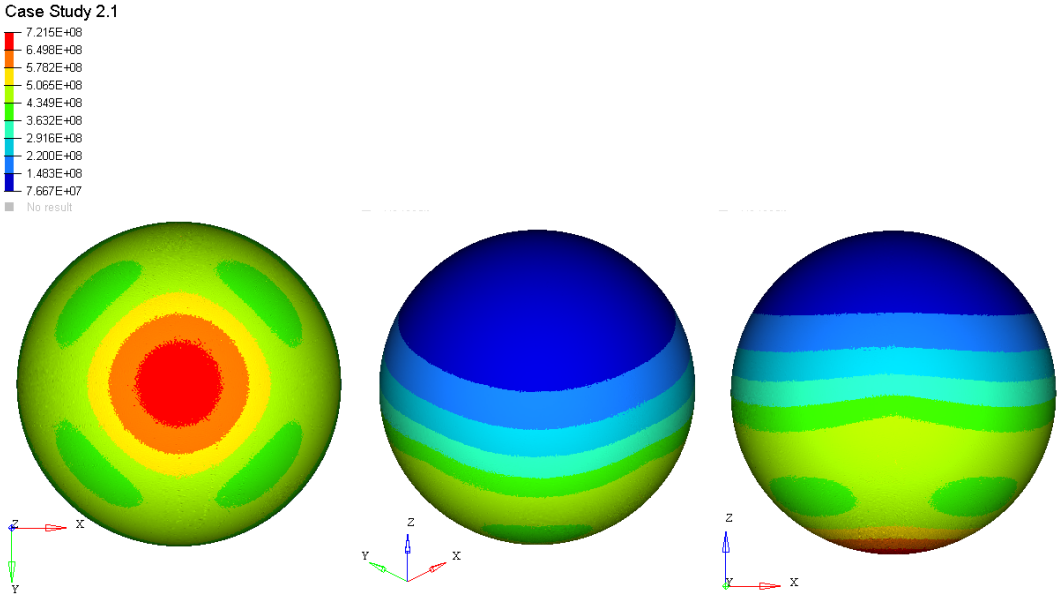

Figure 5.7: *Representation in three views of contour plots relative to Case Study 2.1 (Von Mises Stress) .*

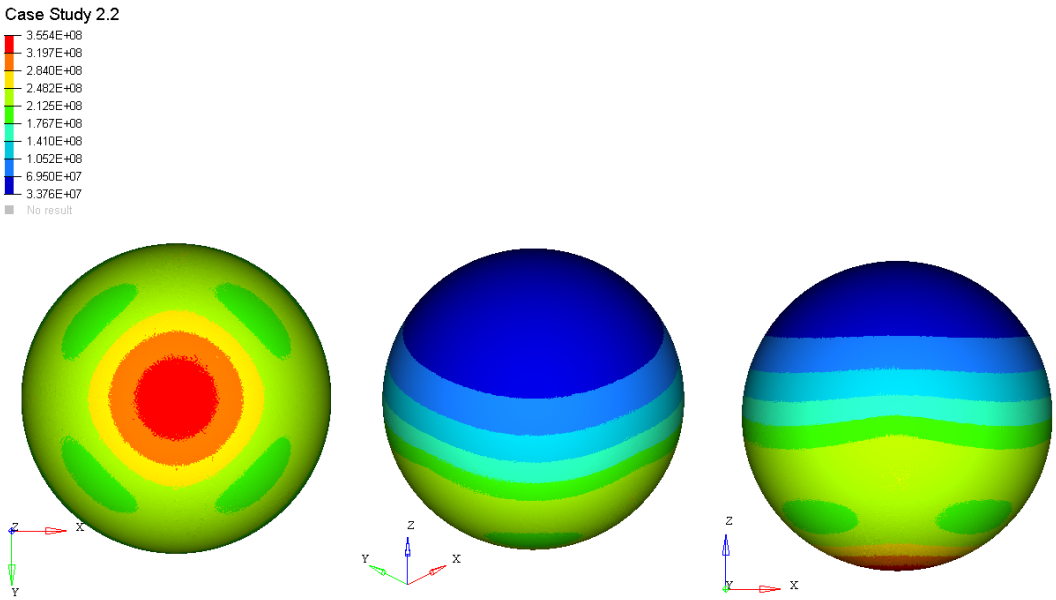

Figure 5.8: *Representation in three views of contour plots relative to Case Study 2.2 (Von Mises Stress) .*

bring out actual quantitative evaluations of the results it is necessary to develop an in-depth analysis of the material, which is not object of the present work.

What is more, although the upper part seems to have values of stress tending to zero, actually looking at the scale on the left you can see that there are values of stress just one order of magnitude lower than the maximum one.

The global distribution shows an expected behavior but doesn't take into account in a proper way neither the inertia of the shell or the inertia (and the actual presence) of the internal gas.

Case Study 2.1 vs Case Study 2.2

The considerations made for the first comparison apply also for the sub-cases belonging to Case Study 2. The distributions are very similar with respect to the previous case, but it is quite interesting to make a comparison between Case 1 and Case 2.

Case Study 1 vs Case Study 2

What is immediately clear is that, although the sail undergoes a substantial increment in thickness from Case Study 1 to Case Study 2 (*500% increment*), the maximum tension value for a given acceleration target is about 5% higher in case of 30000g and about 12.5% higher in case of acceleration target of 15000g.

The conclusion that can be made is that in this particular case the stress distribution seems to be almost thickness-independent but instead looks like it is strongly dependent on the acceleration target. This means that there is probably an upper limit to the acceleration reachable with this kind of device in a similar situation, which is probably very close to 30000g investigated in this case.

It is important to remember that the thickness of the shell, associated to the actual presence of the gas mass within the sail can reverse or partially change this kind of results and to understand in a better way this phenomenon a non-stationary explicit analysis with internal gas is essential.

5.2 Analytical model - Inertial contribution of gas

The analyses made until now didn't take into account the inertial contribution of the internal gas. Such contribution could be a *"deal-breaker"* due to the fact that in most cases the mass of the gas is far greater than the mass of the sail (e.g. in case of inflating pressure $p_{infl} = 100\ Pa$ and thickness of the shell $t = 0.1\ \mu m$ the gas mass is approximatively 81% of the total mass and about 4.3 times greater than sail mass). So a trade-off between gas mass (useful in the unfolding phase of the launch) and thickness of the shell (which contributes with its own inertia and determines the mass of the sail) must be found.

Optistruct and inertia relief analysis don't allow to model an actual gas to fill the sphere and so inertial effects can't be taken into account into the simulations. This is because the only possibility to simulate a gas within an implicit solver as Optistruct is making a tetramesh of the volume within the sphere and assigning to it a material property which can simulate the gas properties. This could be considered a valid idea, but there is a sly drawback which must be taken into account: large deformations undergone by the sail cause several numerical problems due to various factors, for example the determinant of Jacobian matrix can become negative and so on.

For this reason, an idea to solve this problem and to run a complete simulation could be that of building an analytical model which describes the density field (and consequently the pressure field) within the sphere; a density decreasing from the irradiated surface towards the free opposite surface is expected, due to inertial effects of gas mass. Such model should yield an equation for the pressure field, ready to be inserted into the model as a pressure equation in HyperMesh, and useful to integrate inertial effects of internal gas into the analyses.

5.2.1 Simplified analytical model - Cylinder model

The objective of this section is to obtain an analytical model able to describe the pressure field generated by inertial effects of internal gas, which should apply an overpressure (if compared to the inflating pressure) on the inner surface of the irradiated semi-sphere.

Developing an analytical model which yields a pressure field like that of our interest, in closed form and on a sphere, might be possible but seems more appropriate to make such a study on a simpler case.

For this purpose, the model illustrated in figure 5.9 is studied.

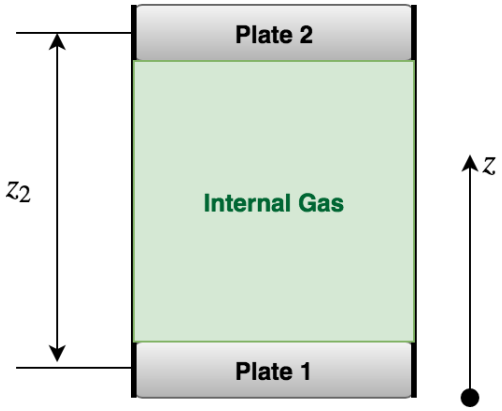

Figure 5.9: *Cylindrical mono-dimensional geometry used to develop the analytical model of the pressure field.*

This kind of geometry is made of two circular plates, plate 1 and plate 2, both of **negligible thickness**, with a mass respectively of m_1 and m_2 , with $m_1 = m_2 = M_{sail}/2$; so each plate has the same inertial properties of a semi-shell of the original spherical shell. What is more, each plate has a circular surface which is equal to the external surface of a semi-sphere and also the volume between the plates is equal to the volume of the internal portion of the sphere.

It is a mono-dimensional model with the only spatial coordinate $\boldsymbol{z}$ being part of a non-inertial reference frame centered into the circle center of plate 1, being z_2 the distance between plate 1 and plate 2 .

So, the data can be summarized as follows:

- $\mathbf{m_1} = \mathbf{m_2}$ **-** masses of Plate 1 and Plate 2, equal to the mass of a semi-shell of the spherical sail;
- $\mathbf{m_g}$ **-** mass of gas contained in the volume between the two plates;

- **A -** circular surface of Plate 1 and Plate 2, equal to the external surface of a semi-shell of the spherical shell;
- $\mathbf{z_2}$ **-** distance between Plate 1 and Plate 2;
- $\mathbf{F_{laser}}$ **-** force caused by irradiation of laser, applied on plate 1.

The free body diagram in figure 5.10 shows the forces acting on both plates; $\mathbf{p_1}$ and $\mathbf{p_2}$ are respectively the pressure which internal gas exerts on plate 1 and plate 2.

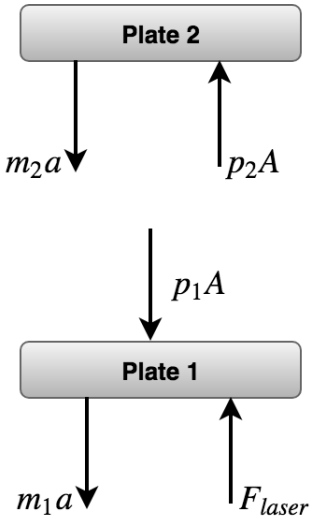

Figure 5.10: *Free body diagram showing the forces acting on Plate 1 and Plate 2.*

Looking at figure 5.10 it is possible to write the following equilibrium equations:

$$p_1 A = F_{laser} - m_1 a \tag{5.7}$$

and so

$$p_1 = \frac{F_{laser} - m_1 a}{A} \tag{5.8}$$

is the equilibrium equation for plate 1. For what concerns plate 2:

$$p_2 A = m_2 a \tag{5.9}$$

and so

$$p_2 = \frac{m_2 a}{A} \tag{5.10}$$

Another equilibrium equation which can be written is the following one, which contains also the contribution of the gas mass m_g:

$$F_{laser} = Ma = (m_1 + m_2 + m_g)a \tag{5.11}$$

in which M indicates the total mass of the system composed by the two plates and the internal gas.

The generic pressure at a generic z coordinate between the two plates can be expressed like:

$$p(z) = \rho(z)RT \tag{5.12}$$

and also as a function of the pressure p_2 and of a term similar to hydrostatic pressure but dependent from the acceleration of the system a rather than the gravitational acceleration g:

$$p(z) = p_2 + \int_z^{z_2} \rho(z) a \cdot dz \tag{5.13}$$

The equation which closes the mathematical system is the expression of the gas mass m_g as a function of density:

$$m_g = \int_0^{z_2} \rho(z) A \cdot dz = const. \tag{5.14}$$

which is a quantity that remains constant throughout the motion and is imposed by the choice of the inflating pressure, which is given as a boundary condition.

So the resolving system is the following:

$$\begin{cases} p(z) = p_2 + \int_z^{z_2} \rho(z) a \cdot dz \\ F_{laser} = Ma = (m_1 + m_2 + m_g)a \\ m_g = \int_0^{z_2} \rho(z) A \cdot dz = const. \\ p(z) = \rho(z) RT \end{cases} \tag{5.15}$$

The objective of the model is to identify a pressure field in steady state condition as a function of acceleration target.

It is possible to reach a solution in closed form of the model performing the following steps:

$$p(z) = p_2 + \int_0^{z_2} \rho(z) a \cdot dz - \int_0^{z} \rho(z) a \cdot dz \tag{5.16}$$

in which the integral $\int_z^{z_2} \rho(z) a \cdot dz$ has been divided in two components.

$$p(z) = p_2 + a \int_0^{z_2} \rho(z) \cdot dz - a \int_0^{z} \rho(z) \cdot dz \tag{5.17}$$

$$p(z) = p_2 + a \frac{m_g}{A} - a \int_0^{z} \rho(z) \cdot dz \tag{5.18}$$

in which the integral $a \int_0^{z_2} \rho(z) \cdot dz$ has been substituted by $a \frac{m_g}{A}$ resorting to constancy of the gas mass expressed in equation 5.14.

Substituting p with the expression in equation 5.12 and reordering the terms the following expression can be obtained:

$$\rho(z) RT + a \int_0^{z} \rho(z) \cdot dz = \frac{m_2 a}{A} + \frac{m_g a}{A} = const. \tag{5.19}$$

Deriving the expression just obtained with respect to axial coordinate z the integral

disappear, and the following first order differential equation is obtained:

$$RT\frac{d}{dz}\rho(z) + a \cdot \rho(z) = 0 \tag{5.20}$$

which can be written as:

$$\rho' RT + a\rho = 0 \tag{5.21}$$

Such first order differential equation admits infinite solutions of the type:

$$\rho(z) = C \cdot \exp\left(-\frac{a}{RT}z\right) \tag{5.22}$$

in which C is an integration constant. In order to calculate the actual density field is necessary to impose a boundary condition which allows to calculate the integration constant C; for this reason, knowing the pressure p acting on plate 2 in z_2, one could write:

$$\rho(z_2) = \frac{p(z_2)}{RT} = \frac{m_2 a}{RTA} = C \cdot \exp\left(-\frac{a}{RT}z_2\right) \tag{5.23}$$

The issue in applying this boundary condition is that the value of z_2 is not constant but it is an unknown function of the acceleration. In fact, if we consider a steady-state condition there will be a well defined position of the plate 2 with respect to the plate 1 for a given acceleration target. For this reason it is necessary to find a the relationship between z_2 and a which allows to find a value for the integration constant when inserted within equation 5.23.

The path to find this relationship can be found by imposing the conservation of the gas mass m_g:

$$m_g = const. \tag{5.24}$$

In particular, m_g can be written as:

$$m_g = \int_0^{z_2} \rho(z) A \cdot dz \tag{5.25}$$

and so imposing within this expression the equation 5.22, a relationship between z_2 and the acceleration can be found, although still dependent from the integration constant C:

$$m_g = AC \int_0^{z_2} \exp\left(-\frac{a}{RT} z dz\right) \tag{5.26}$$

such relationship between z_2 and a is obtained by integrating the exponential between 0 and z_2, which yields:

$$m_g = AC\frac{RT}{a}\left(1 - \exp\left(-\frac{a}{RT} z_2\right)\right) \tag{5.27}$$

and so, reorganizing the equation:

$$\exp\left(-\frac{a}{RT} z_2\right) = 1 - \frac{m_g a}{ACRT}. \tag{5.28}$$

Finally the expression of z_2 as a function of a and C is:

$$z_2(a, C) = -\frac{RT}{a} \cdot ln\left(1 - \frac{m_g a}{ACRT}\right) \tag{5.29}$$

in which the only unknowns are a and C and the other parameters are given; it can be useful to express such relationship also as a function of the inflating pressure p_{infl} which is an important parameter which must be set to determine the mass of gas which is a constant of the problem.

Now we have all the informations necessary to compute the integration constant C. It can be computed by starting from the density at the interface with plate 2 (in equation 5.23), and substituting the expression of $z_2 = z_2(a, C)$:

$$\rho(z_2) = C \cdot \exp\left(-\frac{a}{RT}\left(\frac{-RT}{A} \cdot ln\left(1 - \frac{m_g a}{ACRT}\right)\right)\right) \tag{5.30}$$

and so:

$$\rho(z_2) = C \cdot \exp\left(ln\left(1 - \frac{m_g a}{ACRT}\right)\right) = C\left(1 - \frac{m_g a}{ACRT}\right) \tag{5.31}$$

Expressing the density field as a function of the pressure field:

$$\rho(z_2) = \frac{p_2}{RT} = \frac{m_2 a}{RTA} = C\left(1 - \frac{m_g a}{ACRT}\right) \tag{5.32}$$

and isolating C yields:

$$C = \frac{a}{ART}(m_2 + m_g) = \frac{a}{ART}\left(m_2 + \frac{p_{infl}}{RT}V_{sph}\right) \tag{5.33}$$

Finally, substituting the integration constant within equation 5.22 yields:

$$\rho(z) = \frac{a}{ART}(m_2 + m_g) \cdot \exp\left(-\frac{a}{RT}z\right) \tag{5.34}$$

This equation expresses the density field within the gas mass. To switch to the pressure field as a function of z you resort to equation 5.12.

Figures 5.11 and 5.12 show the plots of density and pressure as a function of the axial coordinate z (between $z = 0$ and $z = z_2$), coming from the cylinder model just developed. What stands out is that both pressure and density (whose relationship is expressed by equation 5.12) show their maximum values for $z = 0$ (that is at the interface with plate 1), and their minimum value for $z = z_2$ (that is at the interface with plate 2) as expected.

It is worth to underline that the plots refer to a case in which the input data of the model (as m_1, m_2, m_g, etc) represents the correspondent values coming from the actual sphere. In order to make a brief validation of the model it is interesting to

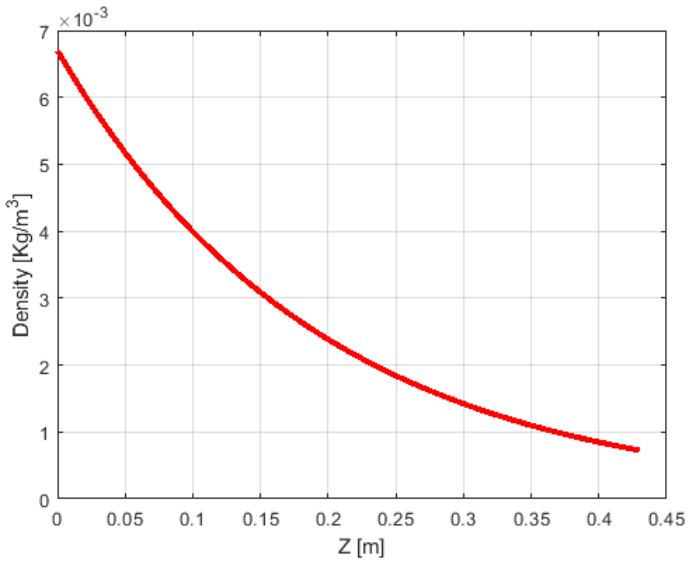

Figure 5.11: *Plot of density field developed within the cylinder as a function of the axial coordinate z, for an acceleration of 30000g.*

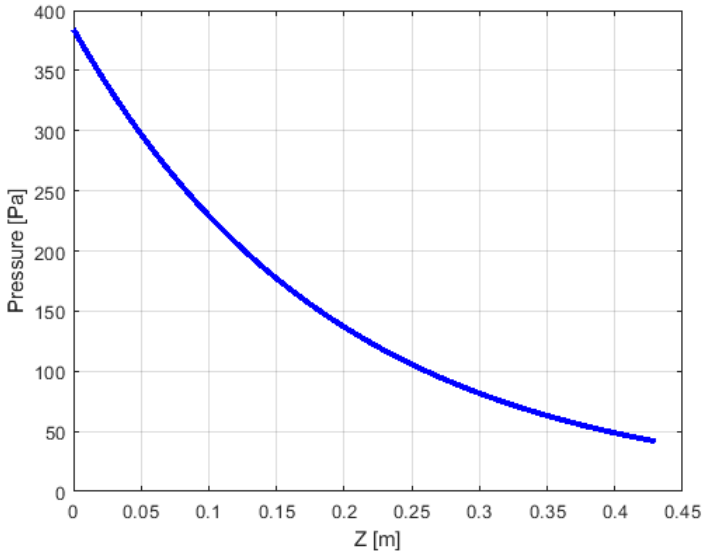

Figure 5.12: *Plot of pressure developed within the cylinder as a function of the axial coordinate z, for an acceleration of 30000g.*

plot pressure and density field in case of a lower acceleration, for example $20000g$, and in case of higher acceleration, for example $40000g$; the correspondent plots are

showed in figures 5.13 and 5.14 for $20000g$ and in figures 5.15 and 5.16 for $40000g$.

The functions show the same trends but the peak pressure and density values are proportional to the acceleration; in fact in case of $20000g$ the maximum value of density is about $4.5 \cdot 10^{-3}\ kg/m^3$ and the maximum pressure value is about $250Pa$, both values quite smaller than the $30000g$ case. The opposite happens in case of an acceleration of $40000g$, in whose case the model yields a maximum density value of about $9 \cdot 10^{-3}\ kg/m^3$ and a maximum pressure value of about $500Pa$.

The same can be said for the value of z_2 (which in the plots is the value of z which presents the lower value of pressure and density) as it was defined in equation 5.29 which, as expected, shows an inverse relationship with respect to the acceleration; in fact it is intuitive that an higher acceleration generates a larger inertia force which pushes the plate 2 towards plate 1 (for a given $p_i nfl$ and so for a given m_g). Obviously the opposite happens with lower accelerations.

From the comparison between the results carried out from the model in case of an acceleration of $20000g$ and $40000g$ a degree of linearity can be noticed; in fact, both density and acceleration double their peak values passing from $20000g$ to $40000g$ whereas the values of z_2 get halved.

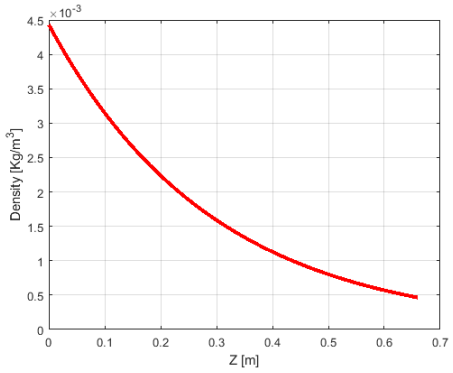

Figure 5.13: Same plot of figure 5.11, but for an acceleration of 20000g.

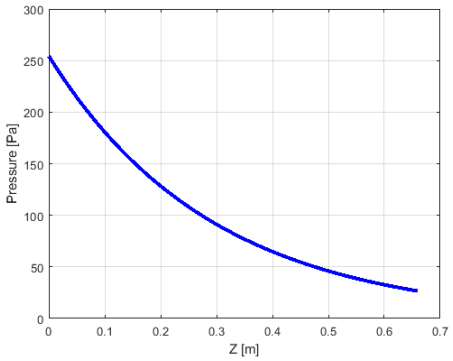

Figure 5.14: Same plot of figure 5.12, but for an acceleration of 20000g.

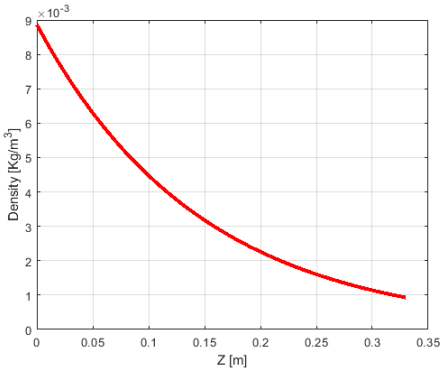

Figure 5.15: Same plot of figure 5.11, but for an acceleration of 40000g.

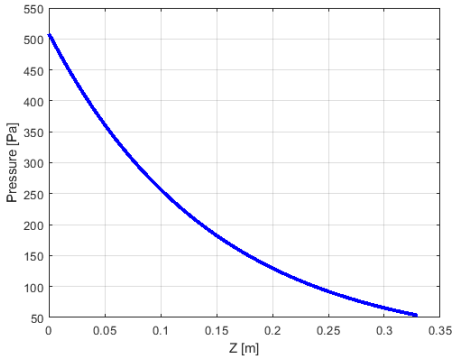

Figure 5.16: Same plot of figure 5.12, but for an acceleration of 40000g.

5.3 Implementation of the analytical model within the numerical model

The analytical model developed in section 5.2.1 was born from the necessity of taking into account the inertial effects due to the internal gas. It is an attempt of simulating (in terms of pressure field directly applied within the model) the mass of gas through its effects on the physics of the problem, without modeling the actual gas mass.

The fact that the analytical model was developed studying a simplified case and not the actual one introduces another degree of uncertainty which must be taken into account when the results are discussed. In fact, at this point it is not possible to establish wether the cylinder model is conservative or not.

The objective of the following analyses is to get as close as possible to the actual case, still performing an inertia relief analysis.

5.3.1 The model

The model has the same characteristics of the one described in section 5.1 (same mesh and so same number of FE entities), but two important changes are made in order to get more realistic results:

- ***Higher laser pressure*** **-** in this case also the mass of gas is taken into

account, so that the pressure exerted on the sail is not underestimated anymore;

- ***Inertial effects of the gas -*** in this case the inertial effects of the gas relative to each acceleration value are taken into account by implementing an equation representing the pressure field within the sphere.

The first change is implemented within the model just adapting the Gaussians functions which compose the $f_{tot}(x, y)$ with a coefficient C (equation 5.6) which take into account the higher value of E_f needed to generate a pressure able to accelerate up to the acceleration target the actual mass of the system. So, a different function for each value of p_{infl} is needed, because of the mass change.

The second modification is implemented by inserting the function of the pressure field defined by equation 5.35:

$$p(z) = \frac{a}{A}(m_2 + m_g) \cdot \exp\left(-\frac{a}{RT}z\right) \cdot RF \tag{5.35}$$

in which RF is defined by equation 5.3 and is necessary because of the reasons already explained in previous sections.

Considering that equation 5.35 comes from the mono-dimensional model of the cylinder, in which the reference frame origin is placed at the same level of plate 1, a good adaptation of such model to the spherical shell can be obtained by inserting this equation with respect to a reference frame placed in the south pole of the sphere (in a point P with coordinates $(0, 0, -1)$ with respect to the inertial reference frame placed at the sphere center) as showed in figure 5.17.

Once the equation is inserted into the pre-processor, the distribution looks like the one in figure 5.18, which is represented on a mesh with less elements than the actual one, because in this way the distribution looks more clear.

The distribution shows its maximum values on for $z \longrightarrow 0$ because it corresponds to plate 1 in cylinder model but also because for $z = 0$ the angles α and β are both zeros and so the reduction factor of equation 5.3 tends to 1. Of course the distribution shows decreasing values for increasing z for the opposite reasons.

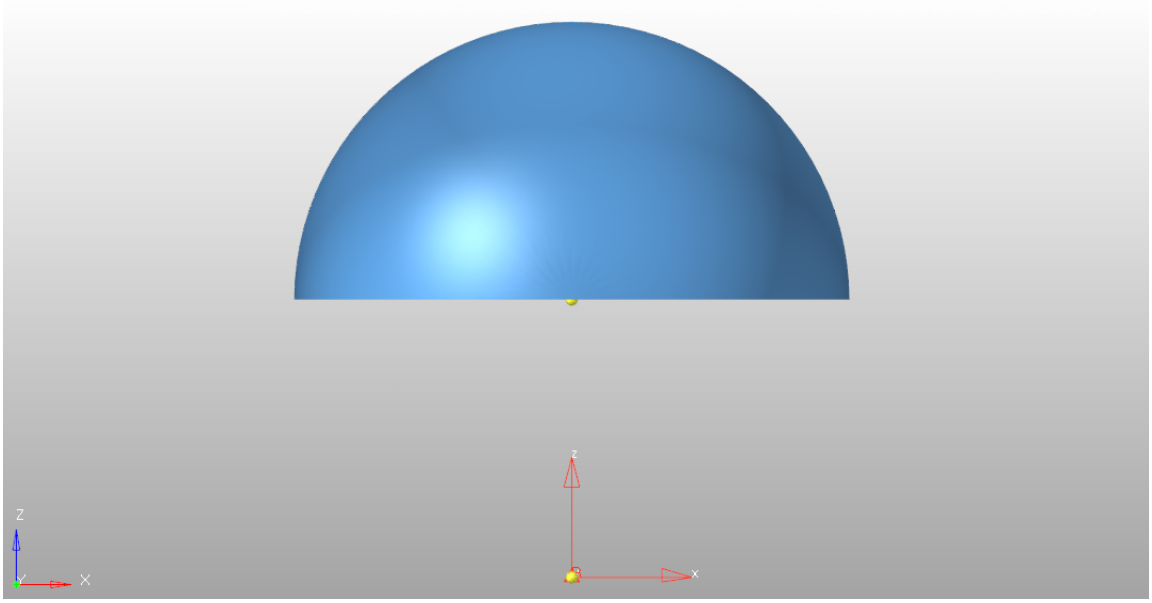

Figure 5.17: Position of the reference frame against which the equation 5.35 was implemented; the lower surface is hidden for sake of clarity.

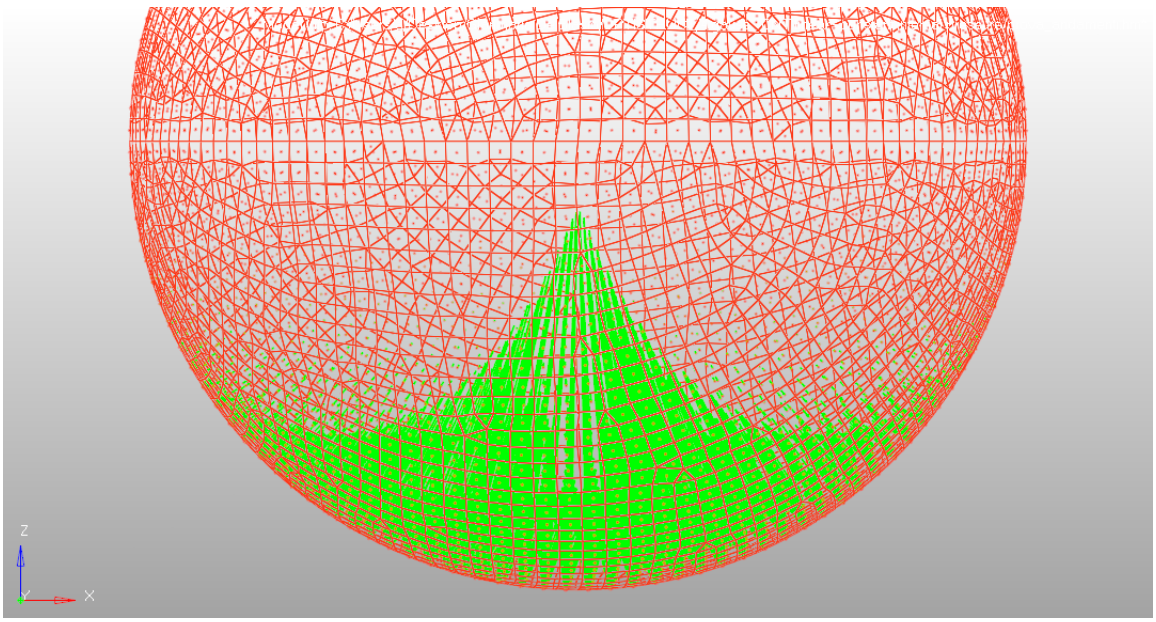

Figure 5.18: Distribution of the internal pressure, implemented using the analytical cylinder model.

5.3.2 Case Studies

The following study is the most accurate study which Optistruct allows to make in this particular case. As it was already said before, in order to take into account in the most accurate way how the gas contribution can influence the stress distribution and the structural resistance of the sail, two additions to the previous models must be considered: rising the external laser pressure so that it is referred to a mass which is the actual one ($m_{gas} + m_{sail}$) and applying an overpressure to the internal surface of irradiated semi-sphere by using the equation coming from the cylinder model.

For this reason, three new case studies (following the numbering already started in section 5.1.2) are analyzed, in which the new variable to be considered is the inflating pressure p_{infl}. In fact, for each case it is the boundary condition that determines the gas mass stored within the sail, and so for obvious reasons it determines also the power needed to accelerate the sail and the inertial overpressure caused by the gas.

Case Study 3, **Case Study 4**, **Case Study 5** are summarized respectively in tables 5.3, 5.4 and 5.5.

	Case Study 3.1	**Case Study 3.2**
thickness [μm]	0.1	0.1
tollerance	0	0
$\mathbf{E_f}$ **[W/m^2]**	2.8e+11	1.4e+11
$\mathbf{E_{f_{tot}}}$ **[W]**	4.075e+11	2.0375e+11
$\mathbf{k_{refl}}$	1	1
C	1868	934
acceleration	30000g	15000g
$\mathbf{p_{infl}}$**[Pa]** $-$ $\mathbf{m_{gas}}$**[g]**	100 - 7.3	100 - 7.3

Table 5.3: Summary of the Case Study 3

So it is obvious that, being the addition of the gas inertial contribution the main difference than the previous cases, it is the most important variable.

In addition, it can be noted that for all the sub-cases a thickness of 0.1 μm has been used, and this is because from the analyses developed in section 5.1.2 it

	Case Study 4.1	**Case Study 4.2**
thickness [μm]	0.1	0.1
tollerance	0	0
$\mathbf{E_f}$ **[W/m²]**	7.5e+10	3.7e+10
$\mathbf{E_{f_{tot}}}$ **[W]**	1.1e+11	5.4e+10
$\mathbf{k_{refl}}$	1	1
C	500	246
acceleration	30000g	15000g
$\mathbf{p_{infl}[Pa] - m_{gas}[g]}$	10 - 0.73	10 - 0.73

Table 5.4: Summary of the Case Study 4

	Case Study 5.1	**Case Study 5.2**
thickness [μm]	0.1	0.1
tollerance	0	0
$\mathbf{E_f}$ **[W/m²]**	5.5e+10	2.75e+10
$\mathbf{E_{f_{tot}}}$ **[W]**	8e+10	4e+10
$\mathbf{k_{refl}}$	1	1
C	366	183
acceleration	30000g	15000g
$\mathbf{p_{infl}[Pa] - m_{gas}[g]}$	1 - 0.073	1 - 0.073

Table 5.5: Summary of the Case Study 5

seems that this kind of thickness allows to have a sufficient safety factor for this application.

5.3.3 Results of the simulations for Case Studies 3, 4 and 5

Following the same line of section 5.1.2, figures 5.19 and 5.20 are referred respectively to sub-cases 3.1 and 3.2 of **Case Study 3**, figures 5.21 and 5.22 to sub-cases 4.1 and 4.2 of **Case Study 4** and in the end figures 5.23 and 5.24 to sub-cases 5.1 and 5.2 of **Case Study 5**.

The three cases show similar distributions for stresses but very different values.

If we compare the sub-cases of each major case study (in which $m_g = const.$), the considerations which can be done are similar to that made in section 5.1.3, that

is the stress values increase in direct proportion with the acceleration requested.

It is interesting how going from Case Study 3 towards Case Study 5 the global stress values seem to be on a decreasing trend, probably because of the the decreasing gas mass. In fact it applies an overpressure (as showed in figure 5.18) on a zone which was already the most stressed zone as pointed out in section 5.1.3, and so it contributes to stress the zone even more, also if the direction is opposite to that of the laser pressure.

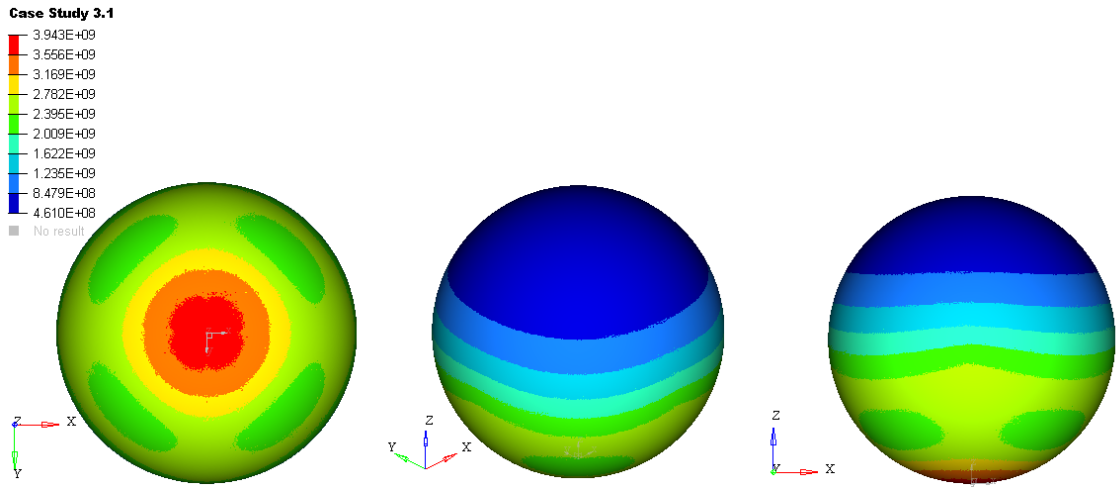

Figure 5.19: *Representation in three views of contour plots relative to Case Study 3.1 (Von Mises Stress) .*

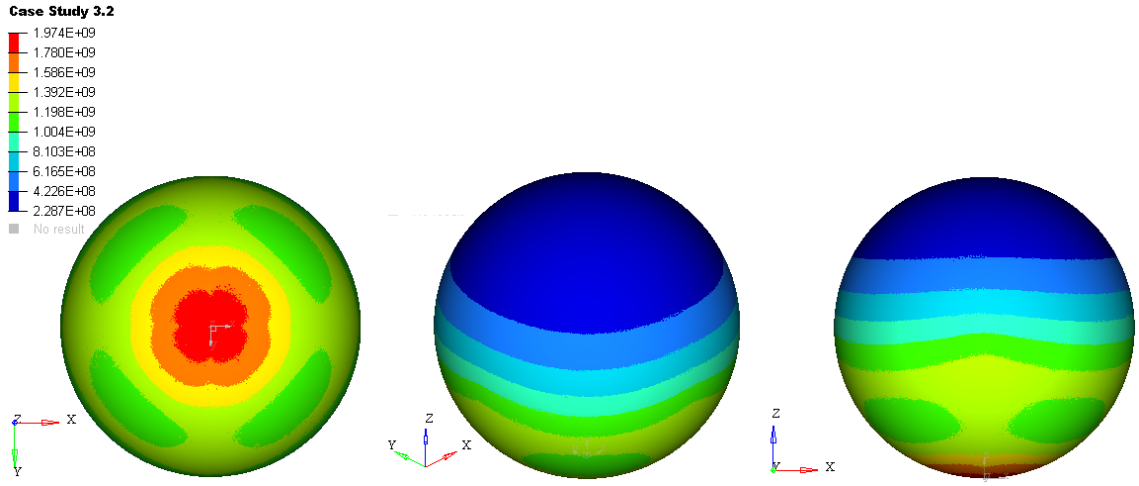

Figure 5.20: *Representation in three views of contour plots relative to Case Study 3.2 (Von Mises Stress) .*

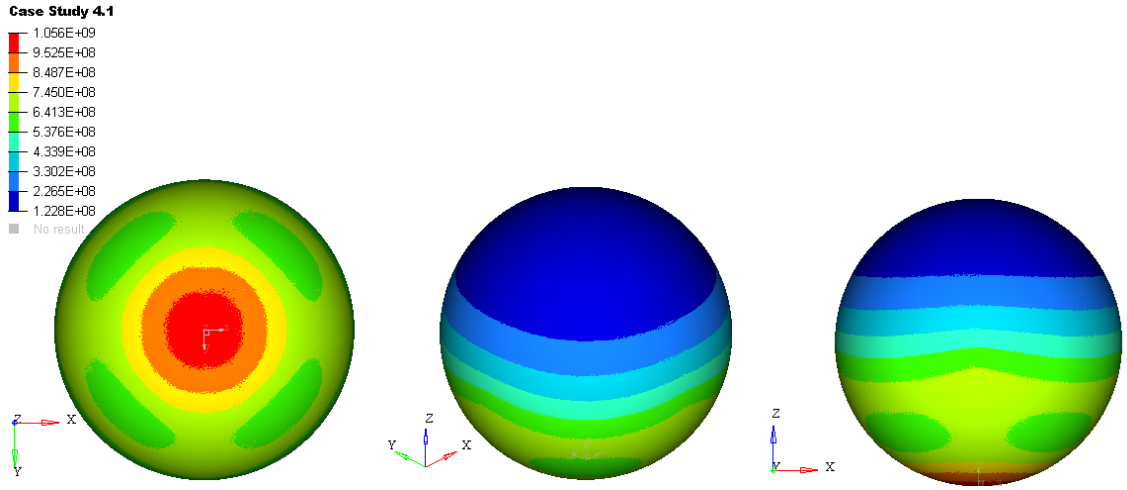

Figure 5.21: *Representation in three views of contour plots relative to Case Study 4.1 (Von Mises Stress) .*

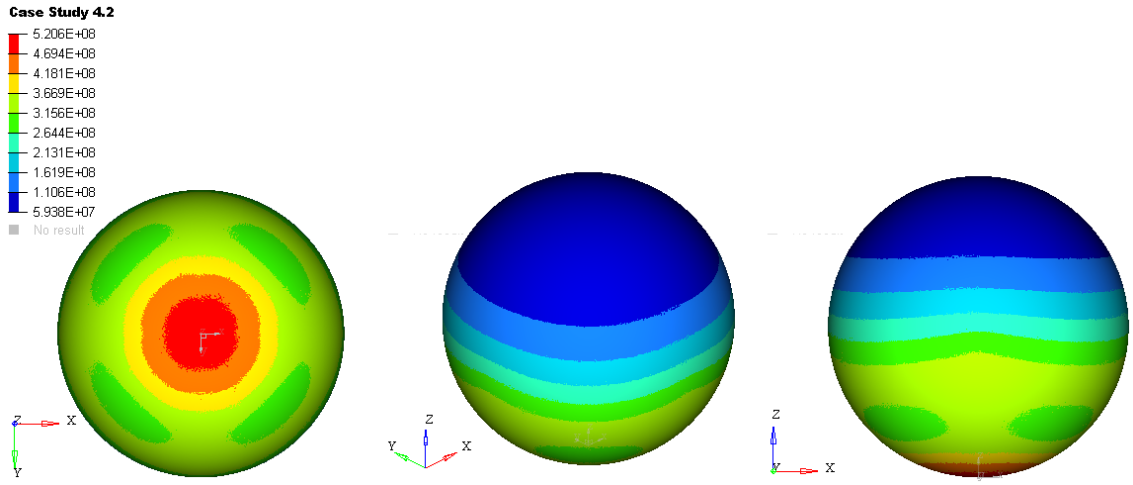

Figure 5.22: *Representation in three views of contour plots relative to Case Study 4.2 (Von Mises Stress) .*

Some other interesting comparison can be made between Case Study 3 and Case Study 1, which differ only because in Case Study 3 there is a contribution given by the mass of gas, with the consequences explained before.

What can be immediately noted is that the maximum stress is developed in the same zone but it is one order of magnitude higher when the gas is considered. In figure 5.25 a direct comparison between Case 1 and Case 3 is shown, with a homogeneous stress scale calibrated with respect to the maximum value developed

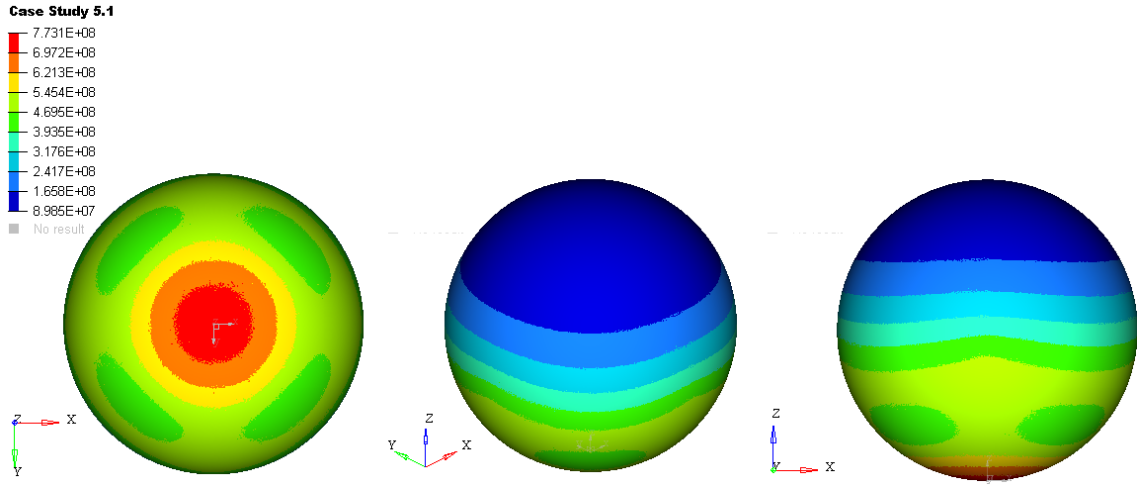

Figure 5.23: *Representation in three views of contour plots relative to Case Study 5.1 (Von Mises Stress) .*

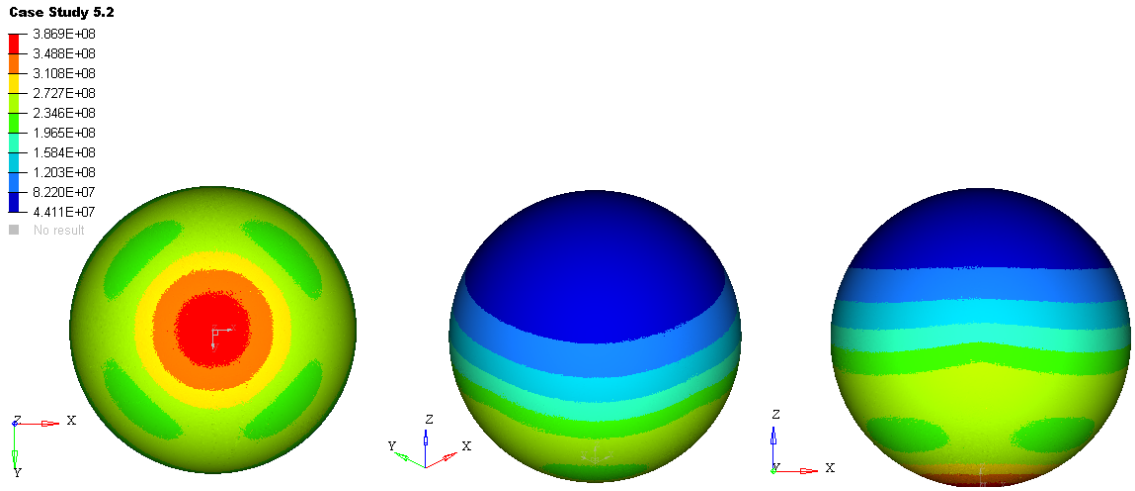

Figure 5.24: *Representation in three views of contour plots relative to Case Study 5.2 (Von Mises Stress) .*

in Case 3.

In figures 5.26 and 5.27 two similar comparisons are showed, in particular Case Study 1.1 is placed side by side first with Case Study 4.1 and then with Case Study 5.1. The results follow the logical path already marked out, showing that less is the mass of gas, less is the stress developed. In fact the values tend to be more and more similar from figure 5.25 to figure 5.27. For $m_g \longrightarrow 0$ the distribution tends to be like the one of Case Study 1.1.

So, the most important information coming from this comparison is that the presence of gas (which must be remember is needed in order to inflate and give a spherical shape to the sail) seems to have a bad influence on the stress level developed within the device, probably because the ultra-high accelerations make inertia effects very important.

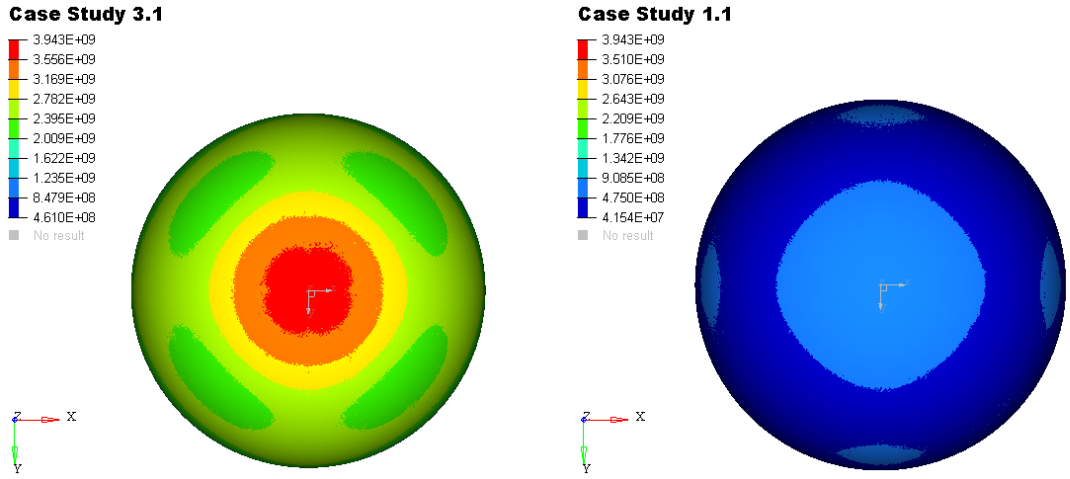

Figure 5.25: *Comparison of Case 1.1 vs Case 3.1 with a view on the most stressed zone, on a homogeneous scale (Von Mises Stress) .*

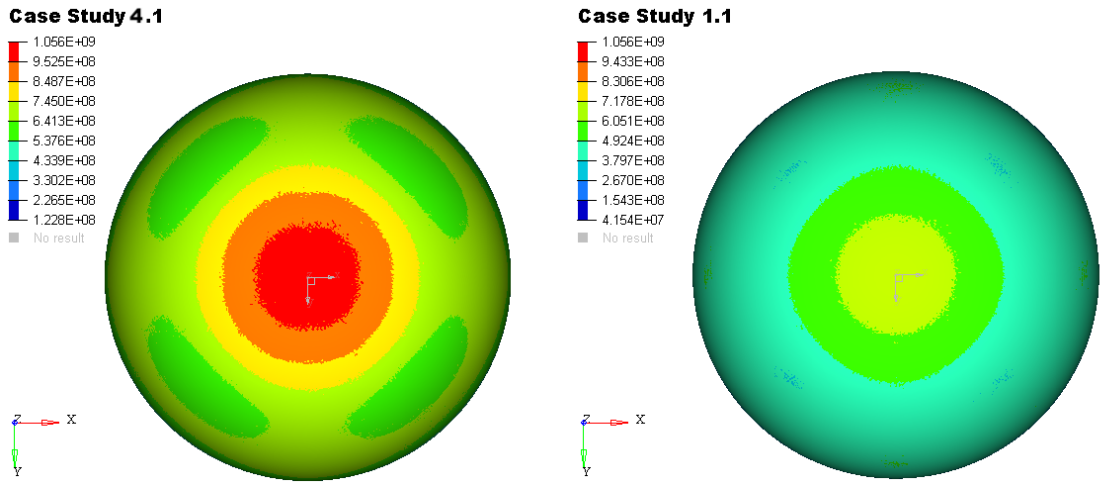

Figure 5.26: *Comparison of Case 1.1 vs Case 4.1 with a view on the most stressed zone, on a homogeneous scale (Von Mises Stress) .*

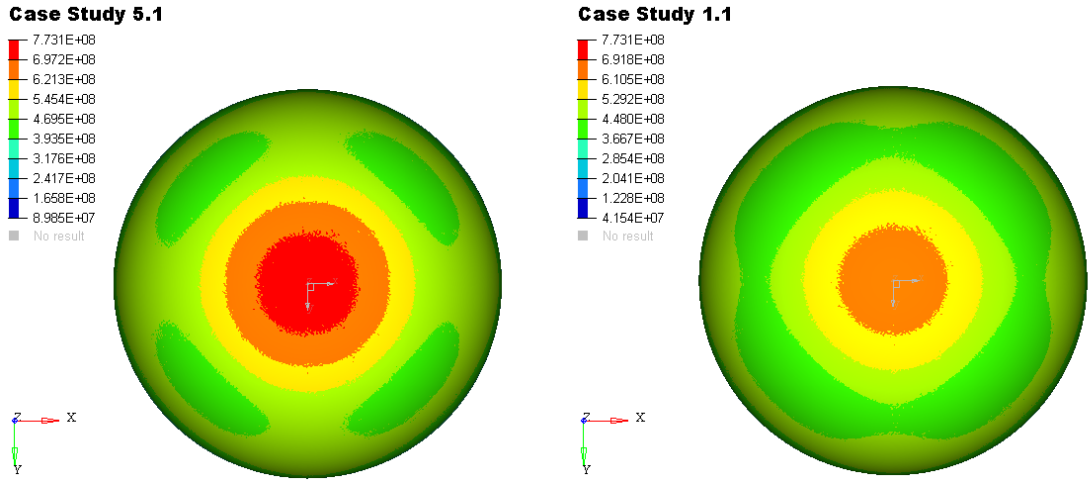

Figure 5.27: *Comparison of Case 1.1 vs Case 5.1 with a view on the most stressed zone, on a homogeneous scale (Von Mises Stress) .*

It has been said that bringing m_g to 0 the sail behaves as shown in Case Study 1, but is also interesting to show what happens increasing the gas mass. It happens that the overpressure generated by the internal gas gets so high that its effect prevails on the others and the sail undergoes a breaking in a direction opposite to the direction of motion (**-z**). A qualitative result is shown in figure 5.28, although the deformation of the sail is less accurate when the stress exceeds the yield stress because the material was modeled as a linear elastic material and we have no information on its behavior after the yield strength. So the software shows the deformations also after the yield point but it probably underestimates them, so the actual result can be substantially different if the real material shows a zone of plastic deformation.

What is really important from our point of view is that the sail undergoes stress levels higher than yield strength and so the mass of gas is a critical parameter to control in order to ensure that the sail doesn't break.

5.3.4 Conclusions

Looking at the results analyzed until now, it seems that the gas has a destabilizing effect on the sail behavior. In fact, its stress level raises due to inertial effects and so the safety factor for this particular application decreases.

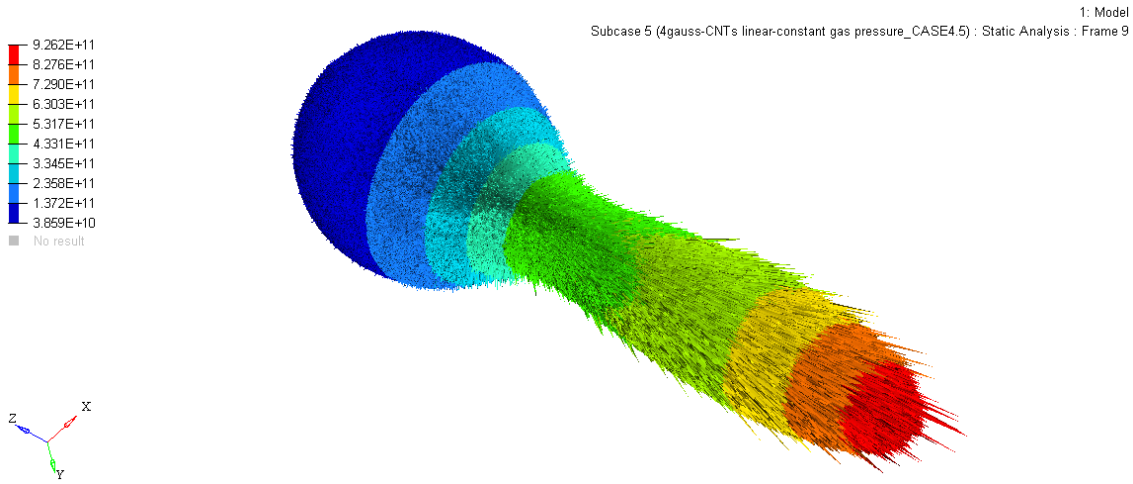

Figure 5.28: *Contour plot of a case in which the gas mass has been raised in order to show the breaking point (Von Mises Stress) .*

What is more, this effect gets more important for higher accelerations (as shown in section 5.2.1) and this confirms the fact that the feasibility of the launch is strongly linked to the acceleration desired, more than it is linked to the other sail parameters.

Finally, using a simplified analytical model developed on a different and simpler geometry leaves a further degree of uncertainty on the results; in fact, there is no way to say for sure wether this approach places us on the safe side or not. The only way to have some additional and more accurate information is to develop a model in which the gas is actually present and the effects on the dynamics of the problems are computed numerically within the Finite Element Analysis. Such study will be performed in chapter 6 .

Chapter 6

Explicit Analyses - Modeling internal gas with Smoothed Particle Hydrodynamics

The last chapter left us some doubts about the reliability of the results due to several approximations made in modeling phase. The objective of this chapter is to perform the most accurate study possible, with Commercial Numerical Analysis Codes.

In order to do that, a different approach shall be used. The analyses made until now were performed using Optistruct solver of Altair's suite, which is an implicit solver. It has a huge limit for what concerns our applications: it is not able to simulate a gas, especially for what concerns this specific application which presents an impulsive dynamics related to its huge acceleration.

An explicit solver like RADIOSS seems to suit better this application: it is able to simulate strongly impulsive events like car crashes, discretizing the problem both in time and in space. Also this solver is not supposed to be used for application like that of our interest but it seems the best option available to move in the right direction. What is more, it allows to model the internal gas with a mesh-free Lagrangian method called Smoothed-Particle-Hydrodynamics.

6.1 Explicit Solvers and applications

When dealing with unique and particular problems like that of a light sail riding on a laser beam at ultra-high accelerations, it is difficult to say a priori what kind of analysis suits better.

The static analyses made until now with inertia-relief method were useful to understand better the physics of the problem and the limits of such analysis.

An explicit solver seems to suit better the field of application , because it usually covers a field with high non-linearities and impulsive dynamics, as illustrated in figure 6.1.

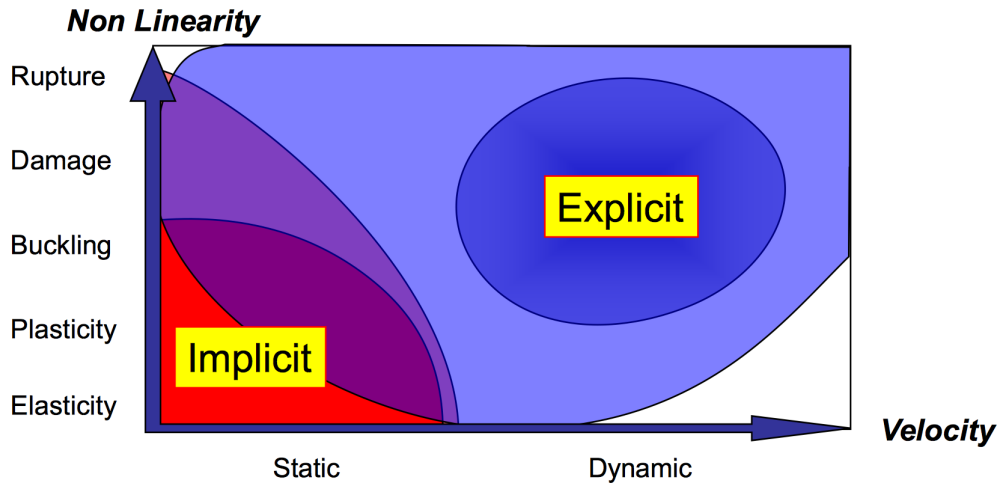

Figure 6.1: *Diagram which sums up applications for implicit and explicit analyses.* [8]

One of the critical parameters of explicit simulations is the time step Δt, which is the time required for a shock wave (which travels at the speed of sound) to propagate across the smallest distance in an element. An explicit solution is stable if:

$$\Delta t < \Delta t_{critical} \tag{6.1}$$

in which a general expression for $\Delta t_{critical}$ is:

$$\Delta t_{critical} = \frac{l_c}{c_s} \tag{6.2}$$

with l_c the smallest distance in an element and c_s the speed of sound, which is different for each material.

This means that the solution is unstable if the information goes through more than one element per time step.

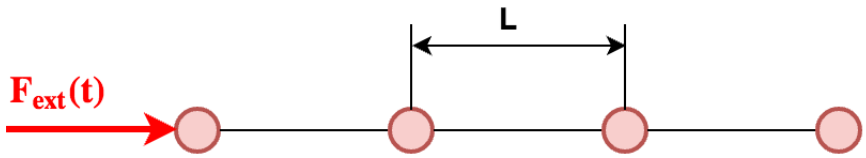

Figure 6.2: *Definition of elemental time step.*

So, stability depends essentially on two factors:

- ***Physical Factor*** **-** size of smallest element;
- ***Numerical Factor*** **-** sound propagation speed.

In order to calculate the time step it is necessary to distinguish between *Elemental Time Step* (equation 6.3) and *Nodal Time Step* (equation 6.4) :

$$\Delta t_e = \frac{l_c}{c_s} = \frac{l_c}{\sqrt{\frac{E}{\rho}}} \tag{6.3}$$

and

$$\Delta t_n = \sqrt{\frac{2m}{k}} \tag{6.4}$$

in which the speed of sound c_s is expressed as a function of the Young Modulus E and of the material density ρ, m is the nodal mass and k is the equivalent nodal stiffness.

What is more, also interfaces and contacts can control the time step during the simulation; in fact, they are essentially stiff springs.

6.1.1 Modeling a physical problem with an explicit solver

Differently from Optistruct, RADIOSS needs a whole new level of discretization which is the time discretization. In fact, space discretization of the geometry is made by using Finite Elements just like it is made in Optistruct, while the time is discretized by time steps.

Such time and space discretization can be classified in the following different formulations:

- ***Lagrangian formulation*** ($\mathbf{v_{material} = v_{grid}}$) **-** used mostly for structural analysis, with this formulation elements deform with material;
- ***Arbitrary Lagrangian Eulerian formulation* -** internal nodes move to minimize element distortion and boundary nodes remain on the boundary of the domain;
- ***Eulerian formulation*** ($\mathbf{v_{grid} = 0}$) **-** used mostly for CFD analysis (fluids), the nodes are fixed in space and the material goes through the mesh.

6.2 Smoothed-Particle Hydrodynamics

Smoothed-Particle Hydrodynamics is a computational method generally used to simulate the dynamics of continuum media, that could be fluid flows and solid mechanics. It is a mesh-free Lagrangian Method (which means that the coordinates move with the fluid), and the resolution of the method can be adjusted by acting on variables like particle density.

Such method was developed by Gingold and Monaghan and Lucy (1977) initially to be used in astrophysical field, but then it was used in many other fields of research like ballistics, volcanology, oceanography and hydraulic. [9]

6.2.1 The method

Smoothed-Particle Hydrodynamics Method is based on the discretization of the fluid by a set of discrete elements called particles. The properties of these

functions are smoothed over a spatial distance (known as *"smoothing length"* **h**) by a ***"kernel function W"*** .

A *kernel smoother* is a statistical technique used to estimate a real valued function $f : \Re^p \longrightarrow \Re$ as the weighted average of neighboring observed data, in which the weight is defined by the kernel, such that closer points are given higher weights. This is a technique which is reliable when dealing with low-dimensional data visualization purposes, which means $p \leq 3$. [10]

So, the physical quantity of any particle used to discretize the fluid, can be obtained by summing the relevant properties of all the particles which lie within the range of the kernel.

For each property, the contributions of each particle are weighted according to their distance from the particle of interest and according to their density; mathematically this distribution is governed by the *kernel function* ***W***. Some example of kernel functions used in SPH method are *Gaussian Function* and the *cubic spline (or cubic Hermite spline or cubic Hermite interpolator*); the latter is a spline (which is a special function defined piecewise by polynomials, used in interpolating problems) where each piece is a third-degree polynomial specified in Hermite form, that is by its values and first derivatives at the end points of the corresponding domain interval. [11] [12]

Differently from the Gaussian which gives a contribution for any finite distance away, the cubic spline is exactly zero for particles more distant than two times the smoothing length **h**; for this reason, the latter causes less computational costs due to the fact that the relatively minor contributions from distance particles are not included.

The equation for a quantity **A** (which can be for example the density ρ) at any point **r** is given by the equation:

$$A(\mathbf{r}) = \sum_j m_j \frac{A_j}{\rho_j} W(|\mathbf{r} - \mathbf{r_j}|, h), \tag{6.5}$$

where $\mathbf{m_j}$ is the mass of particle **j**, $\mathbf{A_j}$ and $\rho_\mathbf{j}$ are respectively the value of quantity A for j-th particle and the density associated to j-th particle, **r** is the position and **W** is the kernel function already mentioned above.

Similarly the spatial derivative of a quantity **A** can be obtained easily thanks to the linearity of the derivative (∇):

$$\nabla A(\mathbf{r}) = \sum_j m_j \frac{A_j}{\rho_j} \nabla W(|\mathbf{r} - \mathbf{r_j}|, h). \tag{6.6}$$

In order to take advantage of the full power of this method, the size of the smoothing length should not be fixed, but should be instead allowed to vary with time, so that the resolution of a simulation can automatically adapt itself with respect to local conditions; for example, in a very dense region where many particles are grouped at a small distance from each other, the smoothing length can be relatively short yielding high spatial resolution. When there is an opposite situation of a low density area, in which the particles are distant from each other and the resolution is low, the smoothing length can be increased optimizing the computation.

If combined with an equation of state and an integrator, SPH can simulate hydrodynamic flows efficiently.

Smoothed-particle hydrodynamics is being increasingly used to model fluid motion as well, because of several benefits over traditional grid-based techniques:

- ***SPH guarantees conservation of mass with no extra computation*** since the particles themselves represent mass;
- ***SPH computes pressure from weighted contributions of neighboring particles*** rather than by solving linear systems of equations like it is made in grid-based techniques;
- ***SPH directly create a free-surface for two phase interacting fluids*** since the particle represents the denser fluid (for example water) and the empty space represents the lighter fluid (for example air), whereas in grid-based techniques fluid boundaries must be tracked.

One drawback over grid-based techniques is the need for large numbers of particles to produce simulations of equivalent resolution, while another significant disadvantage is that models containing SPH require a substantially smaller time step, also due to the interfaces between them and the container.

6.3 RADIOSS model and simulations

The objective of a whole new set of simulations running in RADIOSS environment is that of beating down the simplifications made with inertia relief simulations, that are mainly the absence of an actual gas and the absence of a time discretization of such a dynamic phenomenon. Changing the solver, the model needs to be reassembled due to the substantial differences between the two solvers' logic.

In particular, making a model with the same number of elements used in Optistruct analyses will not be possible due to excessive computational cost. In fact, switching to an explicit model with the addition of the gas modeled with SPH yields unreasonable computational time if such a dense mesh is kept.

For this reason, and due to limited computing power available, the following parameters were used for the model:

- ***8321 nodes***
- ***14818 elements***
- ***3163 SPH entities (particles)***

This configuration was chosen downstream a detailed study which yielded a model with reasonable computing time, compatible with the available resources, and it was used for almost every simulation that will be showed in the following sections. It is clear that there is a dramatic decrease of mesh density with respect to the inertia relief simulations, necessary to keep within a certain limit the complexity of the problem. But there is one huge limitation coming from this new model, RADIOSS does not allow to insert functions of space like Optistruct did; this means that in the following model the only way to impose a load condition simulating the external laser pressure is to apply a constant pressure function, rather than the actual four-Gaussians function already seen in previous cases.

6.3.1 Model structure

The geometry used for this model is identical to the geometry already seen for inertia relief models. Aside from using different control cards due to the different

solver, the main difference is that in this case the internal volume of the spherical shell is *"meshed"* with SPH particles. As already specified in section 6.3, the internal volume was meshed with 3163 particles, a number which is not a random choice but comes from the definition of an SPH mesh within HyperMesh; in particular, when filling a volume with SPH, HyperMesh asks for a closed volume (which in this case is the spherical shell) and allows to set the following parameters (also the most important ones are listed below):

- ***Pitch -*** it determines the distances between each SPH particle; so smaller numbers will result in more elements within the same space, but this will not affect the mass or the density of the substance (gas, fluid and so on) that the particles represent. The choices for this field are *simple cubic* (which arranges SPH particles in groups of 8, with each particle placed in a corner of a cube) or *face centered cubic* (which arranges the particles in groups of 14, with the particles placed in the center and the corners of each face).

- ***Material Density/Filled Volume Mass -*** these options allow to specify the quantity of fluid represented by SPH particles either by specifying its density (and so the total mass is then determined by the volume filled) or specifying its total mass.

- ***Partial Fill -*** HyperMesh allows you to enable this checkbox to model a fluid that does not completely fill the selected volume (for example it can be useful to simulate the liquid fuel which partially fills a tank).

- ***Wall Clearance -*** This option allows you to create SPH particles from the specified distance. It can be useful when trying to avoid contact of SPH elements with walls at the beginning of the solver run (1st iteration) and it helps the solver running smoothly.

In our case, the number of particles was obtained by selecting a pitch of 0.1 and a filled volume mass equal to the mass of gas that we wanted to simulate (that is different for each case study), and also by imposing a wall clearance of 0.1 in order to help the solver running smoothly.

After the SPH particles have been generated, a contact interface between the shell and the particles has to be defined. For this reason a *TYPE7* nodes-to-surface contact is chosen, selecting as master surface the contact surface containing all the elements belonging to the spherical shell and as slave nodes all the SPH particles. This interface contributes substantially to decrease global time step; in fact, interface time step must be computed to insure stability. The resistive force is a function of the interface stiffness, and it is strongly non linear with respect to the penetration of the slave node into the gap (as showed in figure 6.3).

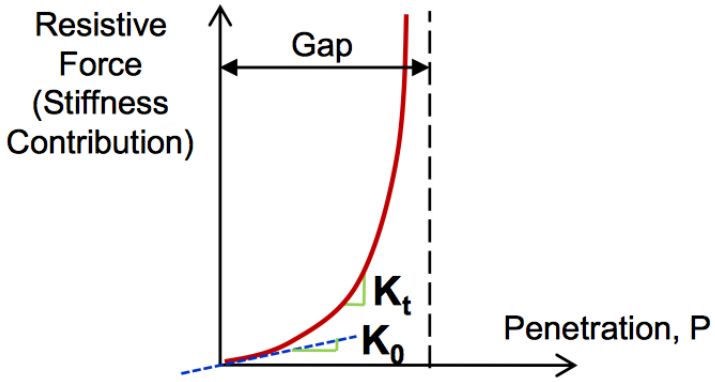

Figure 6.3: *Resistive force of the contact interface with respect to the penetration of the slave node into the gap* ($F = K \cdot P + C \cdot \frac{dP}{dt}$) . $K_t = \frac{\partial F}{\partial P}$ *is the instantaneous stiffness and* K_0 *is the initial stiffness value. [13]*

It is important that the slave node does not cross the master segment. This gives good accuracy for the node location and means that the interface time step needs to be evaluated during the solution. If there is large penetration the interface stiffness becomes large leading to reduced time step. The nodal time step during contact can be expressed as follows [13]:

$$\Delta t_{nodal} = \sqrt{\frac{2M_{nodal}}{\sum(K_{interface} + K_{element})}} \tag{6.7}$$

The contact interface between the gap can be schematized as in figure 6.4.

After the definition of the contact it is important to assign a dedicated property

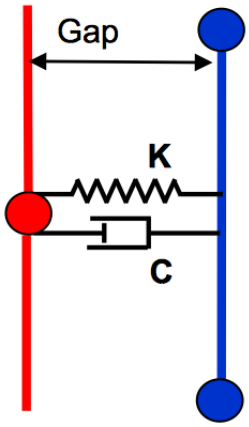

Figure 6.4: *Schematization of contact interface [13]*

.

to SPH particles, that is the kinematic viscosity $\nu = \frac{\mu}{\rho}$ expressed in $[m^2/s]$ where ρ is the density and μ is the dynamic viscosity.

A kinematic viscosity similar to that of the air is used for internal gas, precisely equal to $7.71 \cdot 10^{-6}[m^2/s]$.

The material used for the spherical shell is instead the same already seen in the previous chapters, that is Multi-Wall-Carbon-Nanotubes with the same properties seen in table 2.3.

Finally, in order to simulate the motion of the sail it is necessary to apply both the pressure necessary to accelerate the sail and the respective acceleration. Both the boundary conditions are applied on the irradiated semi-sphere so that the actual condition is faithfully represented.

It is also necessary to apply both the acceleration and the pressure as ramps and not as constant functions so that numerical instabilities are avoided.

These ramps will be always applied in such a way that the function gets to the target value in only *five milliseconds* due to the brevity of the whole simulation which will be of maximum $50ms$ to avoid unreasonable computational cost and time.

6.4 Transient phase - Case Studies and results

Following the same approach of previous chapters, in this sections all the case studies that have been analyzed will be described. The objective of the study is to compare the results carried out from the new model with the old results, but especially to understand (in the complete configuration with SPH) the effects caused by the variation of some important parameters as Young Modulus, inflating pressure p_{infl} (and so gas mass m_g), thickness of the shell t. Please note that in inertia relief analyses the elastic modulus was never taken as variable but, considering the much more complicated analysis object of study in this chapter, it might be useful to evaluate also its variation supposing that a variant of CNTs with higher elastic modulus can be produced.

Also, in all the following cases the tolerance is set to 30% in order to consider a case more similar to the reality, in which the tolerance will likely be always greater or equal to 30% in order to ensure riding stability.

The most important limitation of this solver is that it is not possible to impose an external load (i.e. laser pressure) with a variable spatial distribution (i.e. Gaussians distribution for pressure) as it was done with Optistruct. For this reason a constant pressure distribution has been imposed and this leads to consistent limitations to the model with respect to the real case.

6.4.1 RADIOSS Case Study 0

To make a clean study it is necessary to start somewhere, and in this case a configuration which was already proven to be stable with inertia relief method can be set as base case, and in the following will be referred to as ***"RADIOSS Case Study 0"***. Such case study presents data listed in table 6.1, and looking at them it can be noted that $\mathbf{E_{f_{tot}}} \leq \mathbf{E_f}$ differently from what happened in all previous case studies in which an opposite situation was presented. This is due to the tolerance which is no more zero and forces a part of the laser beam to fall out of the sphere, and so the integral on the spherical domain is smaller than the flux intensity at the source.

What is more, because of the much higher complexity of the simulations and

computational cost, only one acceleration case was investigated, and in particular a $20000g$ case.

	RADIOSS Case Study 0
Young Modulus [GPa]	200
thickness [μm]	0.1
p_{infl} [Pa]	100
m_g [g]	7.3
tollerance	30%
p_{laser} [Pa]	282
E_f [W/m^2]	3e+11
$E_{f_{tot}}$ [W]	2.65e+11
Total mass [g]	9
acceleration	20000g

Table 6.1: Summary of RADIOSS Case Study 0

Despite being a case with an acceleration 33% lower than the one used in inertia relief analyses, what can be noted from figures 6.5, 6.6, 6.7 and 6.8 is that the sphere undergoes huge stresses and so it *"explodes"* due to inertia of the gas.

In particular, at $t = 1\ ms$ the stress distribution shows a maximum in the equatorial zone of the semi-sphere opposite to the irradiated one , and almost no stress on the irradiated one. The absence of stress on the irradiated face can be explained by looking at the gas which is still almost steady, and so does not apply its overpressure yet, whereas the maximum on the opposite face is likely due to its own inertia.

At $t = 3\ ms$ the distribution changes a lot; the maximum stress increases but it is not located on the face at $y > 0$, in fact it is located in some zone on the irradiated face. This behavior is due to the movement of the gas which starts generating a pressure gradient within the sphere, with an overpressure on the irradiated face.

Of course, going ahead in time this phenomenon gets more important, as it is showed in figure 6.7 at $t = 5ms$ where the maximum stress is located on the pole at $y < 0$ because the gas tends to be pushed in that zone by the combination of its inertia and the particular spherical geometry.

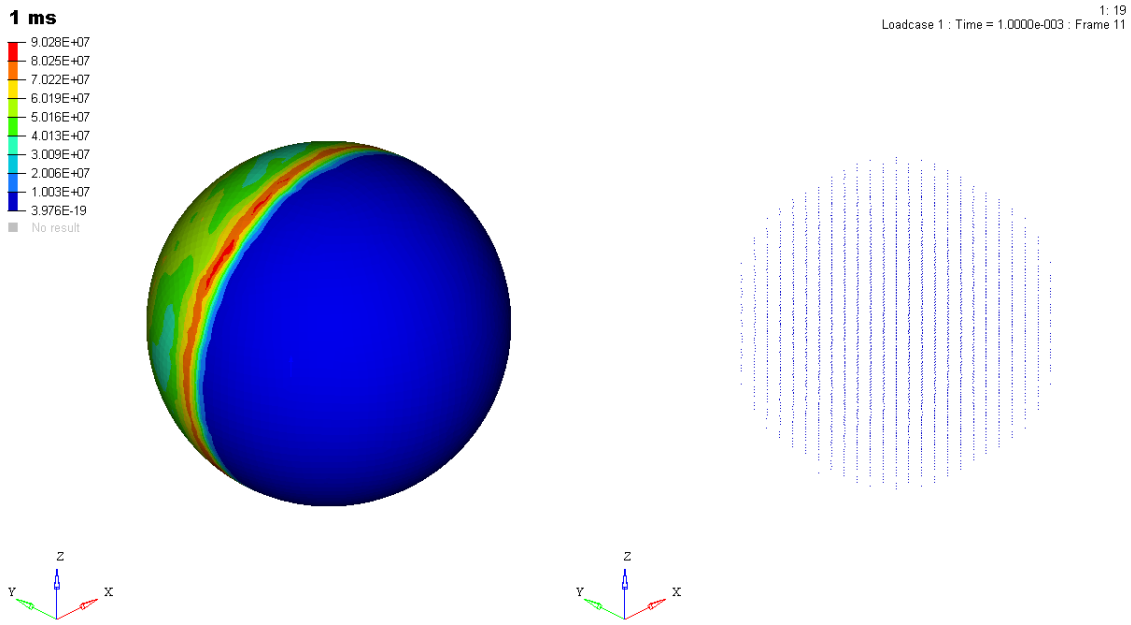

Figure 6.5: RADIOSS Case Study 0. *On the left, contour plot of the sphere at 1 ms. On the right, the representation of the internal gas at the same moment.*

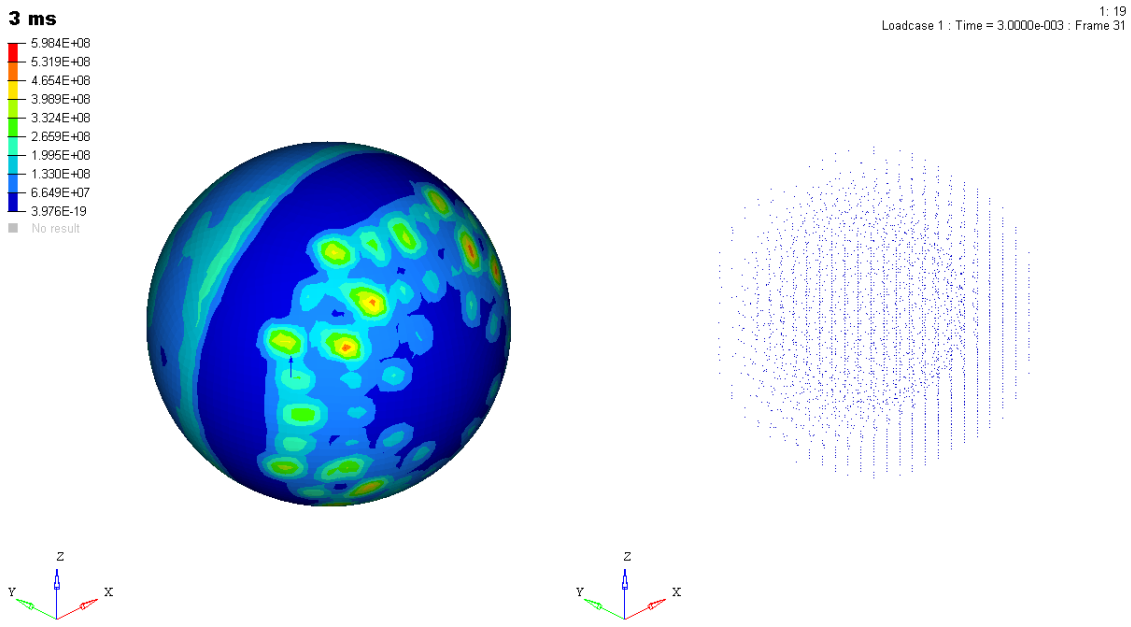

Figure 6.6: RADIOSS Case Study 0. *On the left, contour plot of the sphere at 3 ms. On the right, the representation of the internal gas at the same moment.*

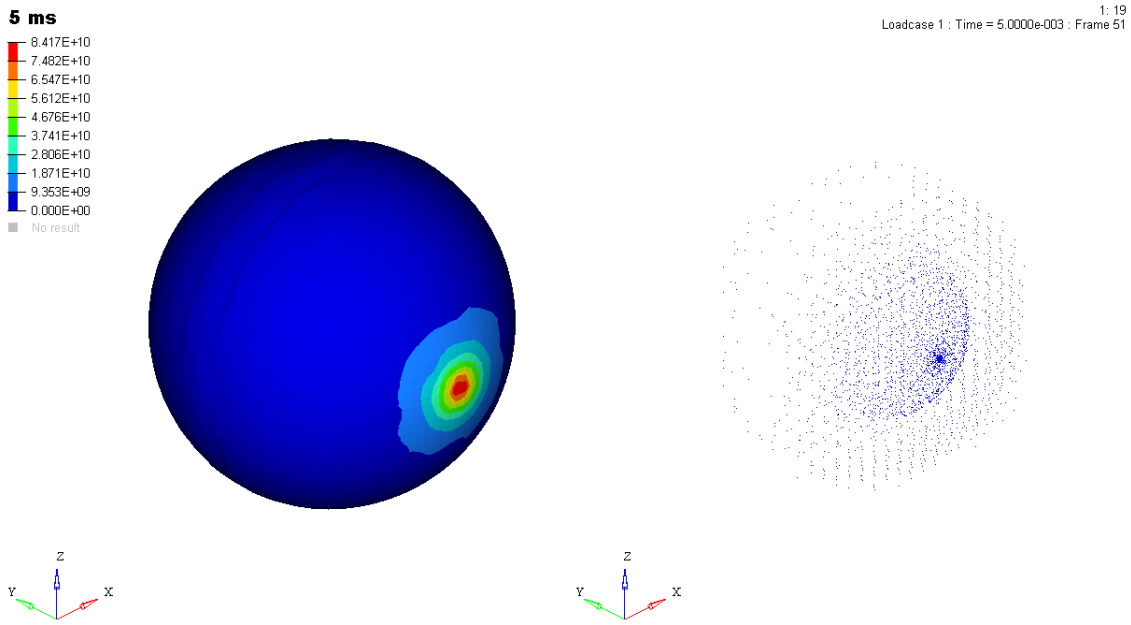

Figure 6.7: *RADIOSS Case Study 0.* On the left, contour plot of the sphere at 5 ms. On the right, the representation of the internal gas at the same moment.

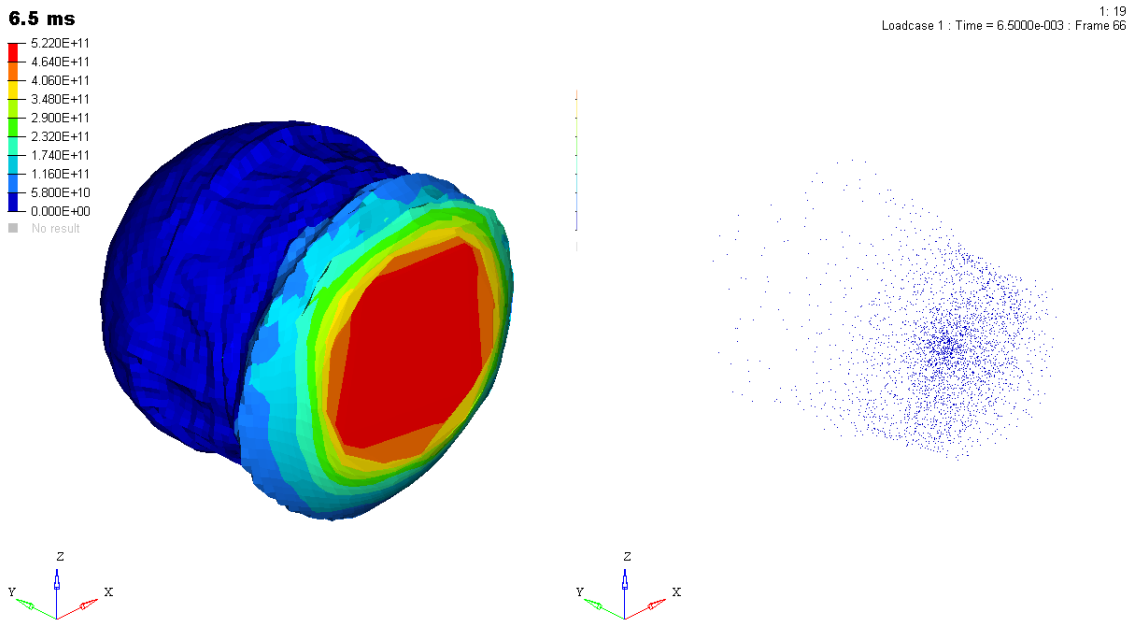

Figure 6.8: *RADIOSS Case Study 0.* On the left, contour plot of the sphere at 6.5 ms. On the right, the representation of the internal gas at the same moment.

At the end, at $t = 6.5\ ms$ the maximum stress is one order of magnitude higher than the yield stress and this brings the sail to failure; in figure 6.8 it is clear that the main reason which causes such failure is gas inertia which keeps pushing on the irradiated face generating that kind of stress.

If we compare this case study with the inertia relief cases made in section 5.3 it is evident that, despite being at a substantially lower acceleration, the stress is much higher. This indicates that probably the cylinder model which should have simulated the presence of gas mass within the sphere in inertia relief model is not conservative but it underestimates the actual stress generated by the gas. The SPH are surely more accurate in simulating gas effects and can also catch turbulent motion and vortices, whose contribution may be the reason which make the two results so different.

So from now on it will be important to understand how to limit the gas effect which seems to be destabilizing.

6.4.2 RADIOSS Case Study 21

The first attempt to improve the strength of the shell is made by increasing Young Modulus (the only difference with respect to the parameters listed in table 6.1 is that Young Modulus $E = 800\ GPa$) , which makes the shell stiffer. It means that the stress needed to obtain a given strain will be higher and so , for a given simulation time, a lower deformation is expected. In fact, it is what happens in the simulation of this case study, which shows a lower deformation and an higher stress for a given simulation time. The evolution of the deformed shape is quite similar to that of RADIOSS Case Study 0 but the sail resists to the breaking which happens for $t = 6.5\ ms$ and undergoes a breaking with a different deformed shape more similar to a disc after 10 ms like showed in figure 6.12.

This behavior indicates that the gas tends to expand also in the peripheral zone after the initial pushing in the polar zone. Anyways, the breaking happens in the maximum stressed zone which is always the polar zone.

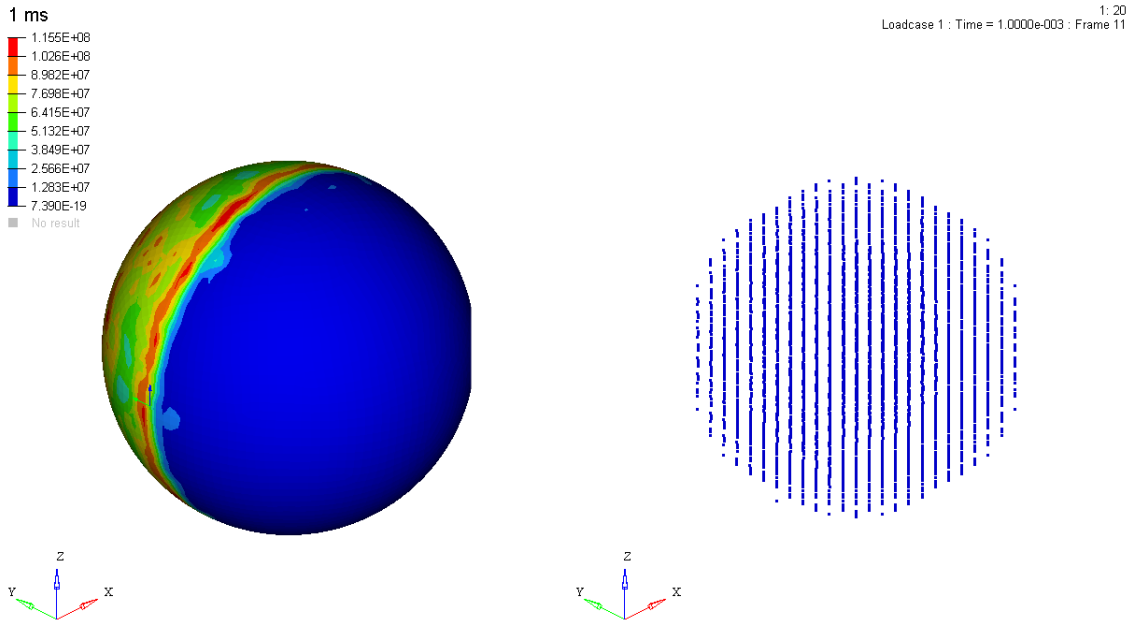

Figure 6.9: RADIOSS Case Study 21. *On the left, contour plot of the sphere at 1 ms. On the right, the representation of the internal gas at the same moment.*

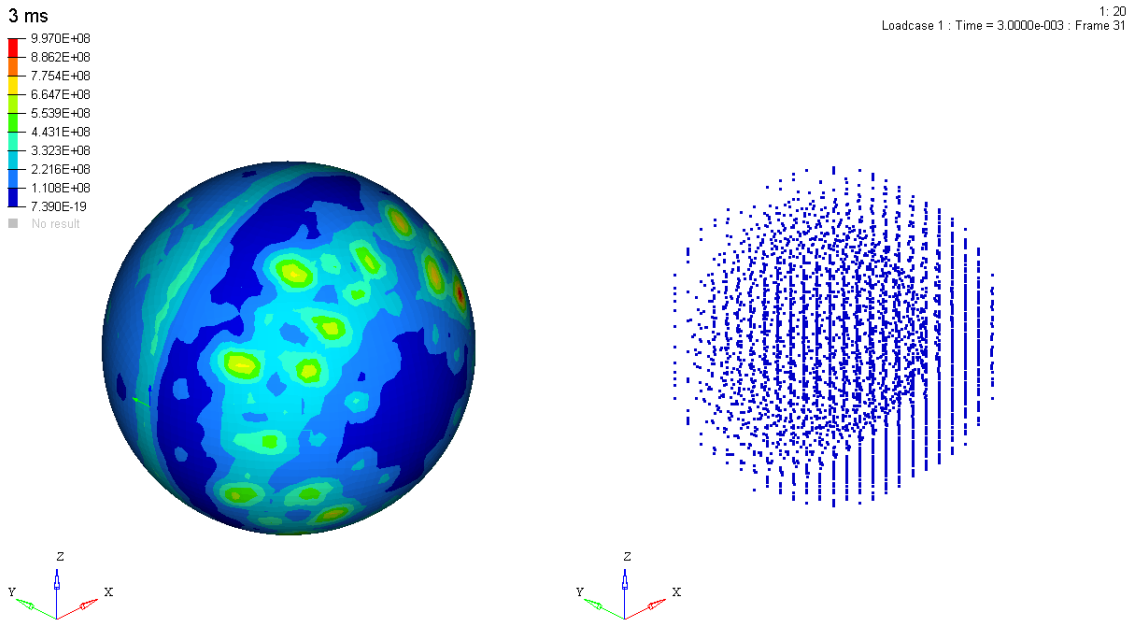

Figure 6.10: RADIOSS Case Study 21. *On the left, contour plot of the sphere at 3 ms. On the right, the representation of the internal gas at the same moment.*

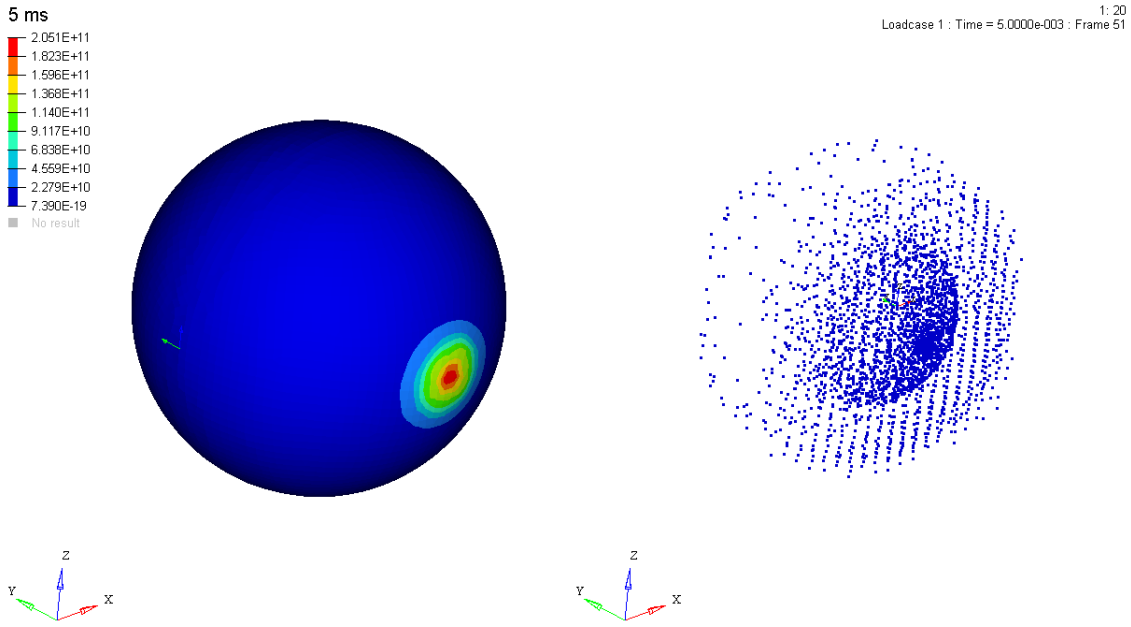

Figure 6.11: *RADIOSS Case Study 21.* On the left, contour plot of the sphere at 5 ms. On the right, the representation of the internal gas at the same moment.

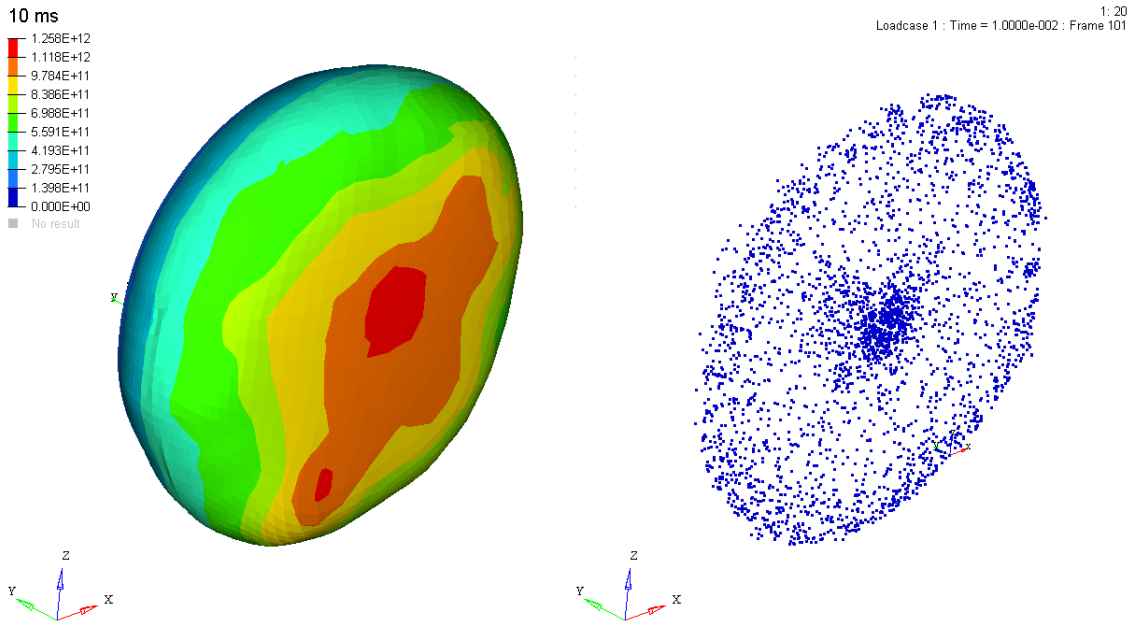

Figure 6.12: *RADIOSS Case Study 21.* On the left, contour plot of the sphere at 6.5 ms. On the right, the representation of the internal gas at the same moment.

6.4.3 RADIOSS Case Study 23

Another way to raise the shell strength is to raise the shell thickness. An expected drawback coming from this change can be an higher stress due to the inertia of the non-irradiated shell. A trade-off among all the parameters must be found with the only aim of reaching a working set-up. For this reason, a configuration like that in table 6.2 is adopted:

	RADIOSS Case Study 23
Young Modulus [GPa]	200
thickness [μm]	0.4
p_{infl} [Pa]	100
m_g [g]	7.3
tollerance	30%
p_{laser} [Pa]	442
E_f [W/m^2]	4.7e+11
$E_{f_{tot}}$ [W]	4.15e+11
Total mass [g]	14.1
acceleration	20000g

Table 6.2: Summary of RADIOSS Case Study 23

From what can be seen in figures 6.13, 6.14, 6.15 and 6.16 actually it seems that the rise of thickness generates a better strength also in the first phase in which the stress in the equatorial zone (figure 6.13) is due mostly to the inertia of non-irradiated semi-spherical shell. This result indicates that the advantage of adopting a much ticker shell (four times ticker than the case described in section 6.4.1) which gives a better strength to the sail prevails on the disadvantage of undergoing a larger inertia.

Also, if compared to the case in which the Young modulus was the quadruple with respect to this case, the max stress for a given simulation time is lower. This means that if the aim is to strengthen the structure of the sail the best choice is to increase the thickness rather than adopting a material with an higher young modulus. The deformation instead follows the case in section 6.4.2 and so it reaches the "disc phase" thanks to its better strength. Of course, higher the thickness of the shell higher the mass of the sail, and so also the requested laser power must

be kept within a certain limit. In this case a power of about $470 GW/m^2$ (a value which respects the project specifications) is necessary to accelerate the sail up to $20000g$.

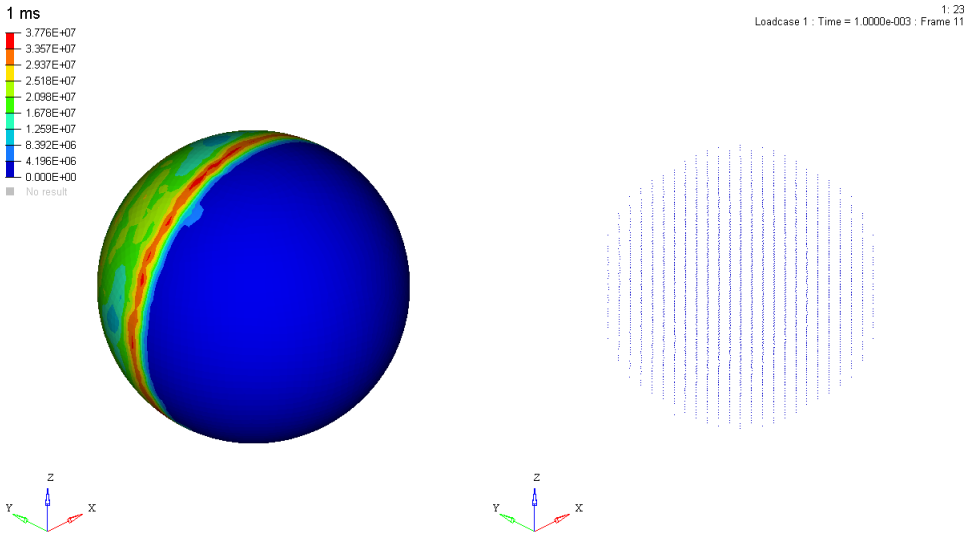

Figure 6.13: RADIOSS Case Study 23. *On the left, contour plot of the sphere at 1 ms. On the right, the representation of the internal gas at the same moment.*

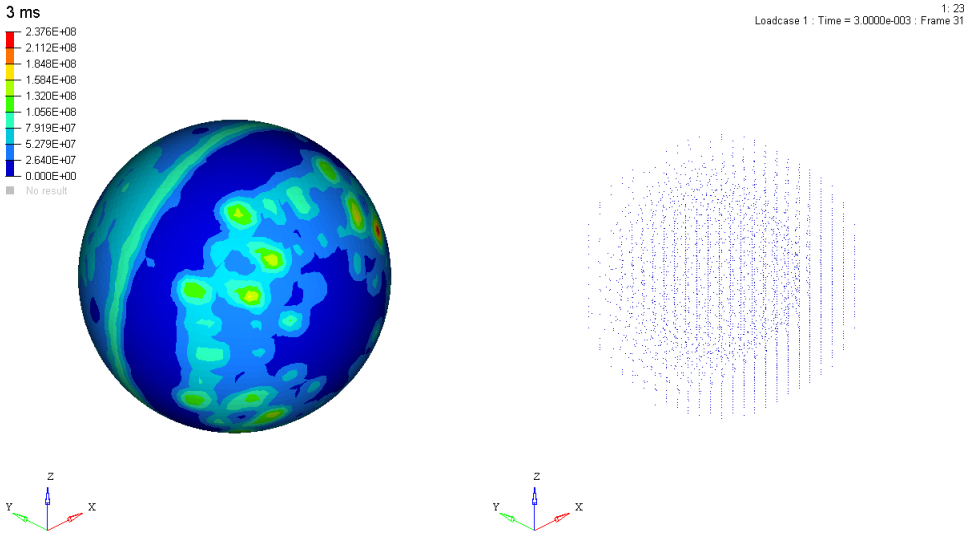

Figure 6.14: RADIOSS Case Study 23. *On the left, contour plot of the sphere at 3 ms. On the right, the representation of the internal gas at the same moment.*

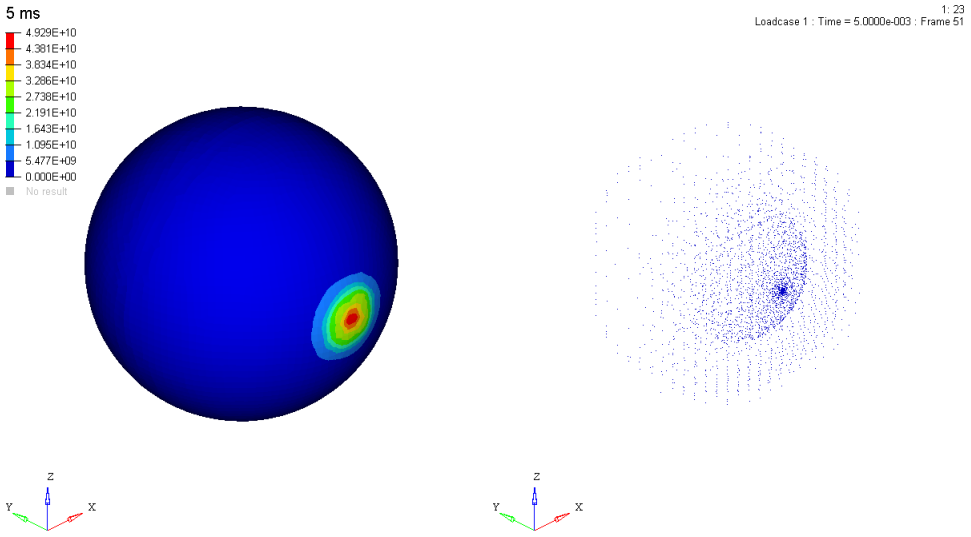

Figure 6.15: RADIOSS Case Study 23. *On the left, contour plot of the sphere at 5 ms. On the right, the representation of the internal gas at the same moment.*

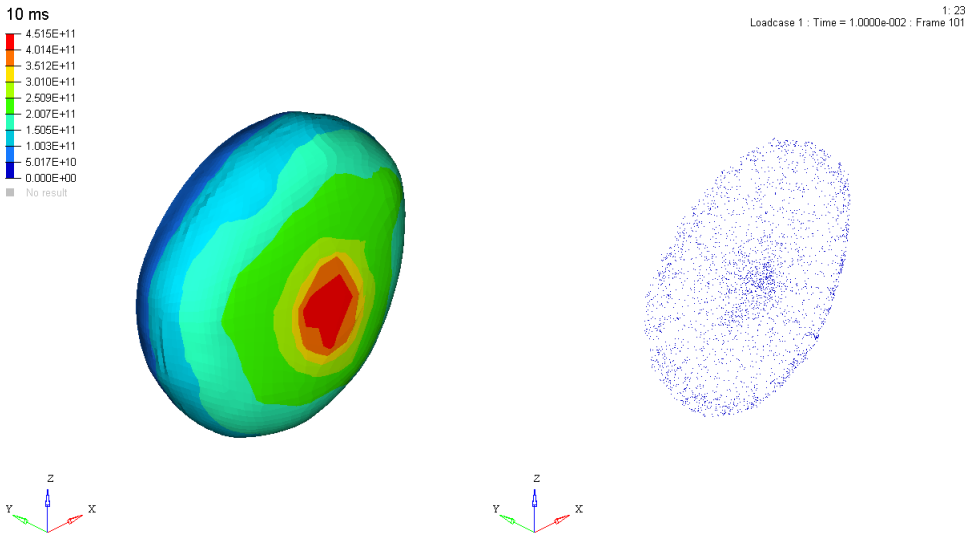

Figure 6.16: RADIOSS Case Study 23. *On the left, contour plot of the sphere at 10 ms. On the right, the representation of the internal gas at the same moment.*

6.4.4 RADIOSS Case Study 27

In this section two variables are modified with respect to RADIOSS Case Study 0: the inflating pressure of the gas (and so also the gas mass) and the thickness. In particular, we have understood that the gas has a destabilizing effect on the physical problem and that if we rise the shell thickness the global stress gets lower.

For this reason, a mixed set-up with the following properties is analyzed:

	RADIOSS Case Study 27
Young Modulus [GPa]	200
thickness [μm]	0.2
p_{infl} [Pa]	1
m_g [g]	0.073
tollerance	30%
p_{laser} [Pa]	112
E_f [W/m^2]	1.05e+11
$E_{f_{tot}}$ [W]	9.28e+10
Total mass [g]	3.5
acceleration	20000g

Table 6.3: Summary of RADIOSS Case Study 27

Lowering the gas mass of two orders of magnitude has several advantages, like reducing the total mass of the sail and so the laser power, reducing the overpressure on the irradiated face and so the global stress level, and so on.

In particular, if we take as reference the simulation time $t = 1\ ms$ and if we compare the maximum stress level with the ones described in sections 6.4.1 and 6.4.3, we can say that in this case the there is respectively a reduction of 473% and 196%. If we take as example the previous simulations we can expect that going ahead in time this gap raises because the massive reduction of gas becomes the controlling variable.

Referring to simulation time $t = 3\ ms$, it is evident that the stress distribution looks quite different with respect to the other two cases, in fact the reduction of gas mass causes a lowered overpressure and so the dominant phenomenon which

generates stress remains the inertia of non-irradiated shell. Quantitatively, the percentage reduction of maximum stress with respect to the ones described in sections 6.4.1 and 6.4.3 is respectively of 1132% and 448%.

For time $t = 5\ ms$ the distribution in the three cases looks the same but with quite different values. This means that in this case the gas becomes the controlling variable later if compared to the previous cases, but eventually the three situations match. The breaking happens in the same zone of the previous cases but without undergoing a massive deformation like was showed in figures 6.8 and 6.16, and undergoing a substantial deformation on the opposite face, probably due to the inertia of the shell.

Even if the sail breaks also in this case, it seems that we are going in the right direction.

The overpressure caused by the gas increases in time because, during the simulation duration (which is of few milliseconds), the phenomenon crosses a transient phase and does not have time to get to the steady state phase in which the pressure should be constant and at the highest value (similar to the one predicted from the cylinder model in previous chapter) because the sail breaks before that point. For this reason, another important step in the same direction can be made to understand if a working configuration can be found.

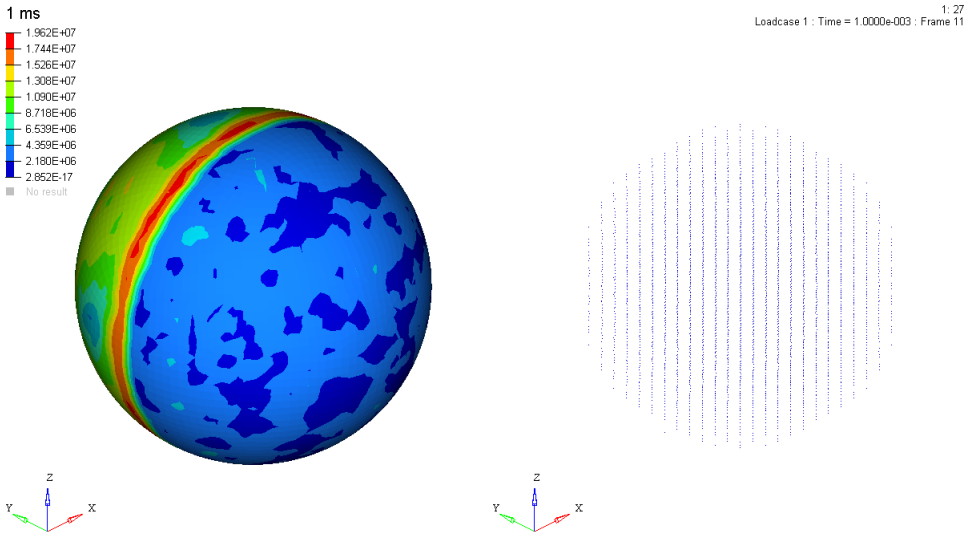

Figure 6.17: RADIOSS Case Study 27. *On the left, contour plot of the sphere at 1 ms. On the right, the representation of the internal gas at the same moment.*

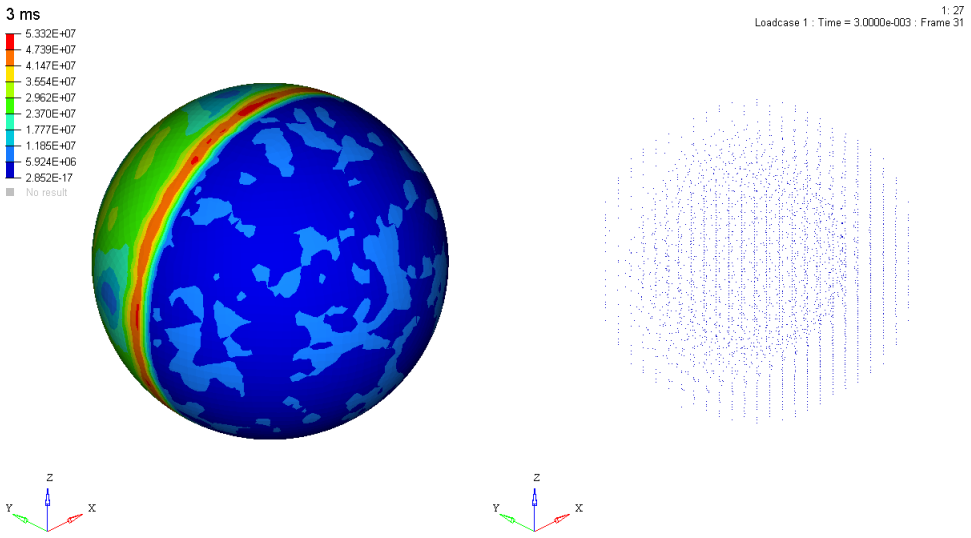

Figure 6.18: RADIOSS Case Study 27. *On the left, contour plot of the sphere at 3 ms. On the right, the representation of the internal gas at the same moment.*

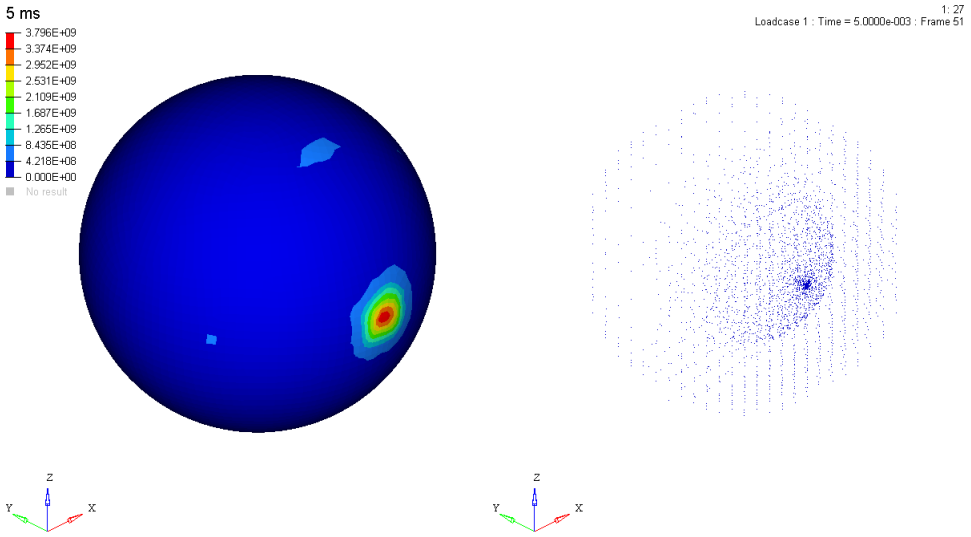

Figure 6.19: RADIOSS Case Study 27. *On the left, contour plot of the sphere at 5 ms. On the right, the representation of the internal gas at the same moment.*

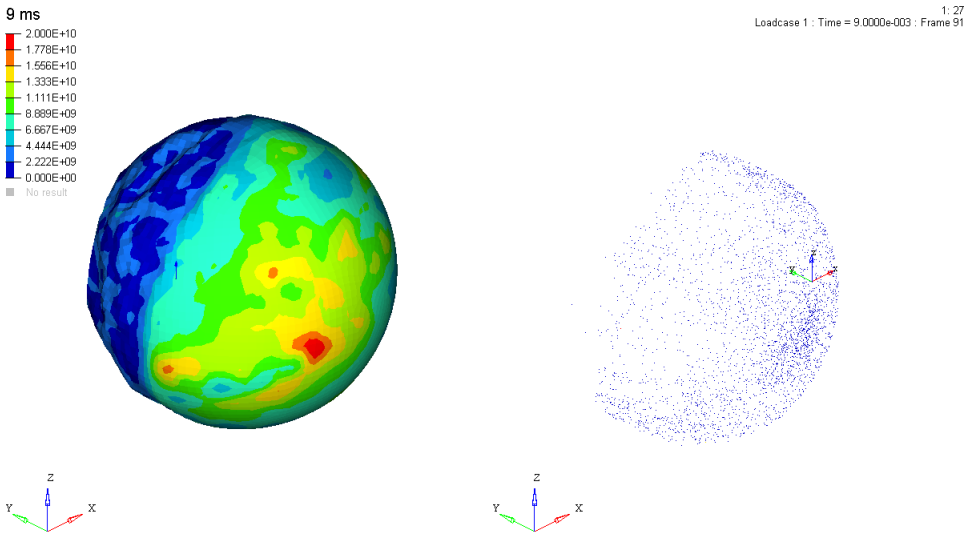

Figure 6.20: RADIOSS Case Study 27. *On the left, contour plot of the sphere at 9 ms. On the right, the representation of the internal gas at the same moment.*

6.4.5 RADIOSS Case Study 29

In this section an exasperation of the last case study is presented: the gas mass is further decreased and the thickness is further increased. The whole data are summarized in the following table:

	RADIOSS Case Study 29
Young Modulus [GPa]	200
thickness [μm]	0.3
p_{infl} [Pa]	0.1
m_g [g]	0.0073
tollerance	30%
p_{laser} [Pa]	165
E_f [W/m^2]	1.75e+11
$E_{f_{tot}}$ [W]	1.55e+11
Total mass [g]	5.1
acceleration	20000g

Table 6.4: Summary of RADIOSS Case Study 29

In this case the further increase of the shell thickness prevails on the further decrease of the gas mass. In fact, the total mass is raised of 145%, and so the laser power. But what really matters is the behavior of the sail with this new set-up.

Let's start analyzing figure 6.21: at time $t = 1\ ms$ the situation is similar to what have been showed in the other case studies, at the same simulation time. In fact the maximum stress is on the equatorial zone and the irradiated face is almost unloaded.

At time $t = 3\ ms$ the distribution is quite different from what we have seen until now at the same simulation time: a certain loading on the irradiated surface is present but the distribution is not uniform and symmetric as expected because of the insufficient mesh density; this problem can't be solved in absence of huge computing power, because otherwise it would require too much time. The simulation gets unstable in time and so the sail undergoes a failure after 5.2 ms; it is worth to underline that although the maximum stress shown in figure 6.24 is far below the yield strength, the one in figure 6.24 is the last frame of simulation in which the sail is intact. The sudden failure which happens in just one tenth of millisecond

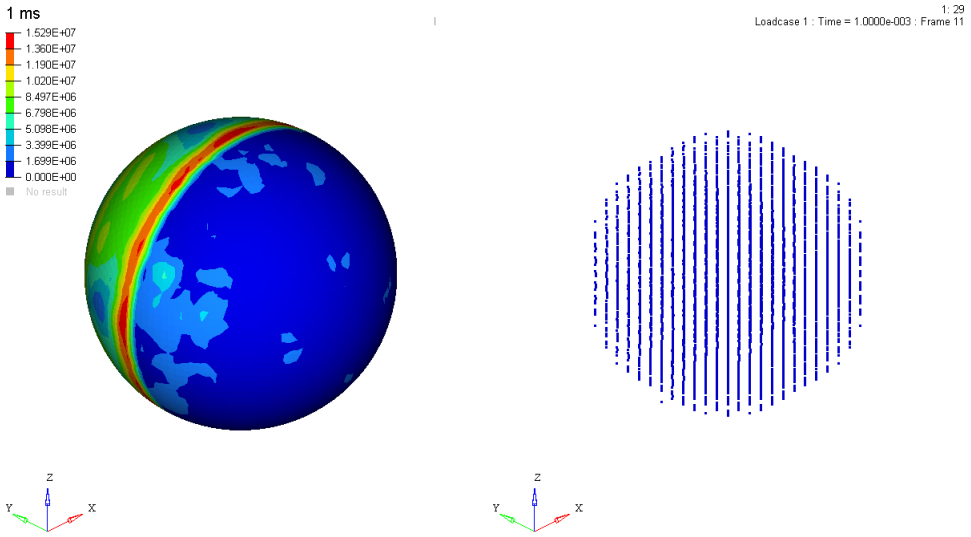

Figure 6.21: RADIOSS Case Study 29. *On the left, contour plot of the sphere at 1 ms. On the right, the representation of the internal gas at the same moment.*

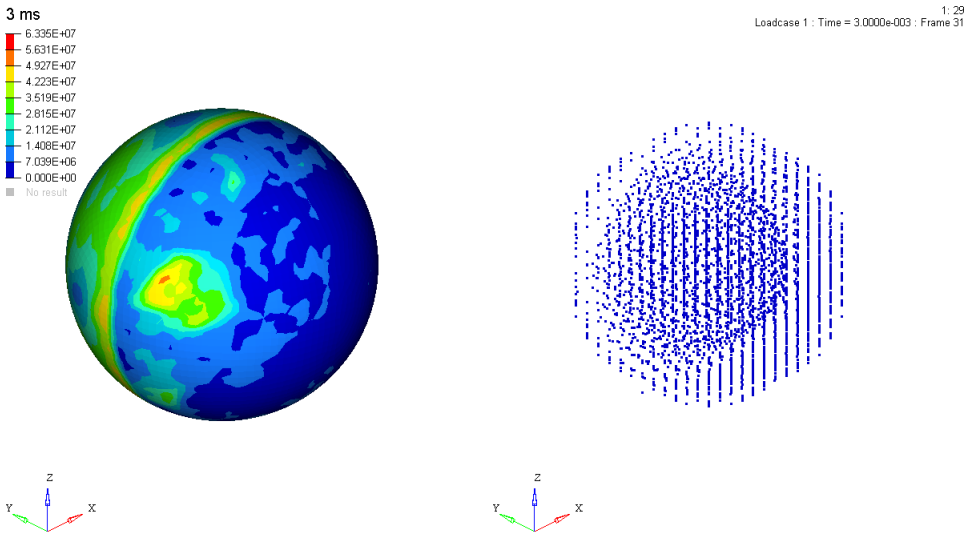

Figure 6.22: RADIOSS Case Study 29. *On the left, contour plot of the sphere at 3 ms. On the right, the representation of the internal gas at the same moment.*

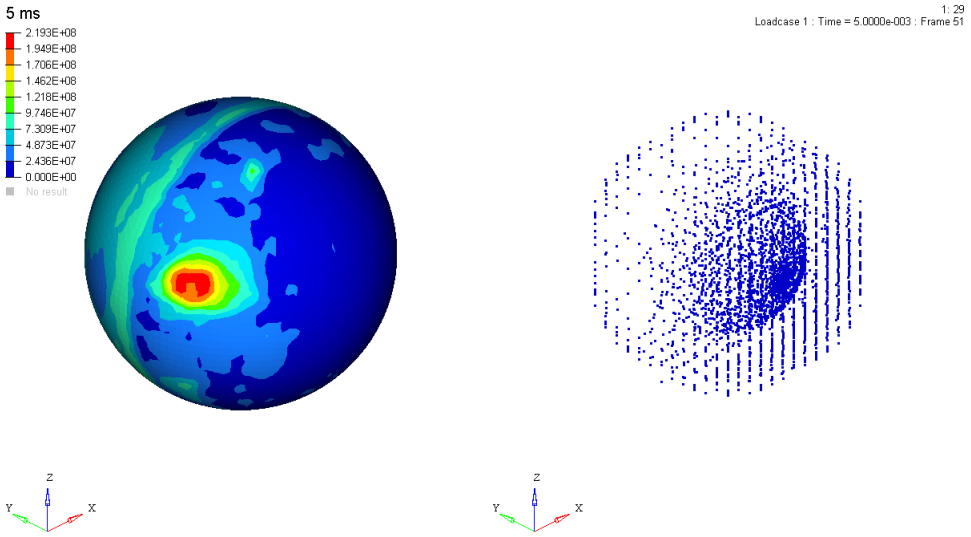

Figure 6.23: RADIOSS Case Study 29. *On the left, contour plot of the sphere at 5 ms. On the right, the representation of the internal gas at the same moment.*

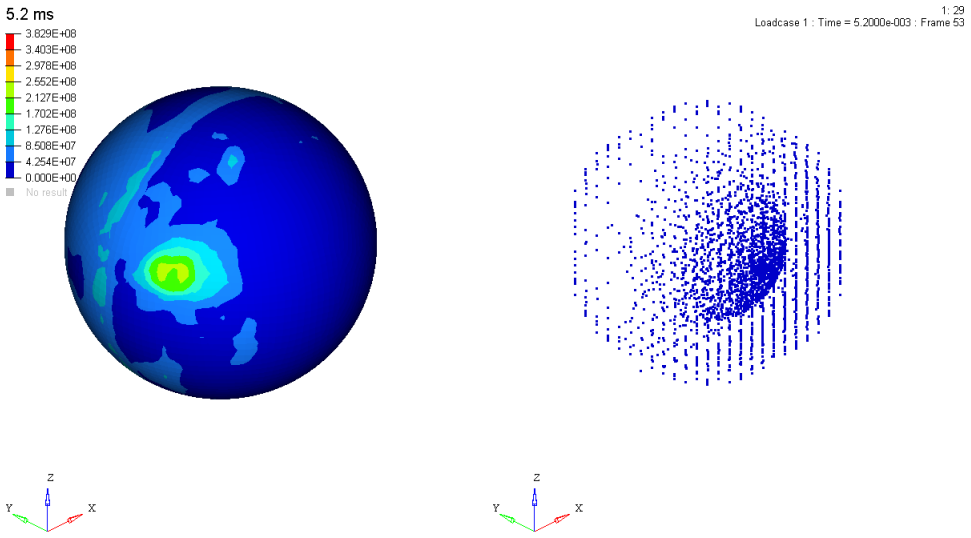

Figure 6.24: RADIOSS Case Study 29. *On the left, contour plot of the sphere at 5.2 ms. On the right, the representation of the internal gas at the same moment.*

(from 5.2 ms to 5.3 ms) is probably due to some numerical issues coming from the inadequacy of both the mesh and SPH density. Anyway, it looks like the controlling variable is still the gas mass which combined with the increased inertia of the shell causes a break.

6.5 Steady state phase - Case Studies and Results

Case studies seen until now show results that were not expected after the inertia relief studies made in previous chapter. In fact, it looks like the sail undergoes different breakings with different set-up, but the most worrying thing is that in each case the sail does not go through the whole transient phase because it breaks before it ends.

A possible reason can be that, due to limited computing time, the transient acceleration phase is modeled with a ramp which brings the sail from 0 to $20000g$ in just 5 ms , and so it is modeled with a ultra-impulsive dynamics which can cause both numerical and physical issues.

Starting from the assumption that the actual transient phase will be far less impulsive and so the sail could go over that phase without undergoing any kind of breaking, a good start to understand something more about the physics of the problem could be simulating the steady-state phase rather than the transient phase.

In particular, the idea is to simulate the last milliseconds of the sail motion which will bring it from a velocity equal to $19.999\% \cdot c$ to the target velocity equal to $20\% \cdot c$.

With a $20000g$ acceleration the time requested to make such a velocity step is 15.3 ms, and so the simulation can be relatively short.

So, with respect to the models seen until now, the simulation has the following set-up:

- *initial velocity* $v_0 = 59957002$ m/s *applied to the whole device (sphere and gas)*;
- *simulation time* $t = 15.3$ ms *: it is the time necessary to increase velocity of a quantity* $\Delta v = v - v_0$ *where* $v = 20\% \cdot c = 59960000$ m/s;

The main problem of these simulations is that a certain degree of approximation can not be removed: in particular, although the whole device is subjected to an initial velocity, the gas at simulation start will be at rest, which is a condition substantially different from the actual one. In fact, at that time of its travel, the gas should be pushed on the irradiated semi-sphere with a certain distribution but of course this cannot be possible without simulating the whole travel (it is not possible to set an initial condition on the gas distribution with this software, but also if it was possible we would have no information on such condition).

This means that this situation is probably not so different from the transient one because it does not remove in an effective way the issues which caused instability, but it is worth a try.

Remarking the assumption that the actual steady-state phase cannot be simulated, only few cases will be addressed in the following subsections, that are a case in which the Young modulus is increased up to 800 GPa , a case in which the thickness of the shell is brought to 0.4 μm and a case in which the gas mass is reduced (we have already seen that increasing the gas mass amplifies all the inertial issues whereas reducing it the stress becomes substantially smaller).

The complete set up of the following Case Studies (namely Case Studies 41, 43 and 45) is the same of the respective Case Studies 21, 23 and 25; the only difference is that in the new case studies the aim is to study an approximated steady-state phase rather than a transient phase.

6.5.1 RADIOSS Case Study 41

In this case study the model has the same set-up of the model presented in section 6.4.2 (so the only variation with respect to RADIOSS Case Study 0 is the Young Modulus increased up to 800 GPa), but it investigates a steady-state phase rather than a transient phase.

In figures 6.25, 6.26, 6.27 and 6.28 the evolution of the sail in time is showed as usual. What can be immediately noticed is that in this case the deformation is visible earlier than in the previous cases (transient phase). Probably this happens because of the initial velocity which contributes to make the phenomenon happen much faster.

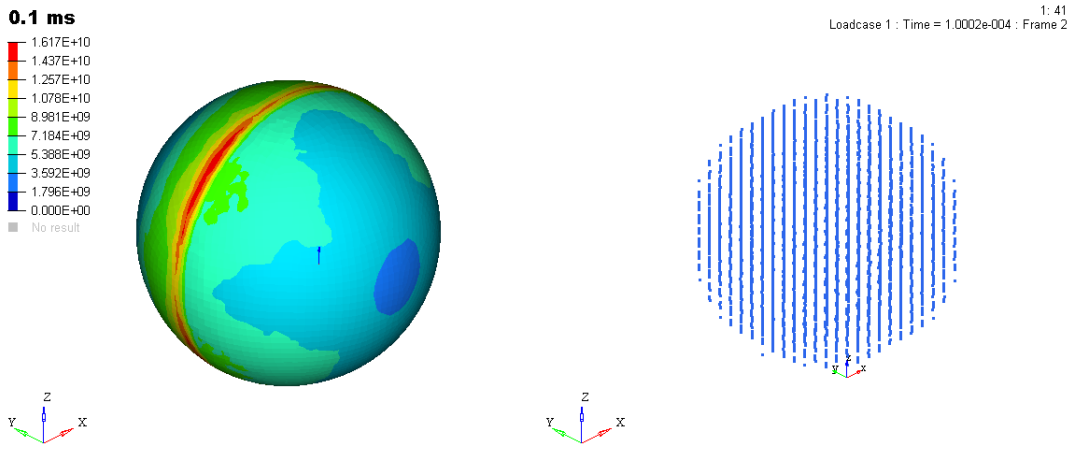

Figure 6.25: RADIOSS Case Study 41. *On the left, contour plot of the sphere at 0.1 ms. On the right, the representation of the internal gas at the same moment.*

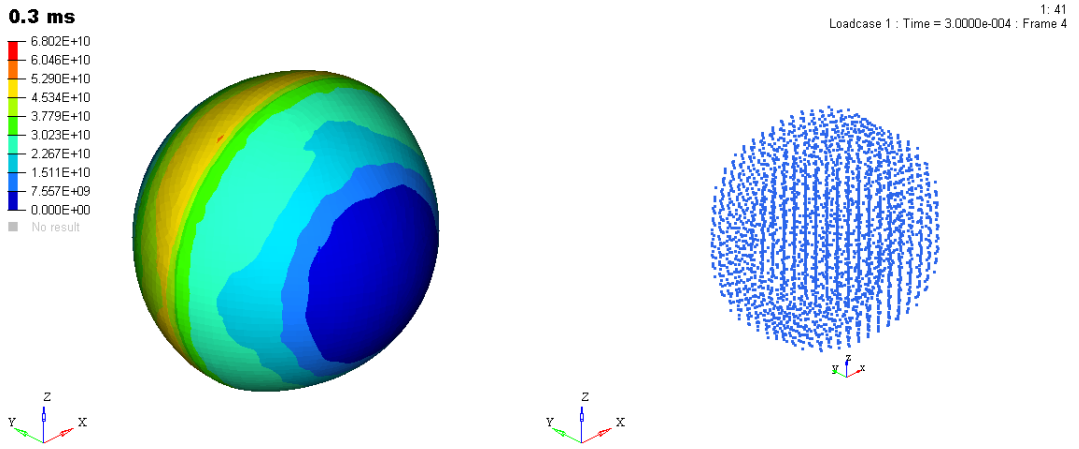

Figure 6.26: RADIOSS Case Study 41. *On the left, contour plot of the sphere at 0.3 ms. On the right, the representation of the internal gas at the same moment.*

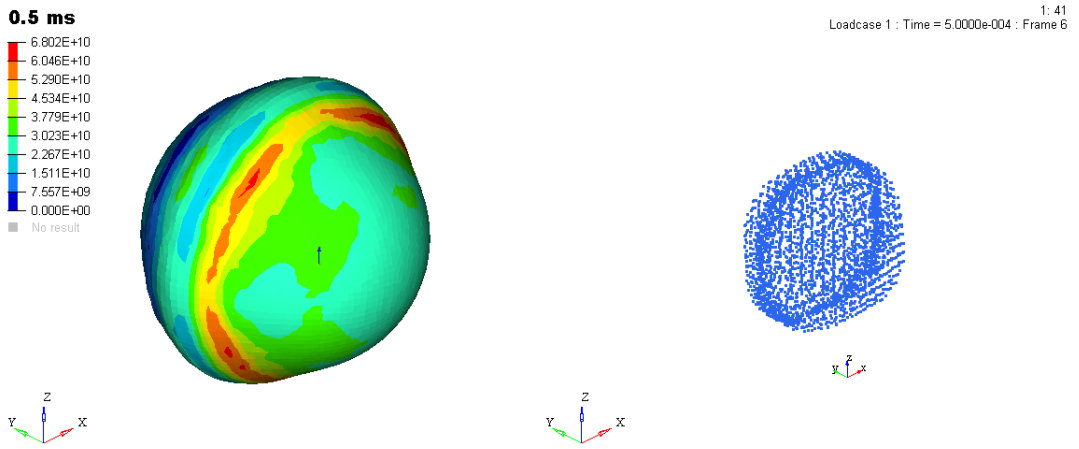

Figure 6.27: RADIOSS Case Study 41. *On the left, contour plot of the sphere at 0.5 ms. On the right, the representation of the internal gas at the same moment.*

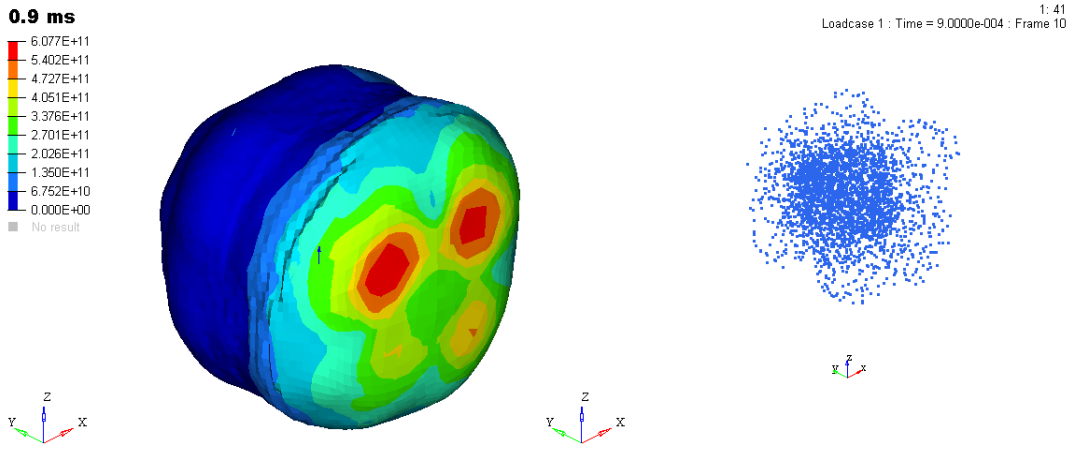

Figure 6.28: RADIOSS Case Study 41. *On the left, contour plot of the sphere at 0.9 ms. On the right, the representation of the internal gas at the same moment.*

For this reason, the max stress goes beyond yield stress almost immediately (after 0.1 ms) as showed in figure 6.25. The following figures show a deformation which is not the actual one (because the material has been modeled as an elastic isotropic material, and so the solver does not have informations about the plastic zone of the $\sigma - \epsilon$ curve) and which shows a consistent increase in stress because of the linear behavior adopted also beyond the yield strength. So they are shown as an additional information but must be analyzed critically.

6.5.2 RADIOSS Case Study 43

The model discussed in this Case study has the same properties shown in table 6.2, but different initial conditions on the velocity as already specified in introduction of section 6.5.

A behavior similar to that shown in section 6.5.1 is expected, with a slightly retarded pattern due to its better resistance given by the thickness increase.

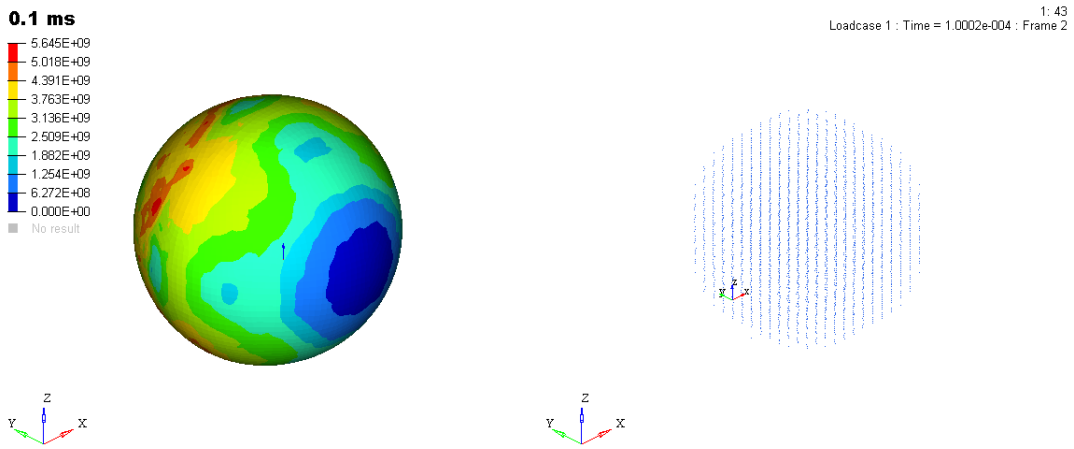

Figure 6.29: RADIOSS Case Study 43. *On the left, contour plot of the sphere at 0.1 ms. On the right, the representation of the internal gas at the same moment.*

In fact, looking at figure 6.29 what happens is that for $t = 0.1$ ms the stress developed is below the yield stress and the maximum stresses are located on the face opposite to the irradiated one, probably due to the fact that at this point the inertia of the shell is still the controlling factor.

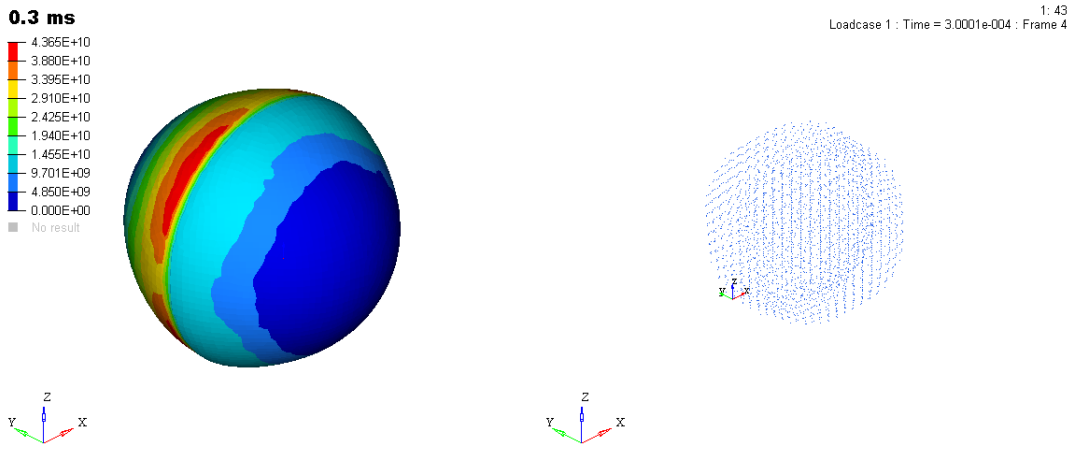

Figure 6.30: RADIOSS Case Study 43. *On the left, contour plot of the sphere at 0.3 ms. On the right, the representation of the internal gas at the same moment.*

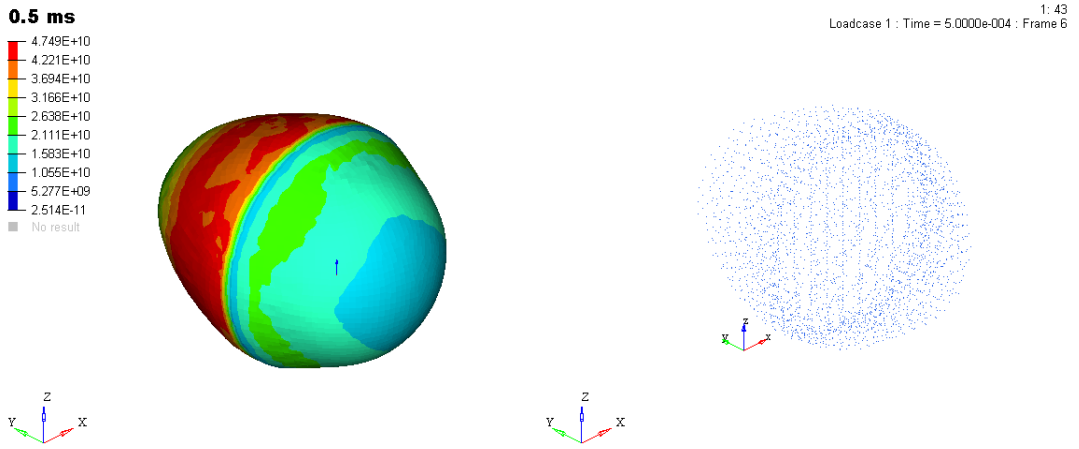

Figure 6.31: RADIOSS Case Study 43. *On the left, contour plot of the sphere at 0.5 ms. On the right, the representation of the internal gas at the same moment.*

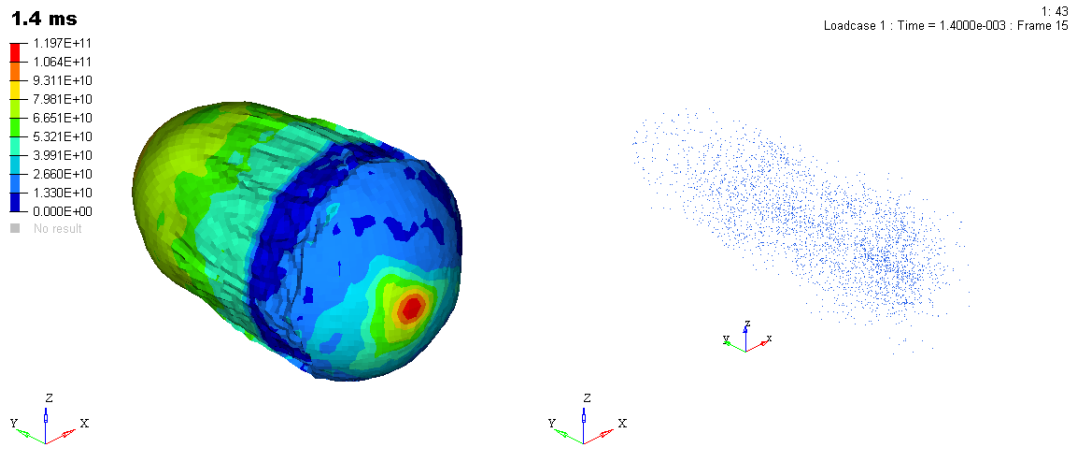

Figure 6.32: RADIOSS Case Study 43. *On the left, contour plot of the sphere at 1.4 ms. On the right, the representation of the internal gas at the same moment.*

However the situation is not substantially better than what was shown in section 6.5.1 because yield stress is passed after only 0.3 ms.

Remembering the low reliability of the deformed shape for stress values that exceed the yield stress, it is possible to notice a different breaking mode in this case. In fact, due to inertia of the gas and thanks to the better structural strength of the shell the sail tends to become oval before the breaking which is caused by the gas that keeps pushing on the irradiated surface from the inside.

Such breaking happens obviously later than the previous case, and the gas has the possibility to acquire a longitudinal distribution along the motion axis (y).

6.5.3 RADIOSS Case Study 49

Case 49 is the same as Case 29 but in steady state condition. Also this case shows a deformed shape similar to other case studies of this section but thanks to the combination of higher thickness and lower gas mass the breaking happens later (for $t = 3.5ms$) than previous cases.

6.6 Lower Accelerations - Reducing inertial effects

All the studies in this chapter have been made by taking as reference an acceleration of $20000g$, which would get our sail to the target velocity in about 5 minutes.

From the last studies it looks like a configuration like that does not get us anywhere; in particular, being the gas inertial effects the most important reason of breaking, and after having verified that also a massive reduction of the internal gas is not enough, reducing the acceleration seems like the quickest solution to reduce the inertial effects which our sail is not able to handle.

It is also true that lower accelerations means higher propulsion time and higher distances to reach with laser before the sail velocity reaches the target value, so also the acceleration has a limit under which the mission cannot be accomplished.

Such limits are not well known, so three cases are investigated:

- ***RADIOSS Case Study 30*** **-** in which the target acceleration is set to $10000g$;
- ***RADIOSS Case Study 31*** **-** in which the target acceleration is set to $5000g$;
- ***RADIOSS Case Study 32*** **-** in which the target acceleration is set to $1000g$;

In table 6.5 some interesting data about these case studies are summarized.

	Case Study 30	**Case Study 31**	**Case Study 32**
acceleration [g]	10000	5000	1000
propulsion time [min]	10	20	102
final distance [km]	1.83e+07	3.7e+07	1.83e+08
final distance [UA]	0.1222	0.2443	1.2216

Table 6.5: Summary of some interesting parameters regarding RADIOSS Case Studies 30, 31 and 32

In the interests of brevity, only the most significant case will be showed. In particular, the one that shows the best improvements with respect to the previous

ones is of course the case study 32, which presents the lowest acceleration. In fact case study 30 and 31 does not reach significant results, also if the sail breaks later.

Reducing instead the acceleration of one order of magnitude has a similar effect on the stress level, and this allows the sail to have a better durability.

Although not sufficient for our aim (because the propulsion time is too long), $1000g$ is still a quite large acceleration, and so it is not clear if the shell will be able to resist to the whole transient phase or it will simply break later.

A detailed analysis of this case is represented in figures 6.33, 6.34, 6.35 and 6.36.

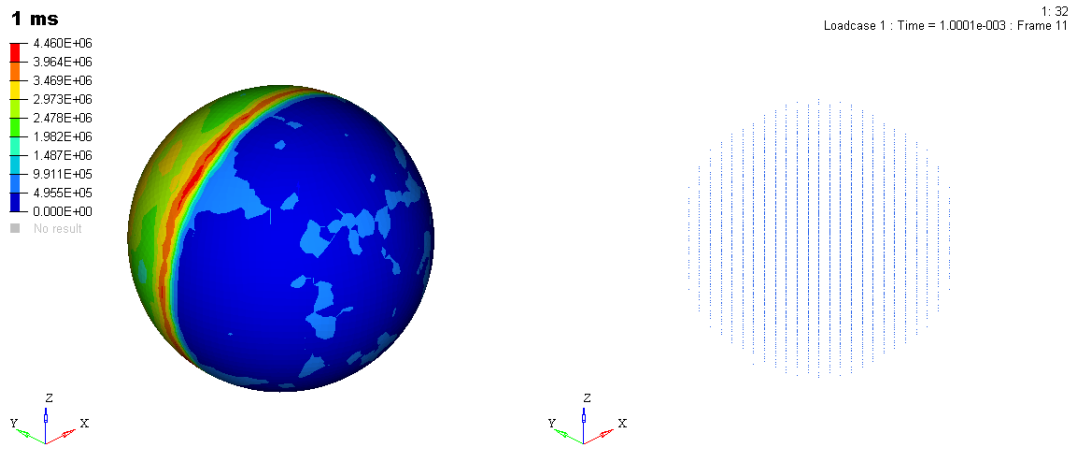

Figure 6.33: RADIOSS Case Study 32. *On the left, contour plot of the sphere at 1 ms. On the right, the representation of the internal gas at the same moment.*

After 1 ms, the global stress level is four orders of magnitude smaller than yield stress, and so there are no problems for the shell.

Also after 5 ms the stress level is far below the yield stress, but the distribution looks quite similar to the one already seen in previous cases, and this looks correct because the motion of the gas should not change with the acceleration.

The sail is able to reach also 10 ms of simulation without undergoing too much stress, remaining below the yield stress of two orders of magnitude.

In the end, at 15 ms it is shown that a very restricted area where the gas has the highest density (visible in figure 6.36) undergoes a stress very close to the yield stress, and so in the next few milliseconds the sail will break with a breaking mode similar to what was seen in previous cases.

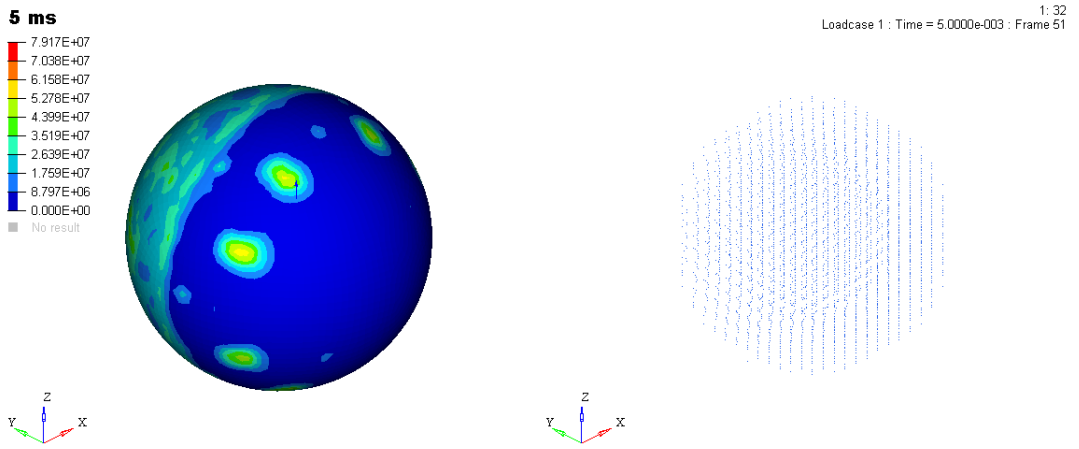

Figure 6.34: RADIOSS Case Study 32. *On the left, contour plot of the sphere at 5 ms. On the right, the representation of the internal gas at the same moment.*

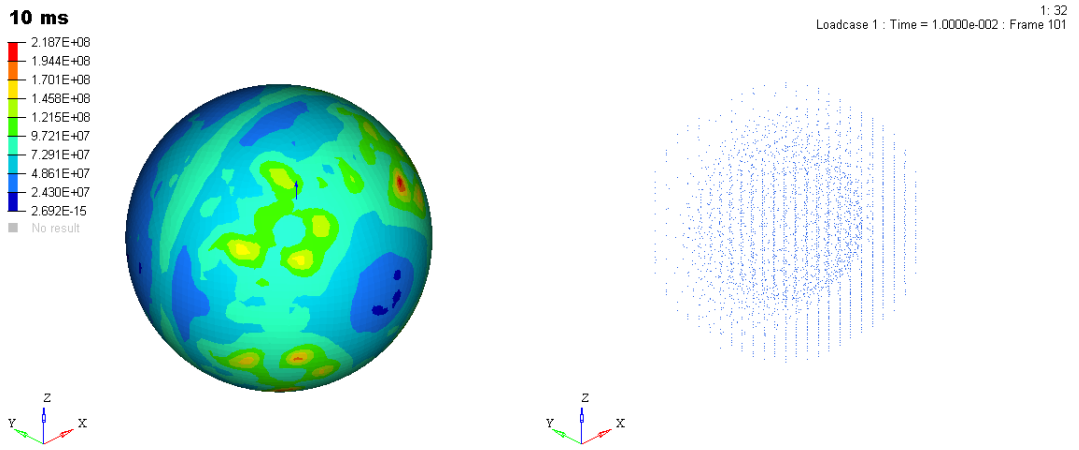

Figure 6.35: RADIOSS Case Study 32. *On the left, contour plot of the sphere at 10 ms. On the right, the representation of the internal gas at the same moment.*

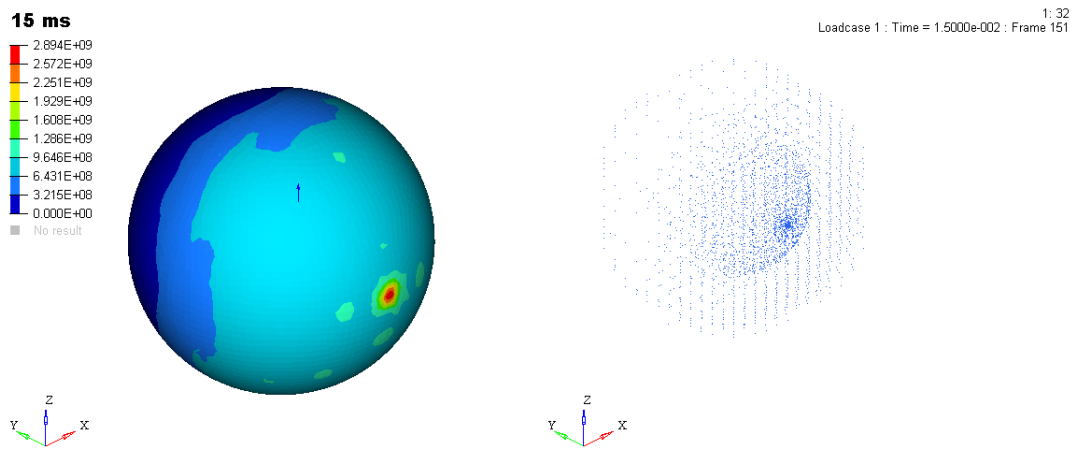

Figure 6.36: RADIOSS Case Study 32. *On the left, contour plot of the sphere at 15 ms. On the right, the representation of the internal gas at the same moment.*

So, not even this configuration allows the sail to reach the target velocity without breaking. Comparing all the cases seen until now, it seems that the stress peaks are due to the presence of gas which exerts an overpressure on the irradiated surface and creates a general instability during the motion.

The most natural solution to this problem is of course thinking of developing a model in which the gas is not present at all, also if this was indicated as a project specification. If a configuration of this kind proves to work without particular issues, a new design solution must be presented in order to replace the gas mass.

6.7 No-gas configuration

All the configurations seen until now don't allow either to go beyond the transient phase or to resist at the steady state phase, and this is probably due to the inertial effect of the gas which creates instability at ultra-high accelerations.

So in this section some solutions with no gas within the spherical shell will be investigated. The assumption is that a different way to unfold the sail is found, and this will be treated later.

6.7.1 RADIOSS Case Study 0-NG

The removal of gas from the problem simplifies things a lot. In order to make some useful comparison it is necessary to set a new reference case, which is on the same line of the one in section 6.7.1 but has no gas. The new set-up is summarized in table 6.6.

	RADIOSS Case Study 0-NG
Young Modulus [GPa]	200
thickness [μm]	0.1
p_{infl} [Pa]	0
m_g [g]	0
tollerance	30%
p_{laser} [Pa]	54.5
E_f [W/m^2]	5.8e+10
$E_{f_{tot}}$ [W]	5.12e+10
Total mass [g]	1.7
acceleration	20000g

Table 6.6: Summary of RADIOSS Case Study 0 - NG

There are few substantial advantages in removing the gas, like lower mass and so lower laser power requested; a lower stress level in general is expected.

A set of four figures relative to four different time frames is now presented (figures 6.37, 6.38, 6.39 and 6.40).

Looking at the four figures, the first thing to do is to make a comparison with respect to the RADIOSS Case Study 0 which still has the gas mass.

From a comparison between figures 6.37 and 6.5 we can note both a different stress distribution and a maximum stress higher of 456% in the latter case. Since the gas was removed due to its destabilizing effect, this result could be considered weird at first impact. But remembering that figures 6.37 and 6.5 are referred to a frame at 1 ms, some considerations can be made in order to justify such behavior:

- at that time the gas is almost in the initial position and so the pressure and density fields can be considered uniform;
- no overpressure on the irradiated face means no additional stress;

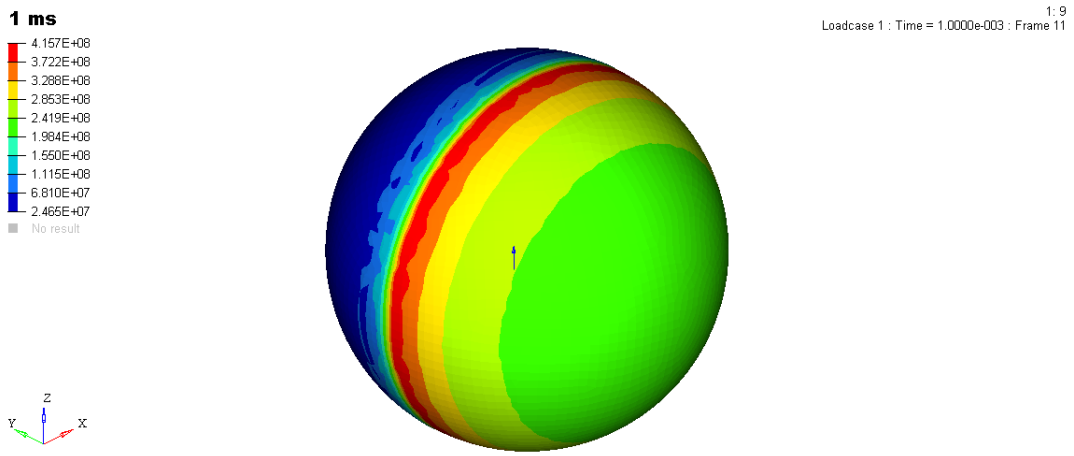

Figure 6.37: RADIOSS Case Study 0-NG. *On the left, contour plot of the sphere at 1 ms. On the right, the representation of the internal gas at the same moment.*

- at that time the stress is almost completely caused by the inertia of the shell and in that moment the distribution of the gas (which exerts a certain pressure also on the non-irradiated face) can be considered stabilizing, because it is opposite to the inertia force of the shell.

Actually, the stress level on the non-irradiated face is not so different in the two cases, and this can be seen looking carefully at the scales. What is completely different is the distribution on the irradiated face that with the presence of gas is almost unloaded whereas without the gas shows the peak of stress. This could be caused by the absence of the gas that when is present, in the initial phases in which it still does not exerts any overpressure, probably plays a role in counteracting the external laser pressure.

From the comparison at $t = 3\ ms$ (between figure 6.6 and 6.38), what happens is that the sail is deformed by the beginning of collapse of the non irradiated face due to its own inertia and such deformation is accentuated by the absence of gas which normally takes position against this phenomenon.

Going ahead in time and keeping an eye on the comparison between RADIOSS Case Study 0 and 0-NG, the fundamental difference comes out. In fact, in case 0-NG the maximum stress seems to tend to a certain asymptote although it goes beyond yield stress and so the sail breaks anyway. What is more, the maximum

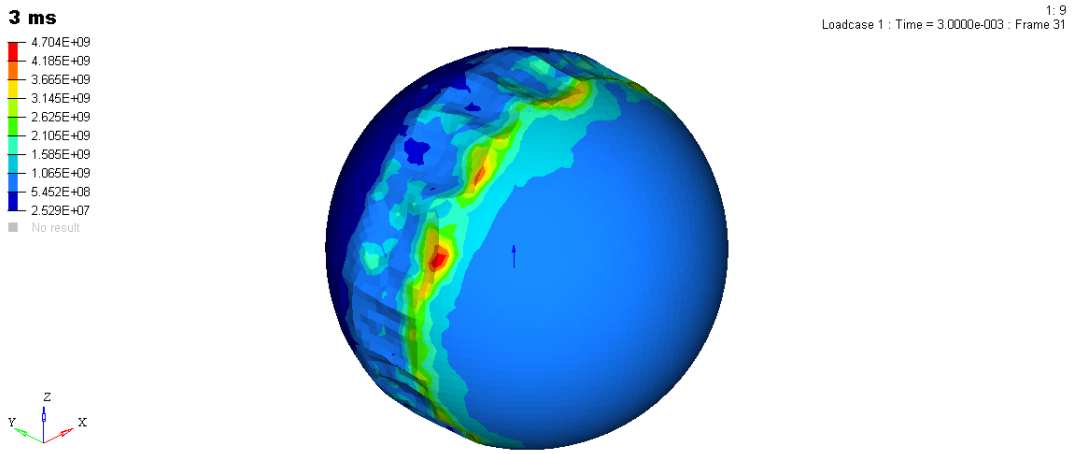

Figure 6.38: RADIOSS Case Study 0-NG. *On the left, contour plot of the sphere at 3 ms. On the right, the representation of the internal gas at the same moment.*

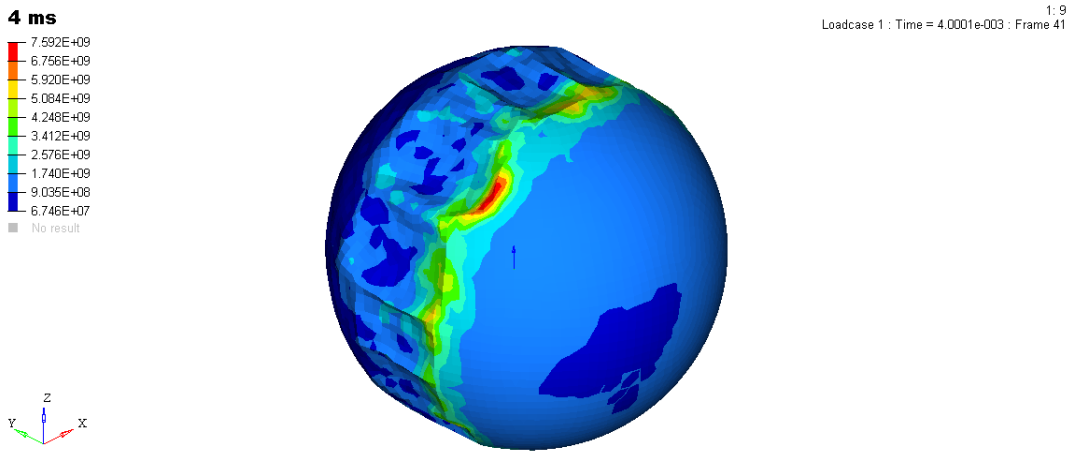

Figure 6.39: RADIOSS Case Study 0-NG. *On the left, contour plot of the sphere at 4 ms. On the right, the representation of the internal gas at the same moment.*

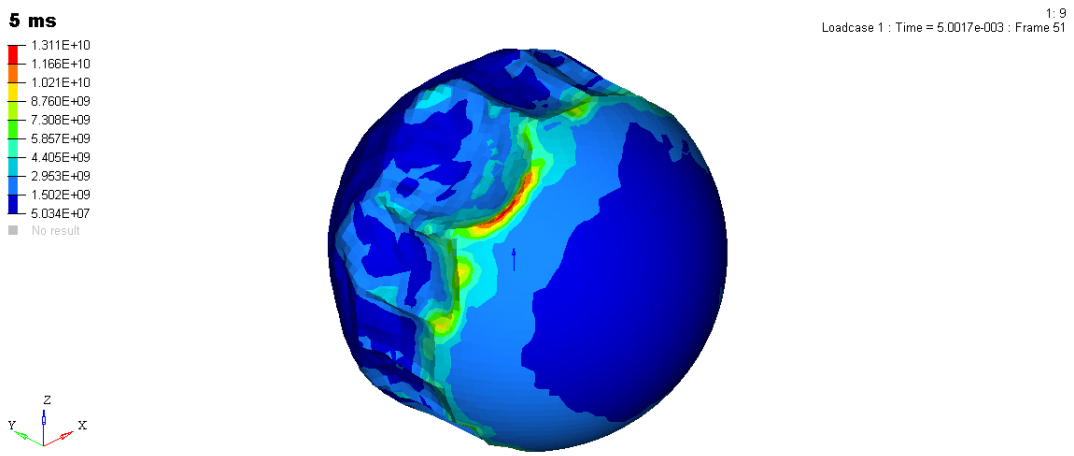

Figure 6.40: RADIOSS Case Study 0-NG. *On the left, contour plot of the sphere at 5 ms. On the right, the representation of the internal gas at the same moment.*

stress is relegated to the same zone (equatorial zone) in all following time steps while in case 0 the stress starts growing in uncontrolled way and reaches a maximum in a zone close to the pole of the irradiated face.

Also if this set-up doesn't solve the problem, the behavior seems to be more controlled and less impulsive. In order to find a working configuration other three cases are analyzed.

6.7.2 RADIOSS Case Study 11-NG

This Case Study presents the following set-up:

in which the only difference with respect to the reference case in section 6.7.1 is the Young modulus increased of four times, up to 800 GPa.

What can be said about the comparison with the reference case "RADIOSS Case Study 0 - NG" is that for a given time step the stress developed within the shell are approximatively the same but the shell undergoes a lower deformation. After 5 *ms* the stress level is almost at yield stress level, and it goes beyond that limit just few instants later. So, increasing the elastic modulus does not help in terms of maximum stress developed but it helps in term of deformations, for this case in which the stress level remains about the same.

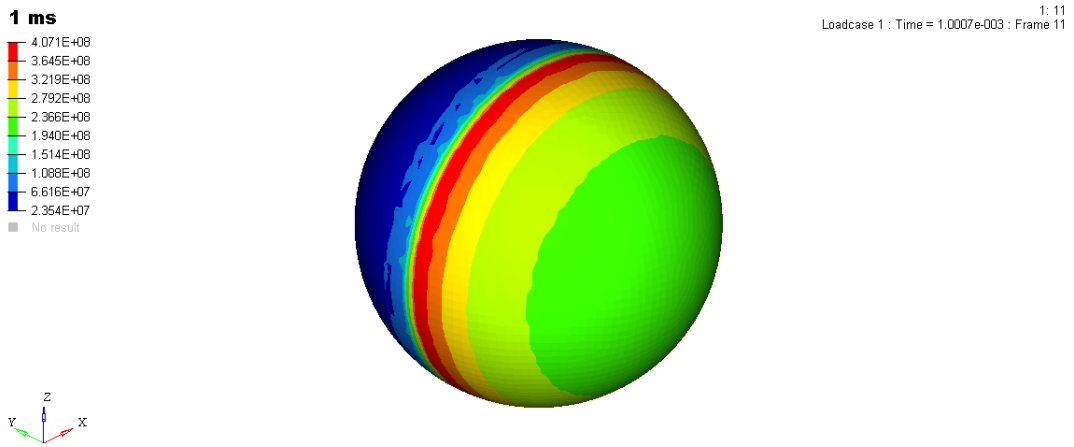

Figure 6.41: RADIOSS Case Study 11-NG. *On the left, contour plot of the sphere at 1 ms. On the right, the representation of the internal gas at the same moment.*

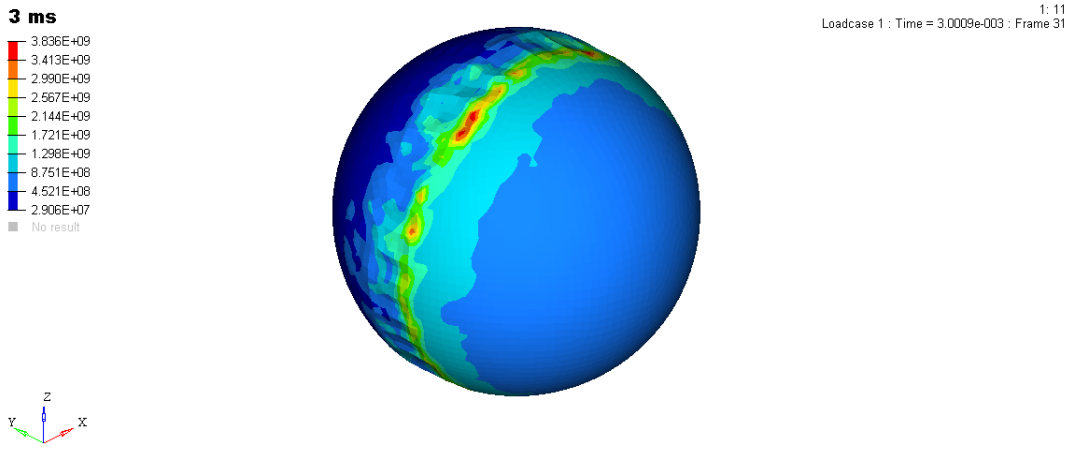

Figure 6.42: RADIOSS Case Study 11-NG. *On the left, contour plot of the sphere at 3 ms. On the right, the representation of the internal gas at the same moment.*

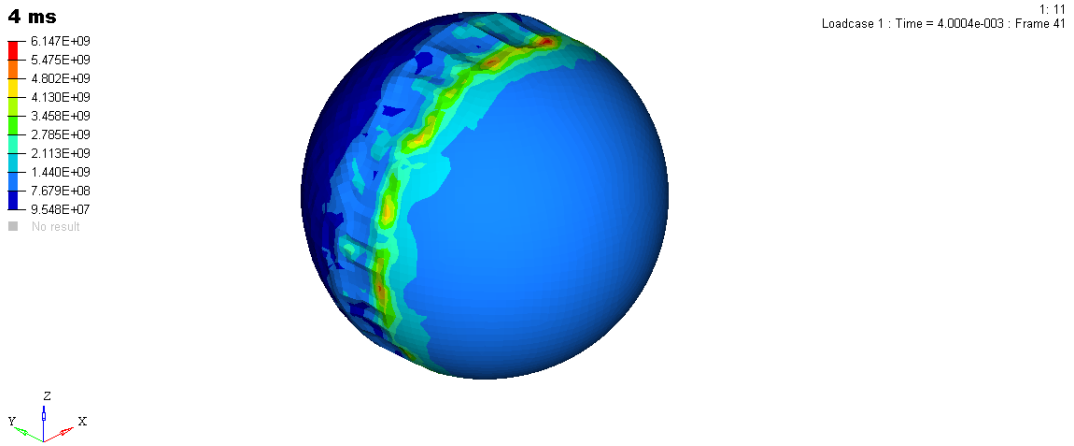

Figure 6.43: RADIOSS Case Study 11-NG. *On the left, contour plot of the sphere at 4 ms. On the right, the representation of the internal gas at the same moment.*

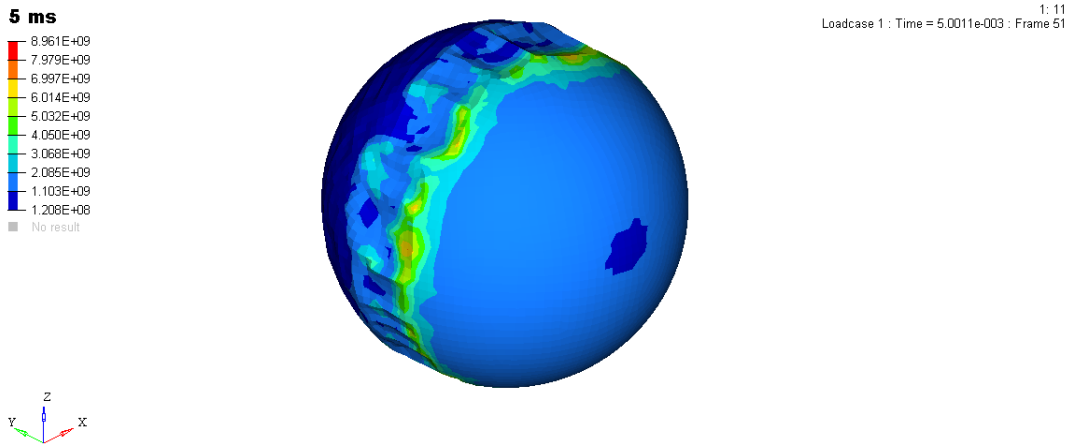

Figure 6.44: RADIOSS Case Study 11-NG. *On the left, contour plot of the sphere at 5 ms. On the right, the representation of the internal gas at the same moment.*

	RADIOSS Case Study 11-NG
Young Modulus [GPa]	800
thickness [μm]	0.1
p_{infl} [Pa]	0
m_g [g]	0
tollerance	30%
p_{laser} [Pa]	54.5
E_f [W/m^2]	5.8e+10
$E_{f_{tot}}$ [W]	5.12e+10
Total mass [g]	1.7
acceleration	20000g

Table 6.7: Summary of RADIOSS Case Study 11 - NG

6.7.3 RADIOSS Case Study 12-NG

This Case Study presents the following set-up:

	RADIOSS Case Study 12-NG
Young Modulus [GPa]	200
thickness [μm]	0.2
p_{infl} [Pa]	0
m_g [g]	0
tollerance	30%
p_{laser} [Pa]	108
E_f [W/m^2]	1.15e+11
$E_{f_{tot}}$ [W]	1.01e+11
Total mass [g]	3.4
acceleration	20000g

Table 6.8: Summary of RADIOSS Case Study 12 - NG

In this case, only the thickness is doubled with respect to the reference case. The thickness increment causes also increasing mass and so increasing laser power.

An higher thickness should make things better in terms of strength and overall resistance.

The results of this simulations are shown in figures 6.45, 6.46, 6.47 and 6.48.

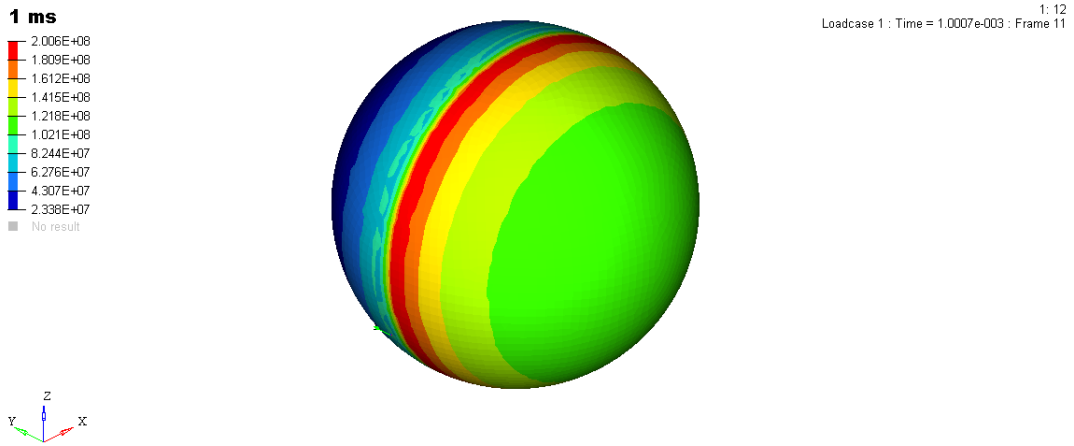

Figure 6.45: RADIOSS Case Study 12-NG. *On the left, contour plot of the sphere at 1 ms. On the right, the representation of the internal gas at the same moment.*

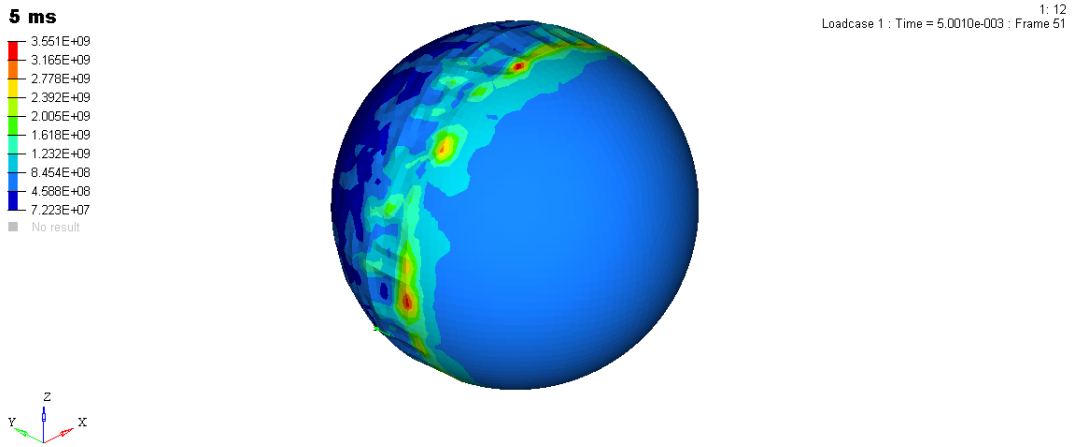

Figure 6.46: RADIOSS Case Study 12-NG. *On the left, contour plot of the sphere at 5 ms. On the right, the representation of the internal gas at the same moment.*

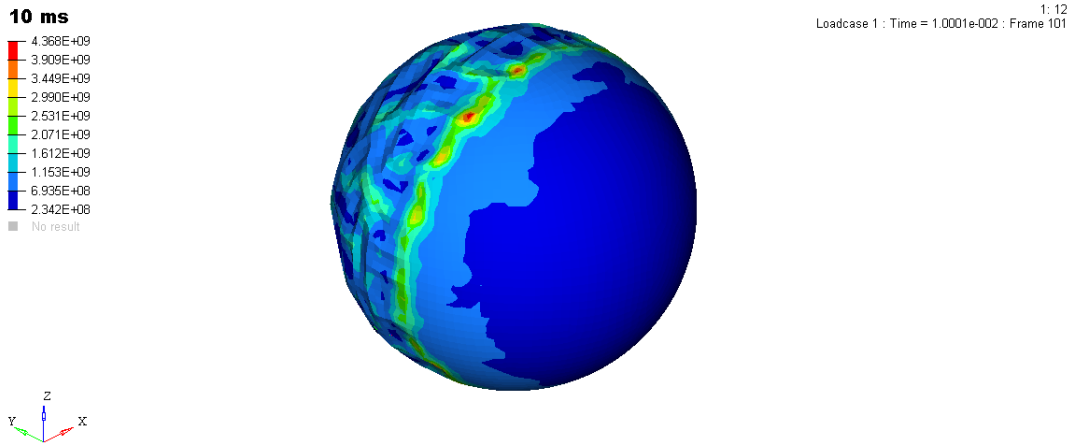

Figure 6.47: RADIOSS Case Study 12-NG. *On the left, contour plot of the sphere at 10 ms. On the right, the representation of the internal gas at the same moment.*

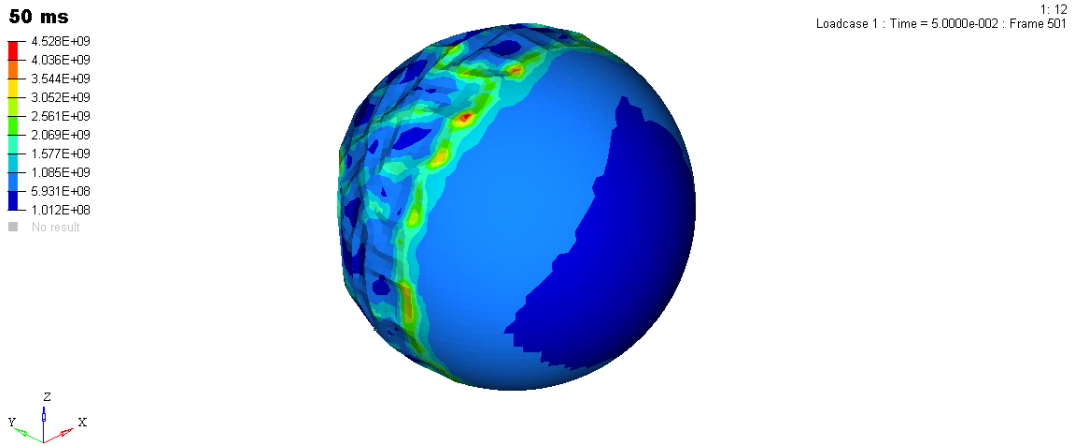

Figure 6.48: RADIOSS Case Study 12-NG. *On the left, contour plot of the sphere at 50 ms. On the right, the representation of the internal gas at the same moment.*

In this case, looking at the figures a very important thing is immediately highlighted: the sail does not undergo any kind of breaking and the simulation runs successfully until the end, for a run time of 50 ms.

A very important information can be extracted from these results: without gas, the transient phase tends to end far earlier than what happened with internal gas. In fact, going ahead with time the maximum stress remains located on the same zone and its value grows of 23% from five to ten milliseconds and only of 3% from ten to fifty milliseconds.

So the stress developed within the sail tends to an asymptote which seems very close to the value shown at 50 ms, but the most important thing is that such stress is below the yield stress of 10 GPa with a safety factor of 2.22 .

6.7.4 RADIOSS Case Study 13-NG

The last case analyzed presents a further increase in thickness, to understand if, at a certain point, the shell inertia does prevail on the resistance due to higher thickness. This Case Study presents the configuration in table 6.9.

	RADIOSS Case Study 13-NG
Young Modulus [GPa]	200
thickness [μm]	0.4
p_{infl} [Pa]	0
m_g [g]	0
tollerance	30%
p_{laser} [Pa]	216
E_f [W/m^2]	2.30e+11
$E_{f_{tot}}$ [W]	2e+11
Total mass [g]	6.8
acceleration	20000g

Table 6.9: Summary of RADIOSS Case Study 13 - NG

In this case the thickness have been doubled with respect to the previous one and so also laser pressure and power have been treated the same way.

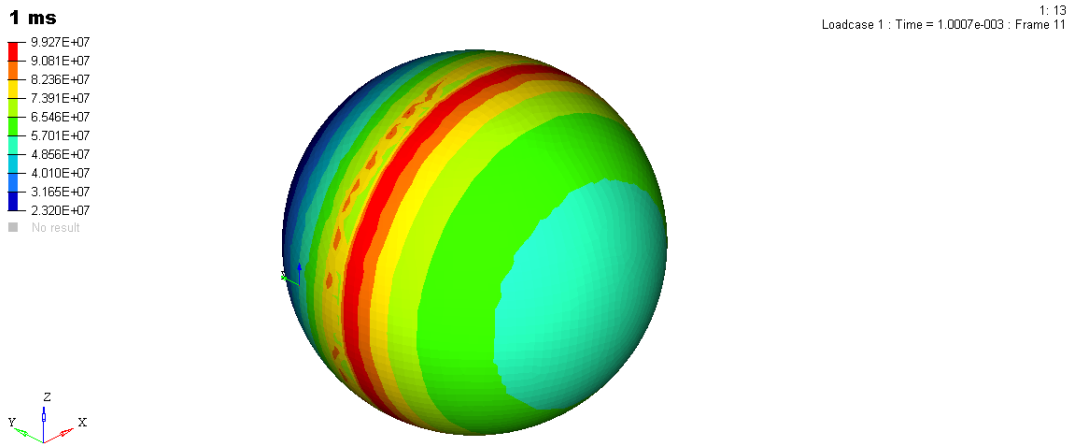

Figure 6.49: RADIOSS Case Study 13-NG. *On the left, contour plot of the sphere at 1 ms. On the right, the representation of the internal gas at the same moment.*

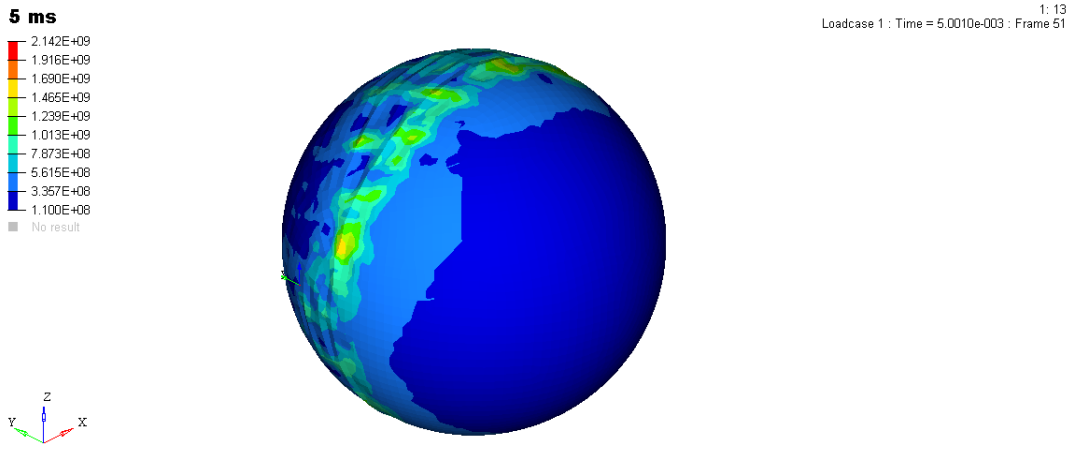

Figure 6.50: RADIOSS Case Study 13-NG. *On the left, contour plot of the sphere at 5 ms. On the right, the representation of the internal gas at the same moment.*

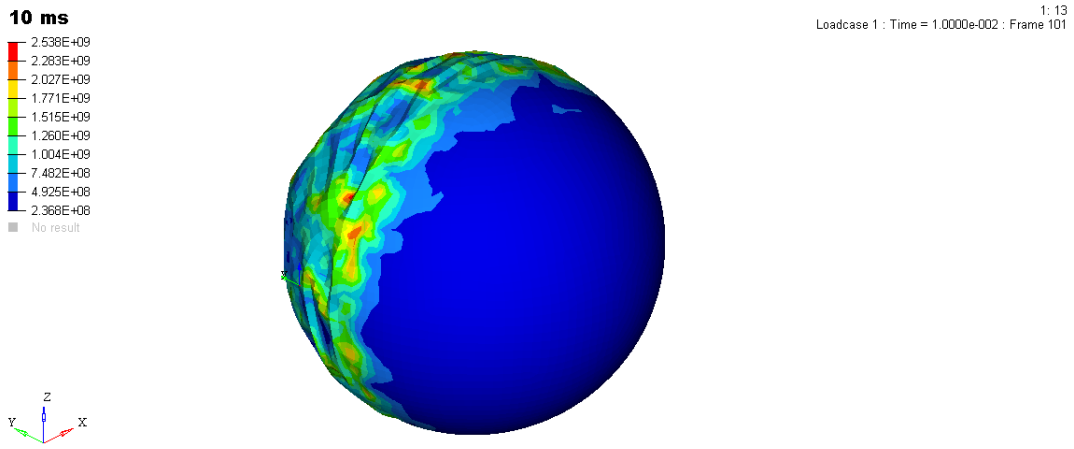

Figure 6.51: RADIOSS Case Study 13-NG. *On the left, contour plot of the sphere at 10 ms. On the right, the representation of the internal gas at the same moment.*

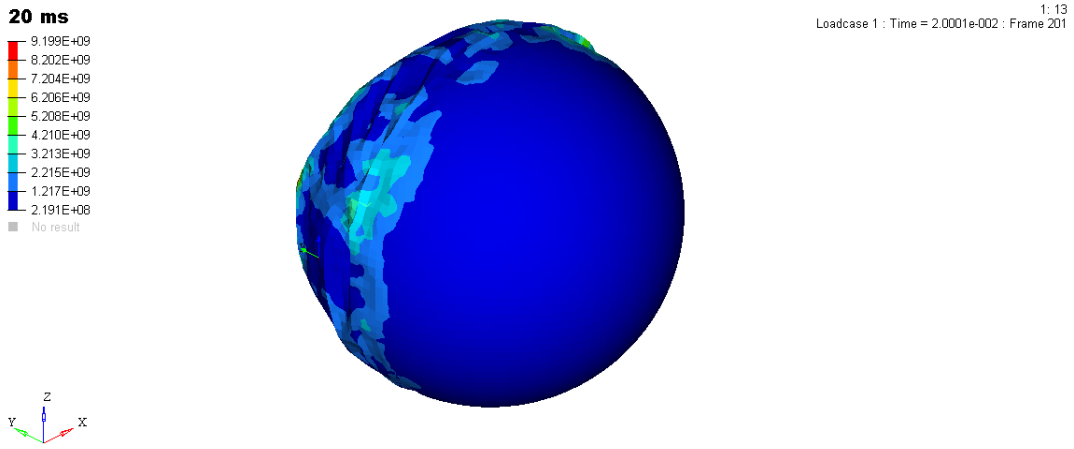

Figure 6.52: RADIOSS Case Study 13-NG. *On the left, contour plot of the sphere at 20 ms. On the right, the representation of the internal gas at the same moment.*

What happens confirms the doubts:

- the stress distribution is quite different, in fact a substantial increment in stress on the non-irradiated face is visible already at 1 ms , and it is clearly caused by the higher inertia of the shell iteself;
- the deformation of the non irradiated face is more important and and the maximum stress reaches almost the yield stress already at 20ms;
- going ahead with time the stress goes over yield stress and so the sail breaks.

Such behavior suggests that there is a delicate equilibrium between all the parameters and a proper trade-off must be found in order to ensure that the configuration works and is stable.

6.8 Design solutions

In this chapter several analyses were first performed and then discussed. Summarizing, it was verified that the mechanical issues experienced by the sail during its motion are mainly due to the presence of gas, which has a destabilizing effect. In fact, a working configuration was found by removing the internal gas, which is evidently not only unnecessary but also damaging after the unfolding phase.

For this reason, some design solutions could be:

- building the sail spherical shell by inserting a restricted zone on the irradiated face made with a different material which is strongly volatile, so that after the unfolding phase such zone evaporates thanks to the heat generated by the laser radiation and the gas is automatically discharged in space;
- the zone made with the volatile material could be also placed onto the non-irradiated surface, so that there is also the advantage of reducing the inertia of the shell which can cause damages. In that case an automated heating system must be provided in order to allow the gas to be discharged in space due to pressure gradient, because such zone does not undergo the heat provided by the laser beam;

- also a system more similar to a pressure valve could be built either on the irradiated surface or on the other one, in order to allow the gas to discharge when reaching a certain pressure; maybe it can be done by using the same valve used to inflate the sail;

- the last idea, which is probably the most elegant, could be that of adopting a pre-loaded folded configuration that does not bring the sail in plasticity and , once the load is removed, allows the sail to assume its natural spherical shape by itself.

Each solution brings also some drawback and issues to solve, both from a manufacturing point of view and from a physical point of view.

For example, some issues would be:

- the volatile zone must evaporate almost immediately after the irradiation, in fact we have seen how in few milliseconds the sail breaks; this can be made for example by adopting an irradiation law with a slow ramp until the part evaporates or maybe it will not be necessary because in the first milliseconds the combination of laser pressure and gas inertia make the evaporation faster;

- once the zone is evaporated a hole in the sail shell would weaken the mechanical structure which could undergo breaking also without the gas.

So, for each idea proposed, a whole new analysis must be performed in order to understand if such idea works or not.

In the end, the ideas proposed are only few ideas which might work, but this topic will not be discussed further and will be object of future studies and developments.

Chapter 7

Conclusions and Future Developments

Throughout the whole master thesis work, several steps of the preliminary phase of Starshot project have been treated.

In Chapter 2 an overview on the sail configuration was presented and a spherical shape for the sail was chosen based on previous studies.

In chapter 3 an overview on a 2D Model was presented as the state of the art of the project, with several approximations with respect to the actual specifications. In fact, a phenomenon with much lower accelerations, smaller diameter and thicker membrane was investigated. In addition, a non-specialized fem code was used because of its capability to make preliminary analyses in short time but with good reliability. Such approximations were necessary because the complete configuration would have requested unreasonable computing power and time, due to the inadequate software.

In chapter 4 a first 3D analysis was made in order to assess the goodness of the model and in order to get rid of some simplifying hypothesis made in chapter 3. The results proved that the new 3D model does not show geometric non-linearities.

For this reason, in chapter 5 the first complete 3D study was made with Optistruct, and in particular through inertia relief method. Although this set-up proved to work, such model does not include the gas inertial contribution but only a constant pressure along the whole inner surface, which is not even similar to the

actual case. For this reason, an analytical model based on a simplified scheme was developed and then applied to the model through an equation in order to simulate the gas presence and its inertial contribution. The complete model showed how the presence of gas causes a rise of the stress level and so its mass must be kept low in order to minimize such effects.

In the end the most accurate model is presented in chapter 6; the internal gas is simulated by SPH in order to capture dynamic effects of the gas and its motion in time during the dynamic simulation. The model in this case is made by a less dense mesh due to its higher complexity which would lead to unreasonable simulation time and cost with a better mesh.

From the last chapter a very important information comes out: the internal gas is necessary for unfolding phase but it is destabilizing in other phases and always causes the sail to break. For this reason, it is necessary to find a new configuration in which the gas is not present or it is expelled before the acceleration phase starts (just after the unfolding phase). Some design solutions are proposed and future work can start from that solutions in order to test them better.

Future developments can include:

- a new simulation based on models of Chapter 6 but with a strongly refined mesh in order to have some numerical results quantitatively reliable;
- perform numerical analyses taking into account the thermal contribution of the laser on the irradiated face;
- develop a better and more accurate material model;
- acquire more informations about the laser plant which will be used to propel the sail;
- develop a physical prototype so that experimental tests can be made and compared to the numerical analyses.

Bibliography

[1] Zachary Manchester - Abraham Loeb (2017), *Stability of a light sail riding on a laser beam*

[2] Giancarlo Genta - Dario Riccobono (2017), *Preliminary Analysis of the deformed shape of an inflated light sail*

[3] GChunyu Li, Tsu-Wei Chou (2003), *Elastic moduli of multi-walled carbon nanotubes and the effect of van der Waals forces*

[4] T. Pozar (2014), *"Oblique reflection of a laser pulse from a perfect elastic mirror"*

[5] F.J. Low et al., *"Infrared cirrus, New components of the extended infrared emission"*, in Astrophysical Journal Letters

[6] Lin Liao, *A study of inertia relief analysis*, Structural Dynamics and Materials Conference

[7] David W. Sleight and Danniella M. Muheim, *"Parametric Studies of Square Solar Sails Using Finite Element Analysis"*, Structural Dynamics and Materials Conference

[8] Altair Engineering, *"Introduction to explicit methods"*

[9] R.A. Gingold and J.J. Monaghan (1977), *"Smoothed particle hydrodynamics: theory and application to non-spherical stars"*

[10] Li, Q. and J.S. Racine (2007), *"Nonparametric Econometrics: Theory and Practice. Princeton University Press"*

[11] Erwin Kreyszig (2005), *"Advanced Engineering Mathematics (9 ed.)"*

[12] Schoenberg, Isaac J. (1946),

[13] Altair Engineering, *Interface (Contact) Modeling*

[14] J.P. Salvetat et al. (1999), *"Mechanical properties of carbon nanotubes"*

[15] Bong Wie (2004), *"Solar Sail attitude Control and Dynamics"*

[16] RenÃÍ Heller and Michael Hippke (2017), *"Deceleration of high-velocity interstellar photon sails into bound orbits at α Centauri"*

[17] G. Genta et al. (2000), *"Gyroscopic Stabilization of Passive Magnetic Levitation".*

[18] G. Genta and E. Brusa (1999), *"The Aurora Project: a New Sail Layout"*, in Acta Astronautica

[19] E. Brusa, C. Delprete, G. Genta, *"FEM Structural Assessment of the Aurora Solar Sail Spacecraft"*

[20] G. Genta (2009), *"Vibration dynamics and control"*, Springer

[21] P. Zhao and G. Shi, *"Study of Poisson's Ratios of Graphene and Single-Walled Carbon Nanotubes Based on an Improved Molecular Structural Mechanics Model"*, in Tech Science Press

[22] G. Vulpetti (2012), *Fast Solar Sailing: Astrodynamics of Special Sailcraft Trajectories*, Space Technology Library Vol. 30, Springer

[23] G. Vulpetti, L.Johnson, G.L. Matloff (2008), *Solar Sails: a novel approach to interplanetary travel*, Copernicus Books